Low speed wind tunnel design, setup, validation and testing of airfoils in turbulent inflow conditions

Iván Torrano Zabalza

Mondragon Goi Eskola Politeknikoa
Mechanical and Industrial Manufacturing Department

July 12, 2016

Low speed wind tunnel design, setup, validation and testing of airfoils in turbulent inflow conditions

Iván Torrano Zabalza

dirigida por:

Dr. Manex Martinez-Agirre
Mechanical and Industrial Manufacturing Department
Mondragon Unibertsitatea

Dr. Mustafa Tutar
Ikerbasque, Basque foundation for science

para la obtención del grado de Doctor
bajo el programa de doctorado de la Universidad de Mondragon:
Programa de Doctorado en Ingeniería.

Tribunal de Tesis:
Presidente: Dr. Mickael Bourgoin (ENS-Lyon)
Vocal: Dr. Xabier Munduate (CENER)
Vocal: Dr. Rajnish Kaur Calay (University of Tromsø)
Vocal: Dr. Martin Obligado (LEGI)
Secretario: Dr. Alain Martin (Mondragon Unibertsitatea)

July 12, 2016

Abstract

The present work aims to design and setup a low speed wind tunnel (LSWT) to be constructed at Mondragon Unibertsitatea for aerodynamic performance analysis of airfoils at low Re number. With this purpose, flow field characteristics through the test section are investigated to ensure that the flow quality requirements are accomplished. Once the LSWT is validated, a passive grid is installed upstream of an airfoil model representative of wind turbine blade sections to analyse the effect of free-stream turbulence conditions on the aerodynamic performance. In the second stage, two modelling approaches are developed in the context of grid-generated turbulence. The ability of simple numerical simulations (Reynolds Averaged Navier-Stokes) to capture the large scale properties of the turbulence downstream a passive grid is tested for design purposes of the grid. The study is completed with the development of a new inflow turbulence generation method to be applied within large eddy simulation (LES) for its use in airfoil simulations at low Re number. Finally, it is proposed that the developed method can be combined with the performed detached eddy simulations (DES) of the flow around an airfoil. These simulations represent a promising approach to numerically study the effect of turbulent inflow conditions on airfoil performance, which is one of the main limitations of numerical methods for modelling turbulence.

List of Figures

List of Tables

Glossary

Symbols

L	Characteristic length of the flow
l	Characteristic length scale of eddies
ρ	Density
u^+	Dimensionless velocity
y	Distance to the wall
C_D	Drag coefficient
q	Dynamic pressure
μ	Dynamic viscosity
f	Friction factor
u_τ	Friction velocity
ν	Kinematic viscosity
η	Kolmogorov lenght scale
Re_η	Kolmogorov Reynolds number
τ_η	Kolmogorov time scale
C	Kolmogorov universal constant
u_η	Kolmogorov velocity scale
M	Mach number
Q	Mass flow rate
U,V and W	Mean velocity components
M	Mesh size
β	Porosity
A	Power-law constant
n	Power-law decay exponent
x_0	Power-law decay virtual origin

Δp_{fan}	Pressure rise in the fan
G_k	Production of turbulence kinetic energy
Re	Reynolds number
σ	Solidity
ω	Specific dissipation rate
λ	Taylor microscale
t	time
ΔH	Total pressure loss
ϵ	Turbulence kinetic energy dissipation rate
$E(\kappa)$	Turbulence kinetic energy spectrum
I	Turbulence intensity
k	Turbulence kinetic energy
τ_w	Wall shear stress
y^+	Wall y plus
κ	Wave number
K	Wind tunnel section loss

Subscripts

$(\bullet)_i$	Referring to the x direction
$(\bullet)_j$	Referring to the y direction
$(\bullet)_l$	Referring to the local loss
$(\bullet)_{lt}$	referring to local loss referred to the test section

Superscripts

$\overline{(\bullet)}$	Time averaged value
$(\bullet)'$	Fluctuating part
$\hat{(\bullet)}$	Spaced filtered value

Operators

$\Delta(\bullet)$	Variation
$\frac{\partial(\bullet)}{\partial(\bullet)}$	Partial derivative

$\frac{d(\bullet)}{d(\bullet)}$	Total derivative
$\int(\bullet)$	Definite integral

Acronyms

ABL	Atmospheric Boundary Layer
BR	Blockage Ratio
CFD	Computational Fluid Dynamics
DES	Detached Eddy Simulation
DSGS	Dynamic Sub-Grid Scale
EVM	Eddy Viscosity Models
FST	Free-stream Turbulence
HIT	Homogeneous and Isotropic Turbulence
LES	Large Eddy Simulation
LSB	Laminar separation bubble
LSWT	Low-Speed Wind Tunnel
MU	Mondragon Unibertsitatea
RFG	Random Flow Generation
RANS	Reynolds Averaged Navier-Stokes
rms	root-mean squared.
SGS	Sub-Grid Scale
VAWT	Vertical Axis Wind Turbine
WALE	Wall-Adapting Local Eddy Viscosity
WMLES	Wall-modeled Large Eddy Simulation
WTT	Wind Tunnel Test

Contents

Chapter 1

Introduction

Man has evolved within a world where air and water are, by far, the most common fluids encountered. The nations and industries worldwide support research and development of aerodynamics, which is the branch of fluid mechanics concerned with the study of the movement of air and its interaction with objects. Understanding the motion of air around an object (often called a flow field) enables the calculation of forces and moments acting on the object. The flow field is characterized by the dimensionless Reynolds number Re, defined as the ratio of inertial forces to viscous forces and consequently quantifies the relative importance of these two types of forces for given flow conditions:

$$\mathrm{Re} = \frac{\rho V L}{\mu} \tag{1.1}$$

where ρ is the fluid density, μ is the dynamic viscosity, V is the flow velocity and L is the characteristic length of the flow. Depending on the order of magnitude of the Reynolds number Re, the flow is determined in laminar or turbulent conditions, and the way to address the problems of aerodynamics is different. Although the theory of laminar flows satisfactorily predicts behavior in laminar flow regime, the study of turbulent flows currently still poses many challenges that continue to fuel the interest of physicists, mathematicians and engineers.

Almost all fluid flow which we encounter in daily life is turbulent. The boundary layers and the wakes around and after bluff bodies such as cars, airplanes and buildings are turbulent. In order to characterize turbulent flows, do experiments in a wind tunnel is a matter of prime importance. There is growing interest in the study of aerodynamics, mainly promoted by civil companies for development of aircraft, automobiles, marine and architectural structures. Most of the wind tunnels were built for the aviation industry. However, there are a large number of existing tunnels for all types of applications, such as smoke tunnels, aeroacoustic tunnels, racing tunnels and environmental tunnels. These

facilities usually respond to large companies given the size and its high cost and they are beyond the reach of small companies. However, low speed wind tunnels (LSWT) are more suitable for companies and universities where a tunnel is used for basic investigations.

1.1 Motivation

This research work is motivated by the need to design an open-circuit LSWT which is to be constructed at Mondragon Unibertsitatea (MU). LSWTs are commonly designed and constructed to study aerodynamic devices operating at low Reynolds numbers, since higher regimes can only be obtained in relatively large and fast wind tunnels.

In the last decade, due to the development of vertical axis wind turbines (VAWT) and small horizontal axis wind turbines (HAWT), there is a growing interest in the study of airfoils operating at low Reynolds regime. The experimental data obtained in wind tunnel tests at this regime is necessary to produce design data for the blade profiles of wind turbines and to overcome the limitations of Computational Fluid Dynamics (CFD).

VAWTs and HAWTs operate inside the atmospheric boundary layer (ABL) and are subjected to high free-stream turbulence (FST) levels. These high turbulence levels can be originated from the shear in the ABL or from the wake of other wind turbines if they are placed in a wind farm, as shown in Figure 1.1.

Figure 1.1: Wind farm property of Vattenfall, photografied by: Christian Steiness

The turbulence characteristics of the incoming flow are important parameters that need to be addressed. The aerodynamic behavior of an airfoil can be strongly affected by free-stream turbulence, specially in the angle range near the stall. To analyze the effect of inflow turbulent conditions on the performance of an airfoil, a common technique is to generate prescribed turbulent flow conditions by the use of grids at the entrance of the test section. Since the design of these grids relies on empirical relations, in this work the ability of simple steady Reynolds averaged Navier-Stokes (RANS) solutions to capture

the large scale properties of the decaying grid-generated turbulence is tested for design purposes of the grid.

Nowadays, the treatment of inlet conditions is one of the main limitations of the numerical methods for modelling turbulence. If the turbulence quantities are specified at the inlet without relation to the structure and shape of the turbulent eddies, the flow lacks realistic turbulent structure and the turbulence level in the separated shear layer decays rapidly. This causes the local turbulence intensity downstream the inlet to be much smaller than the inlet value, hindering the imposition of high turbulence levels. The inflow conditions should ideally possess correlated temporal and spatial fluctuations and a proper energy spectrum. In this context, the need of an inflow turbulence generation method that produces high turbulence intensity levels characteristic of the atmospheric boundary layer for its application in large eddy simulation (LES) is detected.

When performing simulations of airfoils at low Re number, the exact location of the laminar transition point is essential to obtain accurate predictions. In the last decade, detached eddy simulations (DES) have been successfully applied together with transition models (γ model) inside the boundary layer for simulating airfoils under smooth inflows and medium inflow turbulence intensity levels. If these simulations are combined with a proper inflow generation method that enables the imposition of higher turbulence intensity levels, they would represent a promising approach to numerically study the effect of free-stream turbulence on airfoil performance.

1.2 Objectives

Based on the identified limitations, the following main objectives are defined:

1. To design and setup a low speed wind tunnel for aerodynamic performance analysis of airfoils at low Re numbers under different turbulence inflow conditions. To meet this main objective, the following partial objectives are defined:

   (a) To design and setup a low speed wind tunnel for aerodynamic performance analysis of airfoils at low Re numbers.

   (b) To setup a experimental methodology to test airfoils at low Re numbers.

   (c) To analyse the effect of free-stream turbulence on the aerodynamic performance of a thick airfoil representative of wind turbine blade sections.

2. To numerically investigate the turbulent inflow conditions generated by a passive grid. To this end, the following secondary objectives are determined:

(a) To propose a RANS-based simulation tool for design purposes of passive grids in order to produce prescribed turbulent inflow conditions.

(b) To develop a passive grid-generated turbulence technique within LES to numerically investigate the effect of turbulent inflow conditions on airfoil performance.

1.3 Overview of the dissertation

The work carried out is divided into five different chapters corresponding to the defined partial objectives. Each chapter opens with an introduction containing the motivation and the relevant state of art related to the topics to be discussed during the chapter. After the introduction, the dissemination of the results is presented splitted in different sections. At the end of each chapter, the conclusion section summarizes the findings achieved.

Chapter 2 contains all the relevant issues concerning the design, setup and validation of the LSWT. The state of art condenses the design criteria established in bibliography to meet the flow quality requirements for the investigation of airfoils at low Re numbers. The discussion of the results is comprised of three sections. First, the design of the wind tunnel is presented together with the pressure drop calculation through the different LSWT sections. Then, the experimental setup is described including the instrumentation employed and the data acquisition system. Finally, the validation of the flow quality in the test section is discussed.

Chapter 3 is focused on setting up a experimental methodology to study airfoils at low Re numbers. The introduction points out the difficulties encountered when dealing with airfoils in the low Re regime, which are mainly caused by the sensitivity of laminar boundary layer to external disturbances. Next, a review of the different experimental methodologies to measure the aerodynamic coefficients is provided, accounting for the different source of errors that may arise. In the next section the current experimental arrangement installed at the LSWT is presented and some preliminary tests to verify the accuracy of the airfoil model and the balance alignment procedure are performed. In order to validate the implemented experimental methodology, airfoil performance data measurements are discussed in comparison with well recognized wind tunnel tests found in literature under similar flow conditions.

In Chapter 4 the basic theory behind the turbulent flow motions is provided, and the most relevant techniques for studying the behavior of turbulent flows are collected from the experimental point of view. Among all the turbulent flow cases that are studied in literature, the canonical case of grid-generated turbulence is emphasized as it is

the most documented configuration to characterize the fundamental properties of turbulence. Moreover, the use of grids at the entrance of the LSWT test section is a common technique to generate prescribed turbulent inflow conditions. This technique permits to experimentally reproduce the high intensity turbulence levels that exist in the atmospheric boundary layer (ABL). This way, it is possible to study the effect of free-stream turbulence on airfoils representative of wind turbine blade sections. Regarding the discussion of the results, a preliminary study is done to characterize the decay of grid-generated turbulence and define the different turbulence levels to be tested. Subsequently, airfoil performance data measurements under these conditions are conducted.

The design criteria for the grids used in grid-generated turbulence studies relies on a few empirical rules. Chapter 5 aims to use simple simulations as a tool to design grids with prescribed turbulent characteristics. First, a summary of the most common turbulence modelling strategies is presented. Due to its lower computational cost compared to direct numerical simulation (DNS) or large eddy simulation (LES), steady Reynolds averaged Navier-Stoke (RANS) solutions are chosen as parametric studies are easier to achieve. Then, the ability of different turbulence models to capture the large scale properties of the decaying grid-generated turbulence is tested for design purposes of the grid. The numerical simulations are validated with the experiments performed at $\mathrm{Re}_\lambda = 100$ based on the Taylor microscale downstream a passive grid.

In Chapter 6, LES simulations of grid-generated turbulence are proposed as a cost effective inflow turbulence generation method. The final aim is to use the proposed technique in an airfoil simulation to numerically investigate the effect of turbulent inflow conditions. The chapter starts pointing out the difficulties of modelling airfoils at low Re numbers, which is nowadays one of the most challenging tasks in CFD. Next, a description of the most common methods to generate turbulent inflow conditions within LES are revised. The discussion of the results is divided in two sections. First, several airfoil simulations at low Re numbers under smooth inflow conditions are computed in comparison with the experimental data presented in Chapter 4. Secondly, the results of the proposed passive grid-generated turbulence technique to produce turbulent inflow conditions in LES are presented and compared with other methods.

Chapter 2

Low-speed wind tunnel (LSWT) design, setup and validation

Wind tunnels are facilities that enable researchers to study the flow over objects of interest, the forces acting on them and their interaction with the flow. Since the very first day, wind tunnels have been used to verify aerodynamic theories and facilitate the design of aircrafts and, for a very long time, this has remained their main application. Nowadays, the aerodynamic research has expanded into other fields such as automotive industry, architecture, environment and education, making low speed wind tunnel tests more important. Although the usefulness of CFD methods has improved over time, thousands of hours of wind tunnel tests (WTT) are still essential for the development of new aircrafts, wind turbine or any other design that involves complex interactions with the flow.

The chapter is motivated by the need to design a LSWT to study aerodynamic devices operating at low Reynolds numbers, containing all the relevant issues concerning the design, setup and validation of the LSWT to be constructed at Mondragon Unibertsitatea (MU).

2.1 Introduction

It is very common to express the velocity of the planes V based on the Mach number M, which relates the inertia and elasticity forces as:

$$\mathrm{M} = \frac{V}{V_s}, \tag{2.1}$$

where V_s is the velocity of sound in the medium.

Depending on the value acquired by the Mach Number, wind tunnels are classified as:

- Subsonic ($M < 0.7$)
- Transonic ($0.7 < M < 1.2$)
- Supersonic ($1.2 < M < 5$)
- Hypersonic ($M > 5$)

Figure 2.1 shows the subsonic-transonic S1MA wind tunnel of ONERA in Modane, France, which is the largest facility of its kind in the world reaching Mach numbers from 0.05 to 1.

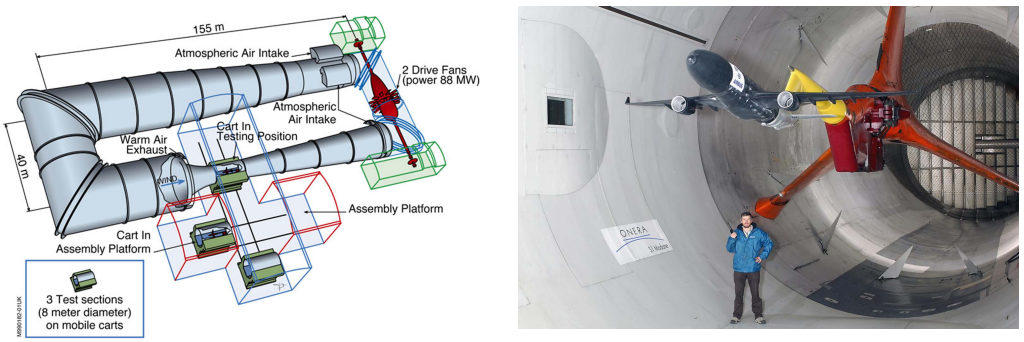

Figure 2.1: S1MA - Continuous-flow wind tunnel, Mach 0.05 to 1 (Images taken from ONERA website [1]).

There are two basic types of wind tunnels: open circuit and closed circuit. The air flowing through an open circuit follows an essentially straight path along the different sections that comprised the tunnel. The air flowing through a closed circuit recirculates continuously with little or no exchange of air with the exterior. Figure 2.2 shows a plan view of both open and closed circuit wind tunnels.

There are some advantages and disadvantages when employing open or closed wind tunnels. For example, construction cost for an open wind tunnel is typically much less compared to a closed one. The main disadvantages are that for a given size and speed the tunnel will require more energy to run than a closed tunnel and, in general, open tunnels tend to be noisy. On the other hand, in closed circuit tunnels the quality of the flow can be well controlled and most important will be independent of weather conditions. However, they usually require cooling systems as the air recirculates increasing its temperature due to viscous dissipation into heat. Because of low initial cost, an open circuit tunnel is often ideal for schools and universities where a tunnel is required for classroom work and high utilization for research is not required.

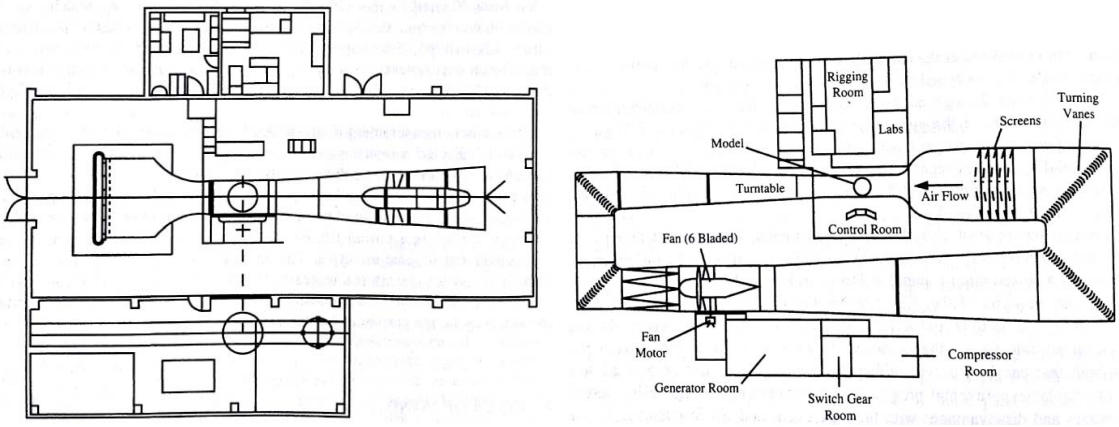

(a) (b)

Figure 2.2: Comparison between open and closed circuit wind tunnels (a) Plan of view of an open circuit wind tunnel, Diamler-Benz Aerospace Airbus, Bremen, Germany. (b) A closed circuit wind tunnel, Defense Establishment Research Agency (DERA), Bedford, England. (Images taken from Barlow *et al.* [2])

Depending on the position of the power section open wind tunnels are classified as blower tunnels or suction tunnels (also known as Eiffel type). In blower tunnels the air is generated by centrifugal blower at the entry of the wind tunnel. A characteristic design problem for these facilities is choice of details of the wide-angle diffuser between the blower and the settling area prior to the contraction. In Eiffel type wind tunnel this problem is avoided as typically axial fans located at the exit suck out the air and there is no need to reduce the turbulence generated by the blades.

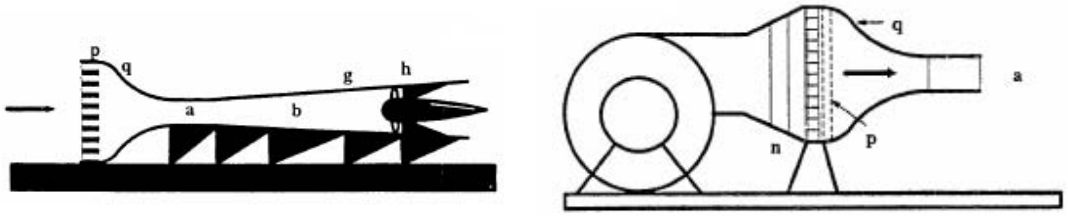

(a) (b)

Figure 2.3: Types of open circuit wind tunnels; (a) Eiffel type wind tunnel ; (b) Centrifugal blower (images taken from Barlow *et al.* [2])

2.1.1 Open LSWT sections and energy losses

LSWT can be designed for operations at very low Mach number M with speeds in the test section up to ≈ 100 m/s (M = 0.3) on the assumption of incompressible (ρ =constant) and inviscid air flow. LSWT are comprised of different sections as shown in Figure 2.4.

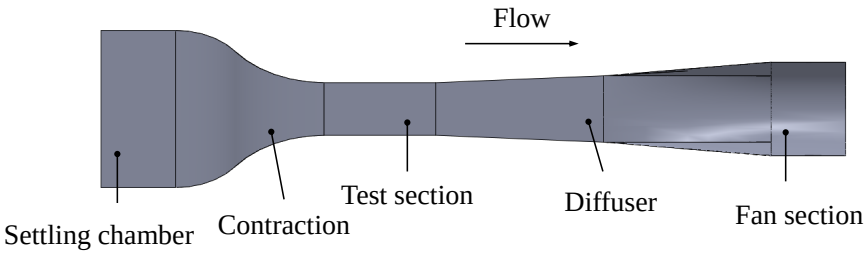

Figure 2.4: Sections of an open Eiffel type wind tunnel.

Wattenford [24] considers that the losses through the wind tunnel can be obtained by splitting the tunnel into different sections and analyzing the losses of each component in succession. According to its instructions, the section loss parameter K_l in a section can be represented or identified by the dimensionless ratio of the pressure loss in the section ΔH_l to the dynamic pressure q_l at the entrance.

$$K_l = \frac{\Delta H_l}{q_l} = \frac{\Delta H_l}{1/2\rho V_l^2} \tag{2.2}$$

This concept is then extended and applied to constant-area sections, where primary losses have the major influence in the pressure drop. Concerning geometry changes in closed conduits and/or LSWT sections, the secondary also take relevance. These and other guidelines are also suggested by NASA, Eckert [25].

In the following paragraphs the design of each part will be thoroughly discussed and analyzed in detail to get the best design addressing the general and particular requirements.

Settling chamber

The air sucked into the LSWT by the fan needs to be uniform and controlled. Thus, the non-uniformities and boundary layer separations must be corrected. For example, a typical problem is the formation of the *vena contracta* phenomena at the inlet of the settling chamber. The reason for this phenomenon is that fluid streamlines cannot abruptly change direction. In the case of sudden pipe diameter change, the streamlines are unable to closely follow the sharp angle in the LSWT wall. The converging streamlines follow a smooth path, which results in the narrowing flow and the consequent boundary layer separation (Figure 2.5). To avoid this problem typically an inlet radius is employed.

(a) (b)

Figure 2.5: (a) Illustration of the *vena contracta* phenomena (image taken from Falkovich [3]) (b) Inlet radius at the open wind tunnel facility in Green Building Research laboratory at Portland State university (image taken from GBRL website [4]).

Another problem present in the incoming flow is its non-uniformity. When a high quality flow is required, some devices can be installed to increase the flow uniformity and to reduce the turbulence level at the entrance of the contraction. The most commonly used devices are screens and honeycombs.

According to Prandtl [26], a honeycomb is a guiding device through which the individual air filaments are rendered parallel. Thus, honeycomb is very efficient at reducing the lateral turbulence, as the flow pass through long and narrow pipes. Nevertheless, it introduces axial turbulence of the size equal to its diameter. This means that honeycombs, while effective as flow straighteners, are not so effective as typical screens in smoothing non-uniformities in flow speed. Figure 2.6 shows some views of typical implementations of honeycomb types in use today.

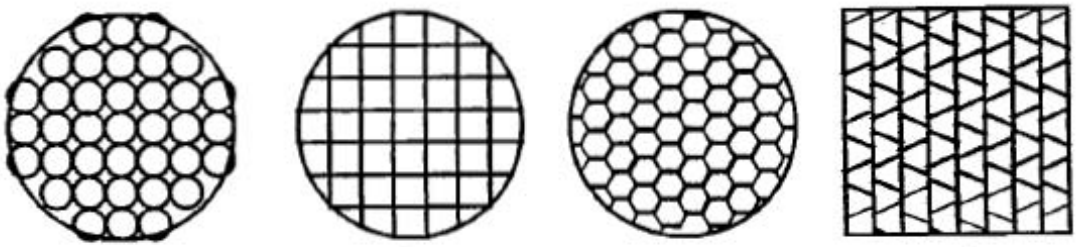

(a) (b) (c) (d)

Figure 2.6: Four types of honeycomb

The design parameters for honeycombs are the length to cell hydraulic diameter ratio L_h/D_h and the porosity β_h defined as:

$$\beta_h = (1 - \Delta/M_h)^2 \tag{2.3}$$

Porosity or open-area ratio β_h is a function of the honeycomb thickness Δ and mesh width M_h. Porosity would be zero for a solid packed honeycomb, and one in the limit of vanishing honeycomb. The complement of porosity, solidity $\sigma_h = 1 - \beta_h$, is sometimes used in literature. Figure 2.7 shows a sketch of the design parameters.

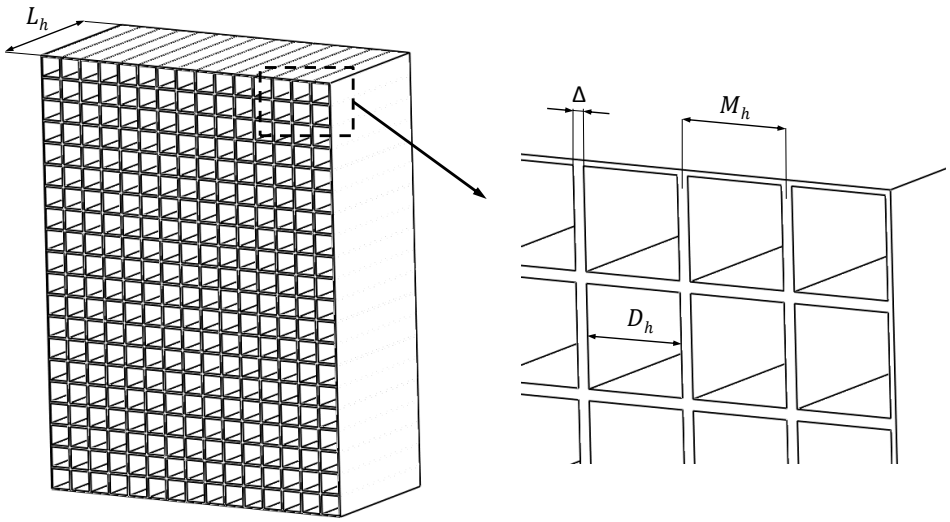

Figure 2.7: Design parameters for the honeycomb.

According to Barlow *et al.* [2] the length L_h must be at least 6-8 times bigger than the hydraulic cell diameter D_h and porosity β_h is typically in the vicinity of 0.8. An expression for losses through honeycomb K_h is given by Eckert *et al.* [25]:

$$K_h = \lambda_h \left(\frac{L_h}{D_h} + 3\right)\left(\frac{1}{\beta_h}\right)^2 + \left(\frac{1}{\beta_h} - 1\right)^2, \tag{2.4}$$

where

$$\lambda_h = \begin{cases} 0.375\left(\frac{\Delta}{D_h}\right)^{0.4} Re_\Delta^{-0.1} & \text{for } Re_\Delta \leq 275. \\ 0.214\left(\frac{\Delta}{D_h}\right)^{0.4} & \text{for } Re_\Delta > 275. \end{cases} \tag{2.5}$$

These expressions depend on Re_Δ, the Reynolds number based on the honeycomb thickness Δ and incoming flow speed.

Some specific data for losses in honeycombs are given by Scheiman and Brooks [27]. For honeycombs of the types shown in Figure 2.6 the values of K_h are found to be 0.30, 0.22, and 0.2 for a, b, and c respectively. Roughly speaking, the loss in the honeycomb in a wind tunnel is usually less than 5 % of the total tunnel loss. Mehta and Bradshaw

[28] indicate that about 150 honeycomb cells per settling chamber diameter, or about 25000 total cells, are adequate.

Another device for turbulence control is the flow conditioning screen. Although screens do not significantly influence the lateral turbulence, they are very efficient at reducing the longitudinal turbulence. Two basic parameters are used to characterize a screen: The porosity β_s and the wire Reynolds number $\mathrm{Re}_w = \rho V d_w/\mu$. Porosity, similarly to the case of honeycombs, is function of the wire diameter d_w and the mesh width M_s (Figure 2.8).

$$\beta_s = (1 - d_w/M_s)^2\,, \tag{2.6}$$

According to Bradshaw [29], the non-uniformities generated by a screen are more prominent for screens β_s <0.57. Also solidity $\sigma_s = 1 - \beta_s$ may be defined as projected solid area per unit total area. Several researchers [29, 30] have found that values of solidity between 0.3-0.4 produce a flow that is stable with both spatial and temporal variation.

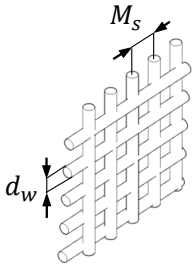

Figure 2.8: Design parameters for the turbulence reduction screens.

A third parameter, the mesh factor K_{mesh} is used to differentiate among smooth and rough wire (or whatever the screen material may be). Mesh factors are given by Idel'Chik [31] as 1.0 for new metal wire, 1.3 for average circular metal wire, and 2.1 for silk thread. Based on this data, Eckert *et al.* [25] give a relation for screen loss coefficient K_m:

$$K_m = K_{mesh} K_{Rn} \sigma + \frac{\sigma_s^2}{\beta_s^2}, \tag{2.7}$$

where

$$K_{Rn} = \begin{cases} 0.785\left(\frac{Re_w}{241} + 1.0\right)^4 & \text{for } Re_w \leq 400. \\ 1 & \text{for } Re_w > 400. \end{cases} \tag{2.8}$$

The Equation (2.8) has a strong Reynolds number dependence for low Reynolds

numbers, but it is almost constant, with a value of about 1, for high Reynolds numbers. At high Reynolds numbers, the flow over the screen wires is supercritical. This means that small scale turbulence is generated by the wires in the screen. Although the reduction in flow fluctuations is less for supercritical than sub-critical screens, it is preferable not to use sub-critical screens because of their very large pressure drop. A series of supercritical screens with consecutively smaller mesh is more effective in reducing flow variations and turbulence than a single sub-critical screen, and with a smaller pressure drop, see Groth [32].

If a better flow quality is desired, a combination of honeycomb and screens is the most recommended solution. This configuration requires the honeycomb to be located upstream of 1 or 2 screens. The mesh width of the screens M_s should be significantly smaller than the integral scale of the incoming turbulence, which is more or less equal to the cell hydraulic diameter of the honeycomb D_h. Reshotko *et al.* [33] defines the sizes of mesh width M_s to be about 5-15 times smaller than the honeycomb cell diameter D_h, being 15 the mesh width of the smallest screen. The distance between the screens needs to be larger than about 30 mesh sizes, for the wire generated turbulence to decay sufficiently, see Groth & Johansson [34].

When the flow has passed through the last screen it has been exposed to a substantial strain, which gives an anisotropic state with most of the turbulence energy in the cross-stream components. It is therefore important to allow it to relax towards an isotropic state before entering the contraction part. The relaxation takes place in settling chamber with constant cross section area. A settling chamber length of 0.5 times the inlet diameter is often used [2]. Just as the screens, the contraction is most effective in reducing streamwise fluctuations and in particular mean velocity variations.

Contraction cone

In the case of the contraction zone, its design is crucial for achieving the required flow quality in the test section. In this sense, its contraction ratio, length and contour definition determine the level of uniformity in the velocity profile, as well as the necessary turbulence attenuation. It is crucial to avoid flow separation close to the walls of the contraction zone. Its aim is to accelerate the flow from the settling chamber to the test chamber, further reducing flow turbulence and non-uniformities in the test chamber. The flow acceleration and non-uniformity attenuations mainly depend on the so-called contraction ratio between the entrance and exit section areas. Typical values are in the range of 6-10 [2]. It is desirable to keep the length of the nozzle as short as possible. The contraction length should be minimized in order to minimize the boundary layer growth. Shorter contractions are also, of course, desirable for saving in space and cost. However, the risk of boundary layer separation increases as the contraction length is

reduced. Boundary layer separation in the contraction leads to undesirable contributions to the non-uniformity and unsteadiness in the exit flow, in addition to a reduction of the effective contraction ratio.

One of the first investigations where the behavior of the boundary layer in the contraction was considered quantitatively was that due to Chmielewski [35]. Since then, most of the studies have involved the calculation of the pressure distributions using various numerical methods and then the application of a boundary layer separation criterion [36]. The most popular separation criterion used has been that due to Stratford [37] for turbulent boundary layer separation. Bell and Mehta also discuss boundary-layer predictions for contractions in their work [38].

The old-style contraction shape with a small radius of curvature at the wide end and a large radius at the narrow end to provide a gentle entry to the test section is not the optimum. There is a danger of boundary-layer separation at the wide end, or perturbation of the flow through the last screen. Good practice is to make the ratio of the radius of curvature to the flow width about the same at each end. Morel gives rules for design of contractions for wall shapes with polynomial curves for axisymmetric contractions [5] and for two-dimensional shapes [39]. He proposed two matched cubic arcs for construction of contraction wall contour, as shown in Figure 2.9.

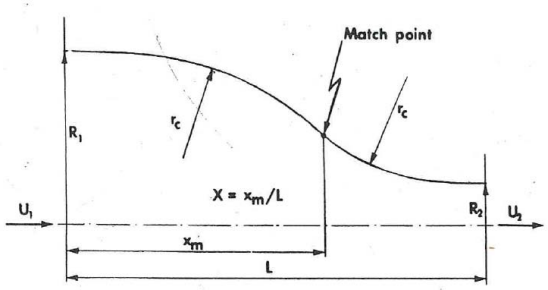

Figure 2.9: Wall contour constructed of two matched cubic arcs (image taken from Morel [5]

Brassard [40] in an unpublished project report *Transformation of a Polynomial for a Contraction Wall Profile* describes a generalization of the fifth-order polynomial proposed by Bell and Mehta [41], to extend the range of shapes and provide different radius of curvature at the two ends. In this report, several desirable characteristics of the wall profile are identified, including; A wall profile having zero first and second derivatives, and inlet and outlet profile radius roughly proportional to the area, that is, the inlet radius is greater than the outlet radius.

To sum up, a design satisfying all criteria will be such that separation is just avoided (implying a minimum acceptable length) and the exit non-uniformity is equal to the maximum tolerable level for a given application (typically less than 1 % variation outside

the boundary layers).

At the stage of design, the most adequate method to verify that the design meets those criteria is computational fluid dynamics (CFD). Sargison [42] makes a calibration of the wind tunnel after construction and validate the design through CFD predictions. Also comparative analysis between theoretical and CFD results of a LSWT designed for Renewable Energy applications are developed. Zehrung [43] provides in his study a feasible design for a cost effective mid-sized wind tunnel used for the purpose of teaching undergraduate students and the testing of green energy wind turbines. In the work done by the present author [44], the design of the contraction zone is performed from both theoretical and numerical methods. First, the pressure drop computations through the wind tunnel are computed from both theoretical and numerical methods. After this, a design modification concerning the curvature wall radius of the contraction section is computed by CFD.

Nowadays, CFD has become a useful tool in wind tunnel contraction design. RodrÃ-guez *et al.* [45] used CFD to propose a novel design for a contraction nozzle based on a logarithmic profile. The improvements obtained with this new proposal were validated, both, numerically and experimentally. Other authors [46] implement optimization techniques in their simulation-driven design of the low-speed wind tunnel contraction. By the use of CFD simulations, as well as a simple multiplicative response correction technique, they achieve to optimize the shape of the contraction.

Barlow *et al.* [2] considers that the losses in the contraction section are from friction only so the pressure drop is obtained by integrating the standard pipe friction law:

$$\Delta p_f = \int_0^{L_c} f \frac{\rho}{2} \frac{V_c^2}{D_c} dx, \tag{2.9}$$

where L_c is the length of the contraction section, $D_c = D_c(x)$ the local hydraulic diameter, and V_c is the local section mean speed.

Continuity equation gives $V_c^2 = V_{sc}^2 \left(\frac{D_{sc}}{D_c}\right)^4$ where V_{sc} is the speed in the settling chamber. The section loss parameter according to Equation (2.2), and using the Equation (2.9) can be written as:

$$K_{cs} = f\left(\frac{L_c}{D_{sc}}\right) \int_0^1 \left(\frac{D_{sc}}{D_c}\right)^5 d\left(\frac{x}{L_c}\right). \tag{2.10}$$

For a typical nozzle shape, the integral of Equation (2.10) has been found to be approximately 0.32. A reasonable approximation for contraction loss that was originally given by Wattenford [24]:

$$K_{cs} = 0.32 f \frac{L_c}{D_{sc}}. \tag{2.11}$$

The above expression seem to be a rudimentary method to estimate the contraction section loss coefficient, as secondary losses due to geometric change are not taken into account. Numerous tables or charts are available in literature where the section loss parameter for a contraction can be known based on its design geometric parameters, the contraction ratio and the cone angle. An example of these charts can be observed in [47].

As the effects of the size and shape of the contraction on the flow are highly nonlinear, it is often necessary to use CFD to make design decisions about key features of the contraction, such as the length, contraction ratio, and, in particular, the wall shape. The design of the contraction zone, together with the honeycomb and turbulence reduction screens placed upstream in the settling chamber, is crucial to reach the desired flow quality in the test section.

Test section

It is the zone of interest, where the drag item is situated and experimental measurements usually take place. Moreover, the prior sections of settling chamber and contraction focuses on reaching a good quality flow in the test section for enable aerodynamic research. The test section is commonly the starting point in the design of a wind tunnel. The rest of sections in a wind tunnel are dimensioned based on test section size, which is defined by the Blockage ratio BR (ratio between the drag item frontal area and the test section cross-sectional area). Depending on the application different values of BR can be found. For example for automobiles a BR$<$5 % is used [2]. For higher BR values wall corrections should be employed. Its length L_{ts} must be sufficient to let the flow be fully developed after the drag item. In aeronautical field it is common to employ a Length-to-hydraulic-diameter ratio greater than 2.

Many shapes have been used for test sections, including round, elliptical, square, rectangular and hexagonal. As the air proceeds along the test section, the boundary layer thickens. In order to minimize secondary flow problems in rectangular test section corners, a 45° fillet is often installed at the start of the contraction and through the test section.

The cost and power are directly determined by the cross-sectional area (the hydraulic diameter D_h) and the length L_{ts}. The section loss parameter is assumed as a constant-area section loss, that can be integrated from the pipe friction law (Equation (2.9)) as:

$$K_{ts} = f \frac{L_{ts}}{D_h}. \tag{2.12}$$

In this equation the friction factor f is based on the *Prandtl universal law of friction*. For smooth pipes at high Reynolds number Shames [48] gives the following relation:

$$\frac{1}{\sqrt{f}} = 2\log_{10}\left(Re\sqrt{f}\right) - 0.8. \tag{2.13}$$

Diffuser

The diffuser of an open wind tunnel typically extends from the downstream end of the test section to the fan section. Since the power losses at any point in the tunnel are expected to vary as the speed cubed, the purpose of the diffuser is to reduce the speed with as little loss energy as possible. Minimum energy loss corresponds to maximum pressure recovery. It is generally desirable to reduce the speed in the shortest possible distance without incurring flow separation. The pressure recovery and pressure gradients and therefore the risk of separation are dependent both the cone angle θ and Area ratio A_R. According to Barlow *et al.* [2], typical values for A_R are in the range of 2-3, with cone angles θ between $2 - 3.5°$. This leads to a diffuser length L_d of about 3-4 times greater than the test section length L_{ts}.

In the diffuser section, both wall friction and expansion losses occur. The diffuser loss coefficient K_d can be decomposed then as a sum of friction loss coefficient and expansion loss coefficient:

$$K_d = K_f + K_{ex}, \tag{2.14}$$

where

$$K_f = \left(1 - \frac{1}{A_R^2}\right)\frac{f}{8\sin\theta}, \tag{2.15}$$

and

$$K_{ex} = K_e(\theta)\left(\frac{A_R - 1}{A_R}\right)^2. \tag{2.16}$$

The factor $K_e(\theta)$ depends significantly on the diffuser cross-sectional shape. Different equations are available for circle and square cross sections in Barlow *et al.* [2], which are based on the experimental data given by Eckert *et al.* [25].

Fan power requirements

Generally two types of fans are used in wind tunnel applications; centrifugal and axial fans. Figure 2.10 shows the operating curves for different fan types, which relates the pressure rise through the fan with the mass flow. It can be observed that centrifugal fans are suitable in applications where a high pressure drops needs to be gained and low mass flow is required. In contrast, axial fans are better for generating higher mass flow and lower pressure rise. In general, this is the case of wind tunnel, so it is very common to use this type of fan as the power input section.

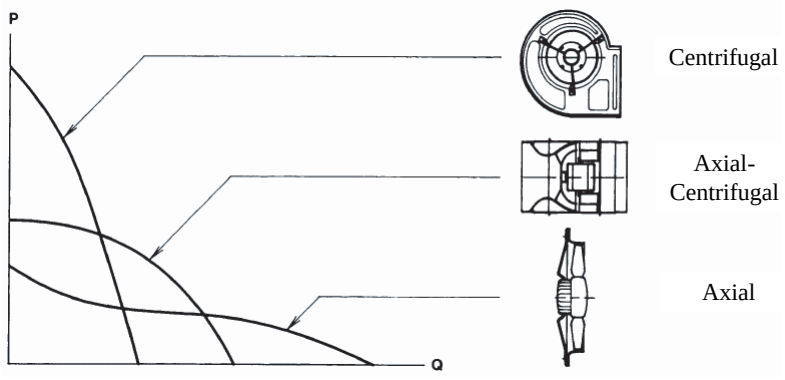

Figure 2.10: Operating curves of different types of fans

The pressure drop through the wind tunnel evolves as a function of velocity squared. This function is recognized as the system characteristic curve. The successive pressure drops in the LSWT sections need to be balanced by the pressure rise through the fan which is given by the operating curve (Figure 2.10). The intersection point between two curves gives the operating point. Figure 2.11 shows a schematic explanation of this procedure.

To account for the total pressure drop, each of the LSWT local losses K_l (Equation (2.2)) are referred to the test section dynamic pressure q_t, as follows:

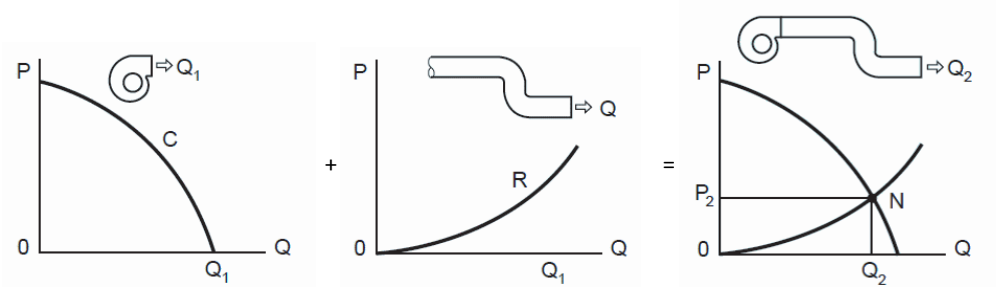

h

Figure 2.11: Schematic view of the operating point in fan driven tubular sections

$$K_{lt} = \frac{\Delta H_l}{q_l}\frac{q_l}{q_t} = K_l\frac{q_l}{q_t}. \tag{2.17}$$

In this equation K_{lt} is the local coefficient loss of one LSWT section referred to the test section velocity v_t. The total rate of loss in the circuit ΔH is obtained by summing the rate of section losses for each of the individual sections multiplied by the test section dynamic pressure q_t.

$$\Delta H = \sum_l K_{lt} \cdot q_t = \sum_l K_{lt} \cdot \frac{1}{2}\rho V_t^2. \tag{2.18}$$

The time rate of energy loss P can be expressed as the product of the total pressure loss times the volume rate of flow through the test section.

$$P = \Delta H \cdot Q = \Delta H \cdot A_t V_t = \sum_l K_{lt} \cdot \frac{1}{2}\rho A_t V_t^3. \tag{2.19}$$

P is the net power that the tunnel drive device must deliver to the airstream to maintain steady conditions. It can be noted here that the fan and motor losses are not considered.

2.1.2 Experimental techniques

A wide variety of aerodynamic tests can be performed in a wind tunnel. Wind tunnel tests (WTT) can be arranged to measure the primary quantities of fluid mechanics, namely pressure, velocity components, temperature and forces and moments acting on bodies. Many other quantities are important in fluid mechanics, such as the vorticity, turbulence intensity, strain rate, stresses, dissipation, enstrophy, to mention just a few examples. These variable can be derived from the velocity field, although direct measurements are sometimes possible. These experimental techniques can be classified according to [13] as shown in Table 2.1.

Other methods such as flow visualization provide information on particular flow patterns. A great variety of such methods make fluid flows visible, in the fluid mechanical laboratory, in industrial environments, and for field experiments. These methods rely mostly on the addition of a tracer material to the flowing fluid, or to the solid surface of the model or wind tunnel walls. This material can be smoke or dye in the case of flowing flows visualizations, or it can be oil impregnated on solid surfaces, sand erosion or wall tufts attached to the model. What is then observable is merely the motion of the tracer, whose motion is considered to be nearly the fluid motion. Some of the flow visualization

Table 2.1: Experimental techniques employed in WTT

Velocity	Pitot and pressure based systems
	Thermal anemometry
	Laser Doppler anemometry (LDA)
	Particle Image velocimetry (PIV)
	Sonic anemometers
Pressure	Manometers and transducers
Temperature	Thermocouples
	Resistive sensors
	Liquid crystals
Forces and Moments	Strain gauges
	Piezoelectric transducers

methods provide qualitative information on particular flow patterns and others allow to measure the flow velocity quantitatively.

In this study both velocity measurement systems are employed. These experimental methods are described in more detail in the following sections.

Velocity measurement systems

Several measurement systems exist to experimentally measure data of velocity components, as previously shown in Table 2.1. Optical measurements like LDA or PIV are non-intrusive techniques that require difficult calibrations, large experimental setups, and clear optical access to the flow. Thermal anemometry and pressure based velocity measurements are the standard technique used to measure time-dependent flow velocity.

Thermal anemometry

For measuring the velocity, the most widely used measurement tool is the hot wire anemometer. A very thin metal wire is heated by an electrical current through the *Joule effect*. The temperature in a metal wire is directly related to its resistance as a linear function of the temperature. When air is blown the wire is cooled, and a closed loop system maintains its temperature constant, (and thus, its resistance) and outputs the required voltage. This output voltage E is a function of the velocity. This operation is known as constant temperature method, but depending on the electronic circuit the hot wire can also operate in constant current and constant voltage.

The main difficulty is the calibration of the system to determine its nonlinear characteristic curve $u = f(E)$ that satisfies the classical King's law, as follows:

$$E^2 = A + Bu^n, \tag{2.20}$$

where u is the velocity of the flow normal to the wire and A, B and n are constants. For common hot-wire probes $n = 0.45$, and A and B can be found by measuring the voltage E, obtained for a number of known flow velocities and performing a least squares fit for the values of A and B which produce the best fit to the data.

This calibration is probably the largest source of measurement error. The hot wire is sensitive mainly to the magnitude u of the velocity orthogonal to the wire so that it is positioned orthogonally to the main flow when a single probe is used. Hot wire systems are very valuable tools due to their accuracy, time resolution, and small size.The sensing elements used in thermal anemometry are either wires or films. Conventional wires are typically 0.5-5 μm in diameter and nominally 0.5-2 mm long. The main drawback is that they are extremely fragile and special care must be taken when handling these instruments. Figure 2.12 shows the typical block diagram of a hot wire anemometer.

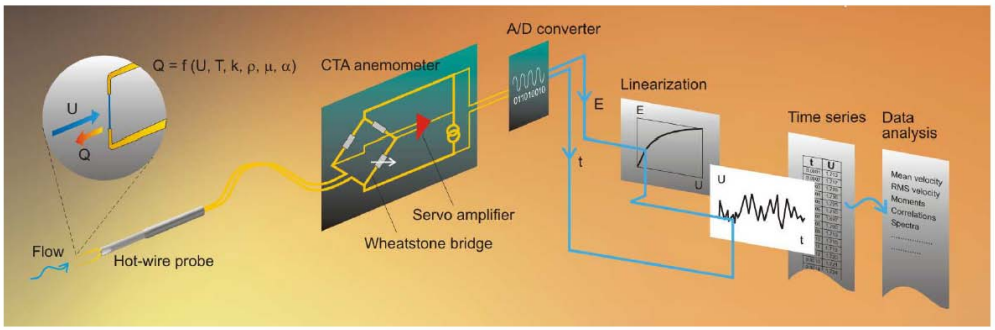

Figure 2.12: Schema of hot wire anemometry (Image taken from Jensen[6])

Pressure based velocity systems

Measurement of dynamic head, in conjunction with use of the Bernoulli equation, is perhaps the most commonly method to determine fluid velocity in a steady, mid-to-high velocity flow. The fabrication of suitable pressure probes is simple and inexpensive, the transducer range may be selected to suit the flow under consideration and a differential measurement of total and static head is sufficient for incompressible flows, in which the density is known.

These type of probes, called Pitot tubes, may be used with a static pressure tapping at the wall, or a static pressure tube. So-called multi-hole probes (MHP) are often used to obtain the flow direction, the static pressure and the dynamic head in flows where the incoming angle is unknown and/or has a large variation in the flow domain. Probes typically consist of a central, stagnation pressure hole or tube, downstream from which

a number of pairs of static pressure holes/tubes are symmetrically displaced, with equal and opposite angles between the orifice faces and the flow. A very common MHP type is the Cobra Probe. The Cobra Probe has three ports equally spaced in a triangular configuration around a central port. The outside holes are located on planes that are at 45° angles with respect to the plane on which the central hole is located, as seen in Figure 2.13.

[h]

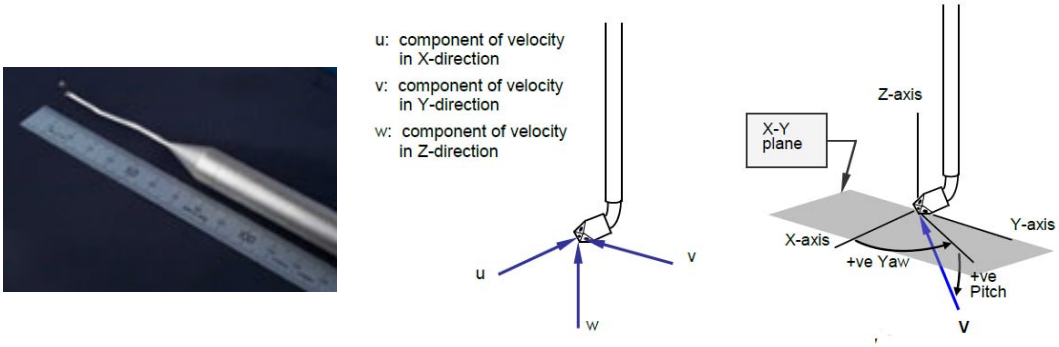

(a) (b) (c)

Figure 2.13: Cobra probe details (a) Cobra probe size. (b) Flow axis system with respect to the probe head. (c) Positive flow pitch and yaw angles. (images taken from TFI website [7])

When a MHP incorporates miniature dynamic pressure transducers near its tip time-dependent velocity measurements are possible. The MHP measures pressure at multiple points along the body of the probe and uses empirical relations between the pressure ports to determine the velocity components. The probe can be calibrated by recording data at various known incidence angles and velocities and calculating single-valued dimensionless pressure ratios. More detailed information on the calibration method can be found in [49].

To reduce the errors introduced in the determination of the velocity several considerations should be taken into account. First, the disturbance of the support or traversing mechanism to the incoming flow should be as low as possible. The devices need to be properly aligned to the flow velocity within the range of yaw acceptance. It is also assumed that dimensions of the device are negligible compared to the incoming flow length scales. The flow must be free of particles and condensation which could adversely affect the device readings. Finally, the measurements have to averaged over a sampling time long enough to give convergence to the true velocity, having accounted the response of the probe. The response time of MHP probes is lower than hot wire anemometers. However, MHPs are much more robust.

2.1.3 Flow quality requirements

For decades, WTT has been conducted in test section environments that have not been adequately or consistently documented. Since wind tunnel flow quality can adversely affect test results, accurate and consistent flow quality measurements are required, along with an understanding of the sources, characteristics, and management of flow turbulence. Wind tunnel disturbances must be measured to the highest accuracy to allow the aerodynamicist to distinguish between aerodynamic, aeroelastic, and Reynolds number effects in order to optimize wind tunnel model designs.

According to Owen [50], wind tunnel flow irregularities can usually be divided into four main categories; spatial non-uniformities, swirl, low-frequency unsteadiness and turbulence. Most notable recent efforts to determine flow quality standards for low speed flow were conducted by the National Wind Tunnel Complex (NWTC) project team consisting of members from the US government, industry and academia. The following Table 2.2 summarizes the parameters defining the flow field and accuracy requirements for LSWT [51].

Table 2.2: NWTC flow quality requirements for an open jet LSWT

Parameter	Open jet LWST
Dynamic pressure distribution	$<\pm$ 0.1 %
Stream angle deviation	$<\pm$ 0.1°
Turbulence	<0.2 %

A decision must be taken whether if previously defined flow quality goals (such as those established for the proposed NWTC) are necessary and if they can be achieved in a cost-effective manner. Ideally, in an empty wind tunnel test section free from struts and fairings, the flow outside the wall boundary layers would be uniform and smooth, without cross flows or turbulence. Since this ideal scenario is unachievable in reality, the key question is what flow quality is acceptable at a reasonable tunnel performance level and operating cost. In fact, Barlow *et al.* [2] specifies that the variation in dynamic pressure q should be less than 0.50 % from the mean, which corresponds to a 0.25 % variation in velocity. Regarding the flow angle deviation, it would be desirable to have a variation below $\pm$ 0.1°, but it is often necessary to accept maximum variation to $\pm$ 0.2°, due to the difficulty of achieving such tight requirements.

It should be noted here that most of LSWT were built for aviation industry, where the flow is attached and highly accurate results are required. On the other hand, these quality requirements has less significance in other WTT where the flow is more or less separated, such as in situations around stall or in bluff body aerodynamics. In this context, other

facilities like general-purpose LSWT, environmental wind tunnels or automobile wind tunnels present different flow characteristics. The specifications for the flow properties for vehicle wind tunnels have not yet been formulated on a rational basis. However, the following data are typical for existing tunnels [13]:

- local deviations from average wind speed $\Delta u/U_\infty = (u - U_\infty)/U_\infty \leq \pm\ 0.5\ \%$;
- angularity in pitch and yaw $\alpha, \beta \leq \pm\ 0.2°$;
- turbulence level $T_u = \sqrt{\overline{u'^2}}/U_\infty \leq \pm\ 0.5\ \%$;

Regarding the study of airfoils at low Re number, the above requirements are acceptable except for the turbulence intensity. Since low Re number airfoil performance is highly dependent on the behavior of the laminar boundary layer, low turbulence levels within the LSWT test section are necessary to ensure that laminar flow does not prematurely transition to turbulent flow. According to [52], a turbulence intensity of 0.1 % is sufficient for low Re airfoil measurements, as it is known that higher turbulence level can cause the transition of the boundary layer on a flat plate. Ideally, the turbulence level in the wind tunnel should be below this value to reduce the discrepancies when comparing data between different wind tunnel environments. In practice, such a low turbulence level is difficult to achieve and wind tunnel airfoil experiments with higher turbulence levels can be found in literature [53, 54].

2.2 LSWT design

In the subsequent chapters the dimensional analysis of the current LSWT design is accomplished together with the pressure drop calculation through the LSWT sections. This study is then used to the selection of the appropriate fan to produce the required pressure rise at the desired volumetric flow.

The initial design specifications are based on the wind tunnel dimensioning principals given in details in the book entitled *Low-Speed Wind Tunnel Testing* by Barlow *et al.* [2]. As stated in this reference work, the first step when designing a wind tunnel is to determine the size and shape of the test section. This dimension is given by the blockage ratio BR (the relation between the area of the drag item and the test section area). Once the test section dimension is defined, the rest of the LSWT dimensions can be determined, taking into account the limited space available in the room where the LSWT is located.

In the current design, the cross-section area of test section is dimensioned as large as possible. The shape of the test section is chosen to be rectangular to ease the manufacturing of the rest of LSWT sections and the assembling of the experimental equipment. The

test section dimensions are then set to 0.75 m width per 1 m height. Theoretically, the length should be sufficient to let the flow be fully developed after the drag item. Given the restrictions of the room where the LSWT is placed, this length is limited to 3 m, which leads to a length-to-hydraulic-diameter ratio greater than 2, commonly employed in the aeronautical field.

The settling chamber is the entry section and its function is to straighten the flow and reduce turbulence intensity. With this purpose, the settling chamber is composed of a flow straightener or honeycomb followed by two screens. The following Table 2.3 summarizes the design parameters of the honeycomb and screens. The screens are parametrized to obtain a solidity between 0.3-0.4 [29, 30].

Table 2.3: Honeycomb and screen design parameters

Honeycomb	Length	$L_h = 90$ mm
	Mesh size	$M_h = 12.7$ mm
	Number of cells	≈ 29000
Screen 1	Mesh size	$M_1 = 4.63$ mm
	Wire diameter	$d_1 = 0.8$ mm
	Solidity	$\sigma_1 = 0.32$
Screen 2	Mesh size	$M_2 = 1$ mm
	Wire diameter	$d_2 = 0.2$ mm
	Solidity	$\sigma_2 = 0.36$

The mesh size of the flow conditioning devices is consecutively finer in order to gradually reduce the size of the largest eddies while keeping smallest of mesh width to be about 5-15 times smaller than the honeycomb mesh size [33]. The settling chamber needs to be long enough to settle down before entering the contraction section. Therefore, the distance between screens is also defined to let the turbulence return to isotropy [34]. In addition, and inlet radius is included at the entrance of the settling chamber to avoid the formation of the *vena contracta* phenomena (Figure 2.5).

Contraction cone or nozzle takes the flow from the settling chamber to the test section while increasing the average speed. The contraction ratio CR (area between inlet and outlet of the contraction) is 6.25. The wall profile is design to have zero first and second derivatives, and inlet and outlet profile radius proportional to the area. The length is 2 m to enable the control of the boundary layer growth while preventing the boundary layer separation.

The diffuser extends from the downstream end of the test section to the fan section. Ideally, its length should be 3-4 times the test section length to reduce the speed with

as little loss energy as possible by allowing a gradual pressure recovery. However, due to space limitations the diffuser is shorter and consequently, the increased exit loss at the outlet is assumed by the fan device.

The subsequent section in the wind tunnel is the fan power section followed by the silencer. Figure 2.14 shows the 3D CAD design of the wind tunnel tunnel in comparison with the constructed and installed wind tunnel at MU. It has an overall length of 10 m and height of nearly 3 m from the floor in the inlet section with a fan section diameter of 1250 mm.

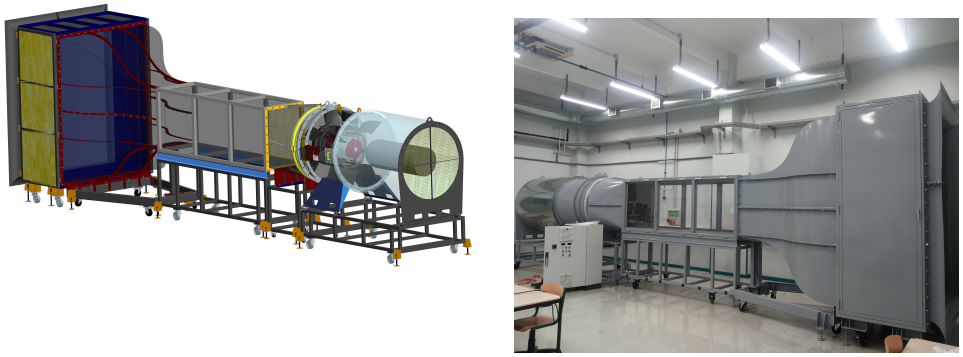

(a) (b)

Figure 2.14: LSWT design (a) 3D CAD design (b) LSWT facility installed at MU

2.2.1 Fan power requirements

Once the dimensions of each LSWT section are determined, the next step is to compute the pressure drop throughout each LSWT section. A maximum flow rate of about 30 m^3/s is desired to be produced by the fan, which results in a maximum of ≈40 m/s velocity in the test section. This mass flow rate in conjunction with total pressure drop through the LSWT at full speed of the fan defines the operation point of the system (Figure 2.11).

The energy losses caused by the honeycomb and screens are calculated based on expressions of the Section 2.1.1. The pressure loss in straight test sections and in the diffuser can be estimated using theoretical expressions given by Barlow *et al.* [2] with accuracy. However, the pressure loss through the contraction section leads to a deeper analysis. The analytical solutions found in bibliography do not predict accurately the secondary losses as they do not take into account the effect of the curvature radius at the inlet and outlet section. This has a significant effect on the wind tunnel pressure drop

calculation, as concluded in a preliminary study of the present author [44]. The CFD predictions performed in this work were necessary to account for all minor losses (due to cross sectional change) and major losses (due to wall and internal friction) together for a design purpose. Additional losses are expected also in the inlet and outlet section as it is an open circuit LSWT. According to the manufacturer, the silencer gains a pressure loss to the system. The pressure loss due to the drag item inside the test section may cause some losses as well. Table 2.4 indicates the estimated pressure loss through each LSWT section.

Table 2.4: LSWT sections' loss coefficients

LSWT section	K_{lt}	K_{lt} (%)
Inlet	0.002	0.2
Honeycomb	0.040	4.4
Screen 1	0.016	1.8
Screen 2	0.023	2.5
Contraction	0.096	10.5
Test Section	0.059	6.5
Safety screen	0.131	14.4
Diffuser	0.036	4.0
Fan Section	0.012	1.3
Silencer	0.072	7.9
Safety screen	0.049	5.4
Exit	0.374	41.1
$\sum K_{lt} = 0.910$		

K_{lt} is the local loss coefficient of the corresponding LSWT section referred to the test section velocity (Equation (2.17)). It is noteworthy that that safety screens located at the end of the test section and in the exit section have a considerable pressure drop, as they are placed in a high velocity section. In contrast, turbulence screens, which have a lower porosity compared to safety screens, or even the honeycomb, have a lower pressure drop as the velocity is much lower in the settling chamber. The contraction section has also a significant pressure drop, and it is mainly caused by the minor losses due to the gradual cross sectional change.

The diffuser length is shorten due to space limitations, and therefore, there is no gradual pressure recovery and there is a large loss of kinetic energy of the exiting flow. This is clearly visible in the pressure drop at the exit section, which is the 41.1 % of the total pressure loss in the LSWT. In fact, exit losses are the main inconvenient of open circuit wind tunnels and the reason why there are no large facilities using this

configuration [2].

Taking all these considerations into account a total loss coefficient of $\sum K_{lt} = 0.910$ is considered with empty wind tunnel. The drag item is not included in the total pressure loss estimation for comparison reasons in the later stage (2.3.1). With this information, a 37 KW axial fan provided by BALTOGAR company is selected. Figure 2.15 shows the operating curve of the fan together with the system characteristic curve. The intersection of these curves is the operating point of the system, which results in a flow rate of $Q = 28.7$ m^3/s (a velocity in the test section of 38.2 m/s) and a total pressure drop of $\Delta H = 816$ Pa.

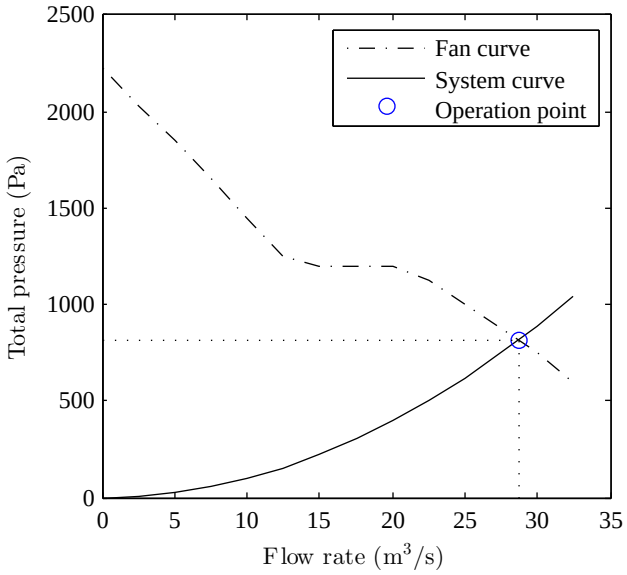

Figure 2.15: LSWT operating curve at maximum rotational speed of the fan

2.2.2 LSWT setup

In wind tunnel testing (WTT), it is necessary to collect and monitor the aerodynamic data obtained from the sensors. A proper positioning of velocity and pressure sensors and the model itself is essential to ensure the reproducibility and accuracy of the data acquired.

For measuring velocity and pressure, a pressure based system is chosen as a more robust alternative to hot wire anemometry. Although hot wire anemometry provides a higher time resolution, the MHP type known as cobra probe provided by TFI company (see Figure 2.13) can acquire data at 2500 Hz, which is enough for capturing the large scales in the flow field and other transient phenomena, such as vortex shedding.

TFI company stated that the accuracy of cobra probe is within ±0.5 m/s and ±1° pitch and yaw and remains relatively accurate to greater than 30 % turbulence intensity. However, this data is considered for a wide yaw and pitch angle range from −45° to 45° and velocities up to 90 m/s. The error decreases for low velocity ranges and low angularities. The accuracy analysis of the TFI cobra probe performed by Johnson [55] reveals that measurement errors for 50 m/s at zero pitch and yaw angles are minimal. Therefore, this instrumentation is suitable for its use in LSWT calibrations, 2D flow mapping, wind engineering boundary layers and characterization of highly turbulent flows.

In addition to the velocity and pressure measurement system, a PT-100 device outputs the temperature of the room and the atmospheric pressure is obtained through a barometer sensor. This data is then introduced in the acquisition software for the application of the corresponding calibration curves.

In most wind tunnels a traversing mechanism of two or more axis is used to set the sensor in the desired position inside the test section. Moreover, these automated systems reduce the setup time of the experimental tests. Figure 2.16 shows the positioning system installed at the top of the test section.

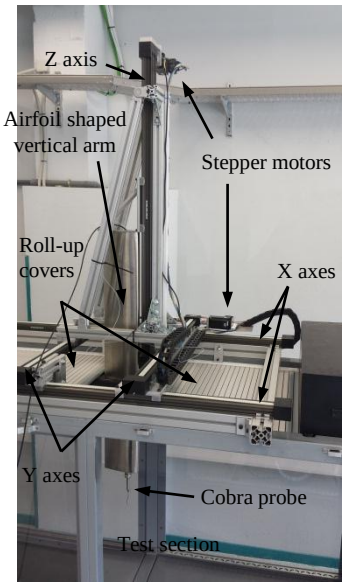

Figure 2.16: Three axis positioning system installed at the top of the test section

The positioning system is a gantry comprised of several toothed belt axes from IGUS company. Two longitudinal axes are first assembled above the test section ceiling to allow the system to move in X direction. Two carriages are mount on each axis so that the axes conforming the Y direction can be assembled to them. An aluminum profile

structure is mounted onto the Y carriages to fix the Z axis. Two aluminum roll-up covers assembled to the longitudinal axis cover the ceiling when the traversing mechanism is moving. Each axis is driven by a NI ISM 7400 series Nema 23 stepper motor that allows positioning the speed sensor (Cobra probe from TFI company) inside the test section. The vertical traversing arm that enters the test section has an airfoil shape to minimize the drag force while disturbing the flow as least as possible.

A 4-axis motion control is developed via LabView environment. The embedded NI cRIO-9031 controller together with the 4-axis SISU 1004 interface module is responsible for controlling at real-time the stepper motors. Additionally, a 4 slot NI cDAQ-9174 chassis is connected via USB to the PC in order to acquire the signals from the sensors. The following modules are used; NI9215 for the Cobra probe and NI 9219 for PT-100 temperature sensor. More information on the software and hardware used in this study can be found in [56].

A graphical interface allows to communicate the motion control while the results are monitored. The programming code uses a state machine structure to synchronize the different tasks. This way obtaining 2D maps of velocity contours, boundary layer studies, measurements of turbulent wakes developed by the object of study, or any other scanning in space is fully automated.

2.3 LSWT validation

Once the LSWT is manufactured and the experimental setup is arranged, it is necessary to validate the design. In other words, it is necessary to check if the flow quality in the test section meets the requirements established in Section 2.1.3. First, the dynamic pressure of the test section for different velocities up to the maximum power of the fan is measured to obtain the power factor λ of the wind tunnel. Then, turbulence intensity, flow uniformity and angularity and other relevant measurements such as boundary layer thickness in the LSWT floor and the longitudinal pressure gradient through the test section are shown.

2.3.1 WT power factor

The power factor λ of the wind tunnel is a measure of the total pressure loss of the LSWT circuit. According to Lindgren and Johansson [57] it is defined as follows:

$$\lambda = \frac{\Delta H}{\eta_f q_1} = \frac{P_m \eta_m}{A_1 U_1 q_1}, \tag{2.21}$$

where q_1 is the dynamic pressure measured in the test section, A_1 and U_1 are the cross-section area and the flow speed in the test section, P_m is the power input from the motor and η_f and η_m are the fan and motor efficiency factors respectively. In Equation (2.21), the numerator is the electrical power input required to deliver to the airstream to maintain steady conditions, and thus, the power factor λ is an estimation of the energy balance in the LSWT. For closed return LSWTs λ is nearly always less than unity, while in open circuit configuration is more than unity.

In Table 2.5 the velocity of the test section is obtained for different rotation speeds of the fan. A Variable Frequency Drive (VFD) controls the rotation speed of the fan and outputs the required power. The obtained power factor decreases as the wind tunnel test section speed is increased, indicating that the energy balance is poor at low rpm. This is caused mainly due to the fact that the fan efficiency decreases for low rotational speeds.

Table 2.5: LSWT power factor as a function of fan rotational speed in rpm

rpm	150	300	450	600	750	900	1050	1200	1350	1500
P_m (kW)	11.8	12.2	12.7	13.2	14.1	15.5	20.5	25.6	31.2	37.0
U_1 (m/s)	3.8	7.6	11.6	15.4	19.0	23.0	26.4	30.2	33.7	37.4
λ	443.7	56.2	16.5	7.4	4.2	2.6	2.3	1.9	1.7	1.4

At 50 Hz, the motor operates at full capacity and the fan manufacturer establish that the efficiency of the fan η_f is 0.72 at that rpm. From Equation (2.21) it is possible to obtain that the total pressure loss is $\Delta H \approx 886$ Pa for a 37.4 m/s test section velocity. The pressure drop is a bit higher compared to the initial estimation of the operating point of the wind tunnel (Figure 2.15 in Section 2.2.1). An error of 8 % is committed in the total pressure drop calculation, what leads to a lower maximum velocity in the test section. This error is found to be acceptable for wind tunnel conventional designs [2].

The power factor of the wind tunnel is important, but is never nearly so important as other factors that define the appropriate quality of flow, such as the turbulence intensity [2].

2.3.2 Turbulence intensity

One of the most important aspects of the flow quality in a wind tunnel is the level of turbulence intensity. During the design of the LSWT, special care is taken to ensure that the honeycomb, screens and the contraction produce the required turbulence damping.

To measure turbulence intensity the Cobra probe is placed centred in the empty test section. The turbulence intensity is defined as $I = \frac{u_{rms}}{U}$, where U is the mean velocity

and u_{rms} is calculated from the data using a sample frequency of 2500 Hz with a total of 37500 samples as:

$$u_{rms} = \left(\frac{1}{N} \sum_{i=1}^{N} (u_i - U)^2 \right)^{\frac{1}{2}}. \tag{2.22}$$

Considering that there will be always flow variations with wavelengths of several meters containing a substantial part of the total turbulent kinetic energy, a high-pass filter (HPF) is included in the data analysis. The cut-off frequency f_c is defined based on the work by Lindgren and Johansson [57] as $f_c = \frac{U}{\lambda_c}$, where λ_c is the cut-off wavelength. The limiting wavelength is this work is chosen to be the hydraulic diameter of the test section. The purpose of the HPF is to remove the influence of length scales larger than the specified integral scale on the results.

Figure 2.17 shows the evolution of the turbulence intensity depending on the flow speed inside the test section. For velocities below 5 m/s, turbulence intensity increases to more than 0.5 %. Therefore, this is the lower limit that can be considered for low Re airfoil measurements [53, 54]. As the velocity increases the turbulence intensity stays within 0.3 % or even below 0.2 % if a HPF is applied to the measured data.

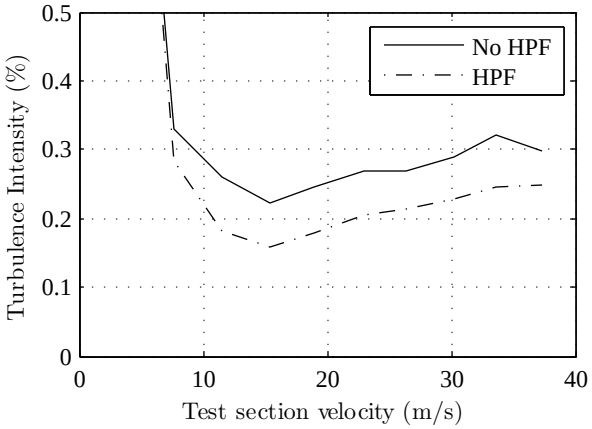

Figure 2.17: Turbulence intensity in the empty test section as a function of velocity

The data in Figure 2.17 is obtained for the center of the test section. However, it is interesting to know how the turbulence intensity varies in other points at the same cross-plane. This is obtained by performing a 2D map by taking measurements with the Cobra probe at different locations. The cross-plane is located at the middle of the empty test section, where the model is situated when aerodynamic forces are measured. A distance of 200 mm is kept from the bottom and top walls while 175 mm is kept from side walls to minimize their influence on the results. A total of 34 points are taken with

a spacing of 100 mm in Y and Z direction. Figure 2.18 shows a sketch of the location of the measurements.

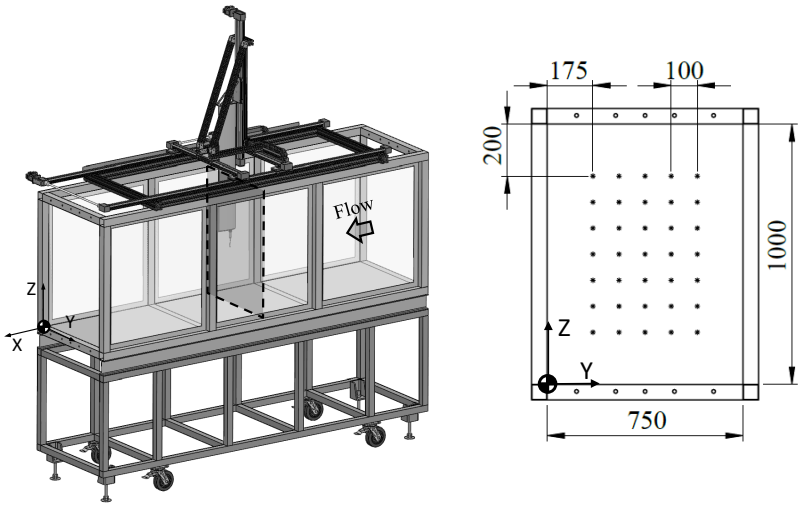

(a) (b)

Figure 2.18: Location of the experimental measurements (a) Cross-plane located at the middle of the empty test section (b) Points were the measurements are taken to obtain the 2D mapping (dimensions in mm)

The following Figures 2.19 and 2.20 show the streamwise turbulence intensity obtained for both unfiltered and filtered data and for 10, 20 and 30 m/s. For 10 m/s, the turbulence intensity stays in the range of $0.25 - 0.3$ % for almost all the range studied. It is only a slight difference in the bottom left corner where values close to 0.4 % are measured. If the HPF is applied, the 2D contour is almost uniform within the cross-plane with turbulence intensity values below 0.2 %. These values of turbulence intensity are also measured when the velocity is increased.

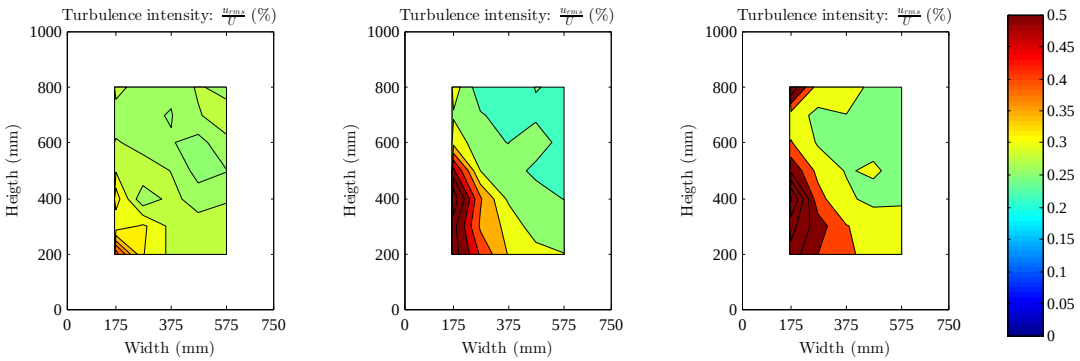

(a) (b) (c)

Figure 2.19: Streamwise turbulence intensity obtained at the cross-plane located at the middle of the empty test section (Non filtered data). (a) 10 m/s (b) 20 m/s (c) 30 m/s

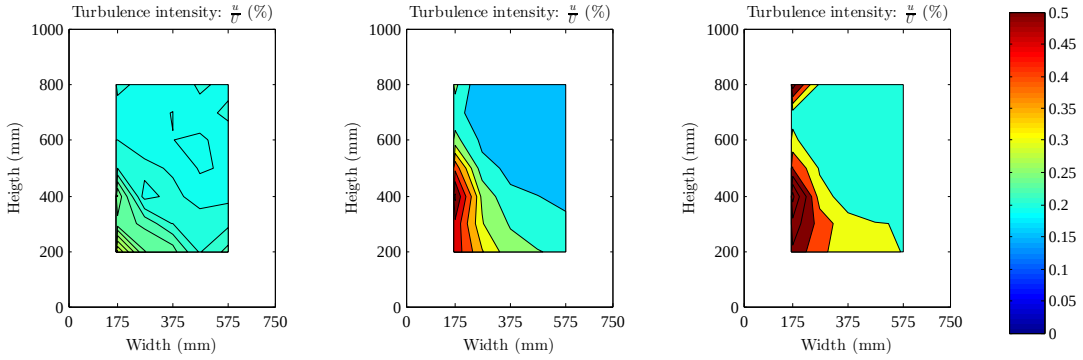

(a) (b) (c)

Figure 2.20: Streamwise turbulence intensity obtained at the cross-plane located at the middle of the empty test section (filtered data). (a) 10 m/s (b) 20 m/s (c) 30 m/s

However, for 20 m/s and 30 m/s, 2D maps show more irregular patterns, specially in the left side wall of the wind tunnel. The flow may be affected by the wall in this zone and turbulence intensity values of more than 0.5 % are measured locally. Since this zone is not in the working region of the test section, where the model is located, it can be said that the flow has enough quality for low Re number airfoil measurements.

2.3.3 Flow uniformity and angularity

The Cobra probe is used to determine the flow uniformity and angularity of the incoming velocity in the test section. Prior to the experimental tests, an uncertainty analysis is performed to asses the accuracy of the measurements. Figure 2.21 displays the error committed for the case of 10 m/s. Up to three repetitions are performed independently for the 35 points that comprised the 2D map (Figure 2.18). For each point, the mean value of the velocity is obtained as $U_{mean} = \frac{1}{N}\sum_{i=1}^{N} U_i$, being N the number of repetitions. Then, the local error is estimated as $\frac{\max(|U-U_{mean}|)}{U_{mean}}$ (%). A similar procedure is followed to calculate the error in yaw and pitch measurements. The yaw β and pitch α angle error is estimated based on the maximum deviation from the mean value ($\beta_{mean} = \frac{1}{N}\sum_{i=1}^{N} \beta_i$ and $\alpha_{mean} = \frac{1}{N}\sum_{i=1}^{N} \alpha_i$) between the three measurements ($\max(|\beta - \beta_{mean}|)$ (°) and $\max(|\alpha - \alpha_{mean}|)$ (°)).

In general, the colored contour plots show that the error committed by the cobra probe at each point is less than the flow quality requirements that needs to be accomplished (Section 2.1.3). The maximum permissible deviations are of the order of 0.5 % in terms of flow uniformity and sensor has an uncertainty of 0.05 % for speed. Regarding the yaw and pitch angles, a maximum angle deviation of 0.2° is admissible and an average error of 0.05°is obtained. There are some points closer to the walls of the tunnel where

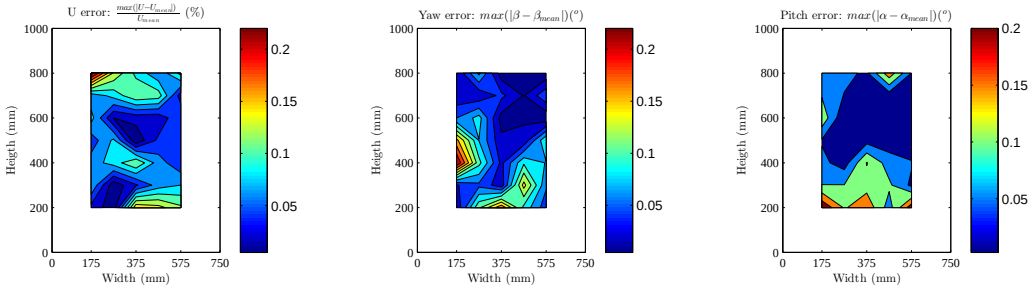

(a) (b) (c)

Figure 2.21: Measured errors at a free-stream velocity of 10 m/s for (a) flow velocity U, (b) yaw angle β and (c) pitch angle α

the error is somewhat higher than these values. This suggests that the cobra probe is more precise when the flow is well addressed. This should be taken into account when analyzing the local deviations in these points.

The uniformity of the flow is the variation of velocity that exists in the test section. Other authors also relate the uniformity as total pressure variation [57], or dynamic pressure variation [52]. In this work, the flow uniformity is related to $\frac{u-U}{U}(\%)$ [13], where u is the local velocity and U is the free stream velocity. Figure 2.22 show the 2D mappings obtained at different velocities. The point where the measurements are taken are the same as in turbulence intensity mappings (Figure 2.18).

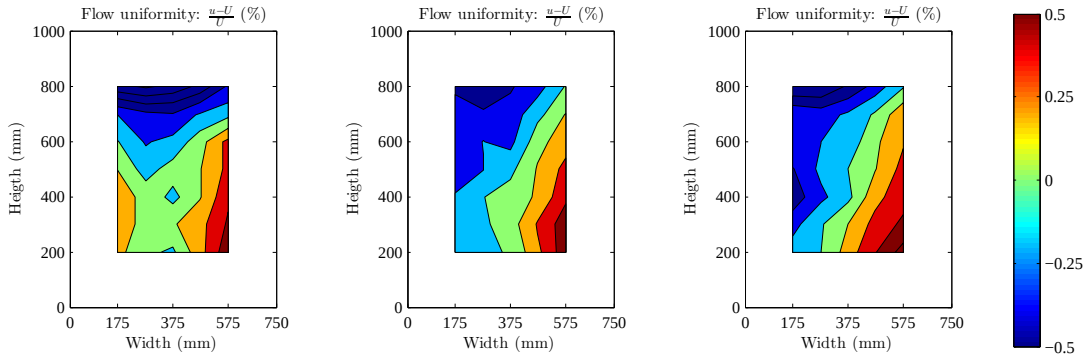

(a) (b) (c)

Figure 2.22: Flow uniformity across the cross-plane located at the middle of the empty test section. (a) 10 m/s (b) 20 m/s (c) 30 m/s

From the uniformity contours, it can be seen a slight asymmetry in the results for the velocities tested. In the right wall, values next to 0.5 % are encountered, specially at the bottom right corner. On the other side, values close to -0.5% are found near the top and left of the working section. These relative differences are within the acceptable range desirable for LSWTs [13, 2].

Apart from a good flow uniformity, it is important to have the flow parallel to the test section. This requirement is of great relevance for airfoil testing. A small change in the incoming angle velocity can alter the effective angle of angle of attack, what would result in a deviation of lift and drag measurements. The yaw and pitch angles are obtained using the Cobra Probe and the axis system presented in Figure 2.13. Calibration curves supplied by the manufacturer are used to determine the flow angle at each location. Figures 2.23 and 2.24 show the contours of Yaw and Pitch angle obtained.

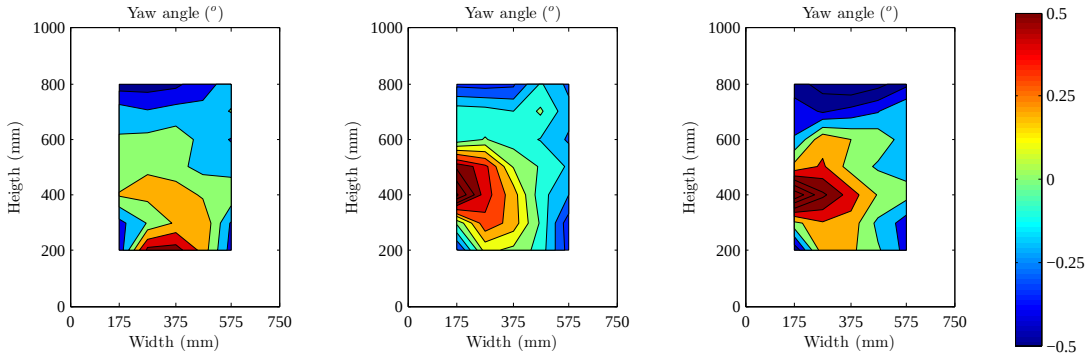

(a) (b) (c)

Figure 2.23: Yaw angle variation across the cross-plane located at the middle of the empty test section. (a) 10 m/s (b) 20 m/s (c) 30 m/s

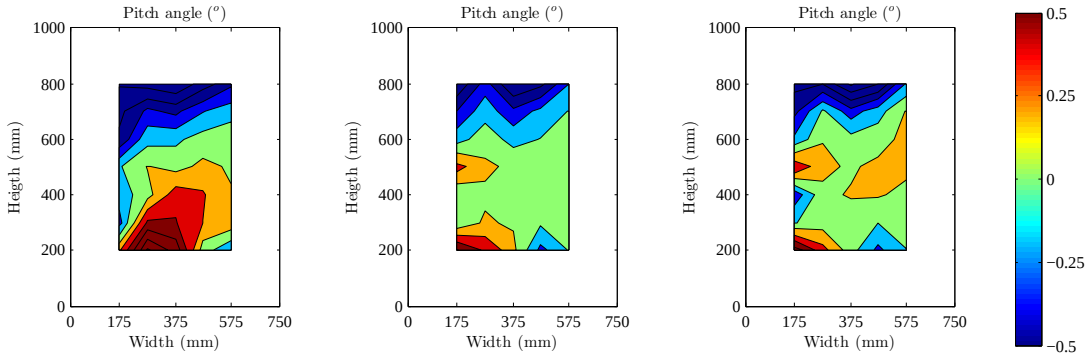

(a) (b) (c)

Figure 2.24: Pitch angle variation across the cross-plane located at the middle of the empty test section. (a) 10 m/s (b) 20 m/s (c) 30 m/s

According to Barlow *et al.* [2], a flow angle variation of ±0.2° is acceptable. The current measurements meet this requirement, although relatively large flow angles are recorded locally near the floor and the upper wall in the case of 10 m/s, in the left side wall for the case of 20 m/s and in the left and top wall for 30 m/s. In general, the flow presents an acceptable angularity in the working region of the test section.

2.3.4 Boundary layer

As the flow proceeds downstream, turbulent boundary layers grow further from the wall. Calibrations of the wind tunnel should not be taken inside the boundary layer. To know the width of the boundary layer, a set of different measurements are taken close to the wind tunnel floor at different positions, X=1.25 and 1.75 m from the entrance of the test section, just before and after the model is to be placed. Figure 2.25 shows the points where data is recorded. A total of 8 points are taken with decreasing spacing towards the wall for each position along the X axis.

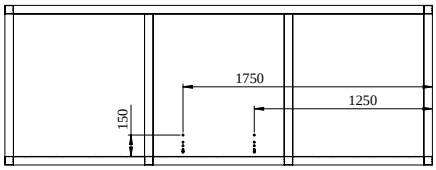

Figure 2.25: Points were the measurements are taken to obtain the boundary layer profiles (dimensions in mm)

Theoretically, the boundary layer thickness is the distance from the wall to a point where the flow velocity has reached free stream velocity. This distance is defined as the point y where velocity has reached 99 % of the free stream velocity ($u(y) = 0.99U$). In practice, it is difficult to find the exact boundary layer width due to error of the measurement technique and the flow uniformity in the test section. For this reason, the evaluation of the turbulence intensity together with the flow velocity near the wall can aid to specify the boundary layer thickness. Figures 2.26 and 2.27 shows the boundary layer profile and the turbulence intensity levels measured for three different test section velocities.

The boundary layer width can be related to the point where the boundary layer profile varies significantly its slope and enters the upper and lower limits of the free stream velocity. These limits are defined based on the assumption that free stream velocity is considered to be within a deviation of 1 %, what results in a lower bound of $u/U = 0.995$ an and upper bound of $u/U = 1.005$. It can be observed that the lower bound intersects the boundary layer profile between 40-50 mm for the case of 10 m/s, while for higher velocities it is roughly $\approx$ 40 mm.

It can be found on Figure 2.27 how the boundary layer slightly grows along the streamwise length of the test section, since the profiles presented reach lower u/U ratios and higher turbulence levels. This indicates that a bigger portion of the boundary layer is captured at this location, or, in other words, the boundary layer is thickened.

The results obtained can be compared to the thickness given by a turbulent boundary

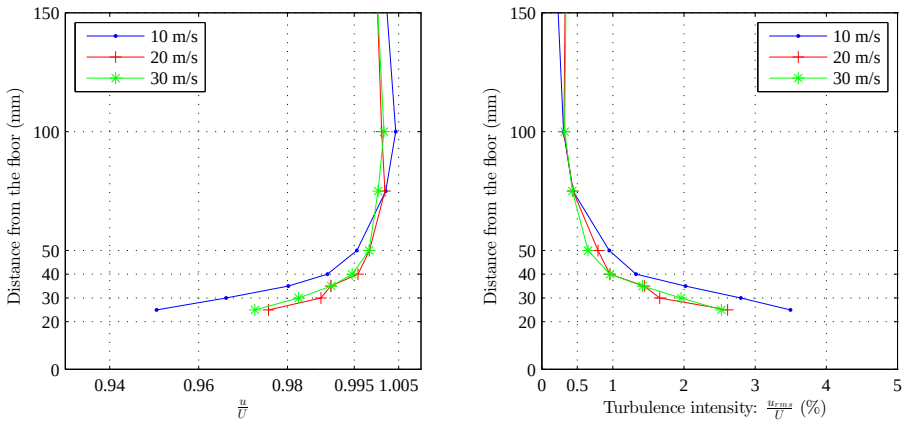

(a) (b)

Figure 2.26: Boundary layer profiles obtained at 1250 mm from the entrance of the test section (a) Local velocity u over free stream velocity U ratio (b) Streamwise turbulence intensity

layer over a flat plate [58]:

$$\delta \approx 0.37x/Re_x^{1/5}, \tag{2.23}$$

where δ is the thickness of the boundary layer, x is the distance downstream the start of the boundary layer and Re_x is the Reynolds number based on x. Table 2.6 shows the values obtained by Equation (2.23) for the cases analyzed.

Table 2.6: Turbulent boundary layer height obtained by Equation (2.23).

δ (mm)	U=10 m/s	U=20 m/s	U=30 m/s
x=1250 mm	30	26	24
x=1750 mm	40	35	32

The values measured are roughly 10 to 15 mm higher compared to the theoretical values and same trends can be observed. The highest boundary layer is obtained for 10 m/s and it is reduced for higher velocities. The boundary layer thickens between 8-10 mm from one location to the other. A lower spacing between the points where the experimental data is obtained may help to find exact location of boundary layer limit. However, since the aim of the study here is to know approximately the limits of working region of the test section, the profiles given are assumed to be enough.

Due to the thickening of the boundary layer toward the exit the effective area of the test section is reduced. This reduction in the effective area results in an increase of the test section free-stream velocity, and consequently the static pressure varies along the test section length.

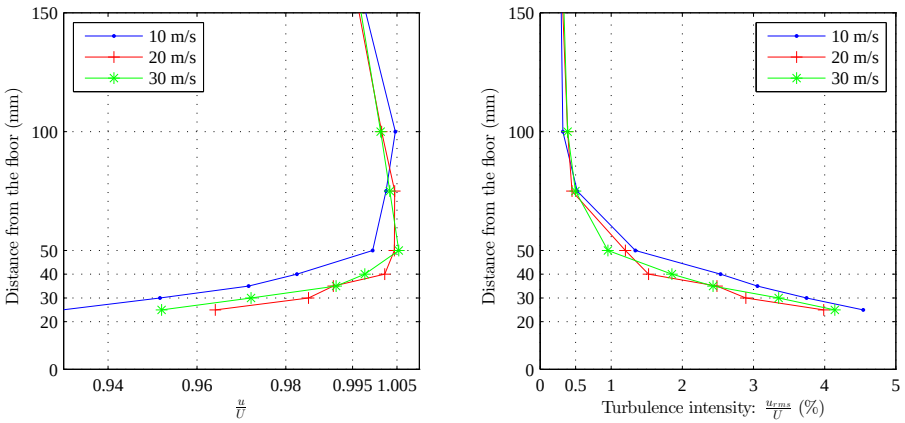

(a) (b)

Figure 2.27: Boundary layer profiles obtained at 1750 mm from the entrance of the test section (a) Local velocity u over free stream velocity U ratio (b) Streamwise turbulence intensity

2.3.5 Longitudinal pressure gradient

The static pressure gradient along the test section must be known in order to make necessary buoyancy corrections. Figure 2.28 shows an sketch with the points measured to analyze the pressure gradient in X direction. The points are located at the midplane of the test section (symmetry plane). The first point is considered at the medium height of the test section at 500 mm and at 1000 mm from the entrance. The points are placed with a spacing of 100 mm.

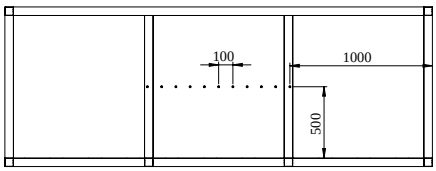

Figure 2.28: Points were the measurements are taken to obtain the longitudinal pressure gradient (dimensions in mm)

Figure 2.29 plots the pressure gradient along the test section. For low velocities, the pressure gradient is almost negligible as the pressure is quite low. In contrast, the pressure deficit along the test section length becomes significant as the test section velocity is increased since the dynamic pressure evolves exponentially. Consequently, the static pressure further increases and the longitudinal pressure gradient has greater effects, reaching values up to 24 Pa per test section meter.

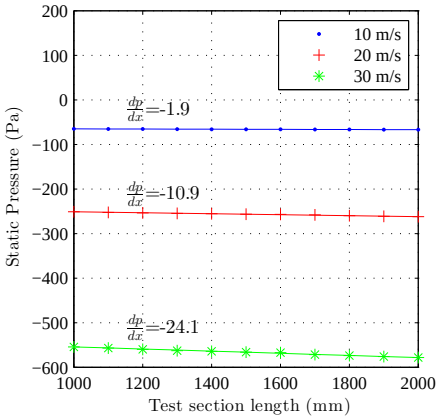

Figure 2.29: Longitudinal pressure gradient obtained at 10, 20 and 30 m/s of test section velocity

2.4 Conclusions

In this chapter the design data of the LSWT installed at Mondragon Unibertsitatea is provided. The pressure drop calculations through the LSWT sections are reliable enough to properly define the fan power requirements, as it is verified in the wind tunnel power factor measurements.

The assembled 4-axis motion control system automates the positioning of the Cobra probe in the test section and the rotation of the model to be tested ensuring a good repeatability of the measurements. The developed graphical interface in LabView environment enables to control the positioning system while monitoring aerodynamic data in real time while it is stored for its later analysis.

Finally, the measurements performed in the LSWT validation meets the aerodynamic flow quality requirements for the experimental testing of airfoils at low Re numbers. Therefore, the one of the main objectives of this research project is successfully achieved.

Chapter 3

Wind tunnel testing airfoils at low Re number

Low speed wind tunnels are commonly designed and constructed to study aerodynamic devices operating at low Re numbers, since higher regimes can only be obtained in relatively large and fast wind tunnels. In the last decade, due to the development of vertical axis wind turbines (VAWT), small horizontal axis wind turbines (HAWT), small unmanned aerial vehicles (UAV), micro-aerial vehicles (MAV), remotely piloted vehicles (RPV) sailplanes, or even subscale testing of many full scale systems, there is a growing interest in the study of blade profiles operating at low Re regime. Experiments in this regime are very useful since the aerodynamic design of airfoils at low Re numbers cannot simply be scaled down from larger ones. Flow characteristics at low Reynolds numbers are vastly different from those found in high Reynolds numbers. The main difficulty associated with analyzing flow in this regime is laminar flow separation. This phenomenon is an important scale effect that must be understood by designers and researchers.

Due to the difficulties encountered to overcome the limitations of numerical models when dealing with airfoils at low Reynolds numbers, wind tunnel tests provide a valuable information for the design of blade profiles of aerodynamic devices. The current chapter is focused on setting up a experimental methodology to study airfoil performance at low Re numbers.

3.1 Introduction

Fluid flows in nature and technology normally depart from laminarity and are turbulent in the majority of cases. The parameter which is fundamental to the transition from laminarity to turbulence is the Reynolds number, which determines the ratio of inertial

to viscous forces and carries information on the overall behavior of the flow field. When the Reynolds number is below a critical value Re_c, the viscous forces are high enough to produce instabilities in the flow. Whenever $\mathrm{Re} > \mathrm{Re}_c$, the flow will start to exhibit all the features of developed turbulence. Empirically, it has been found that in external flows $\mathrm{Re}_c \approx 3 \times 10^5$ [13]. Rather than a fixed value, transition from laminar to turbulent condition arises within a range of critical values, depending on the boundary and initial conditions.

When dealing with airfoils at high Re numbers, the assumption that the flow over the entire boundary layer is fully turbulent is quite realistic, since the laminar flow region near the stagnation point is very small. The onset of adverse pressure gradient (pressure rise along the surface) caused by the suction side pressure recovery is typically after boundary layer transition and therefore the flow is more resistant to separations. In contrast, at low Re number regime, between 10^4 and 10^6, a laminar to turbulent transition occurs over a significant portion of the airfoil. The flow in the boundary layer is strongly influenced by the adverse pressure gradient, which makes the laminar boundary layer to separate from the curved airfoil surface. Figure 3.1 shows a schematic view of this process.

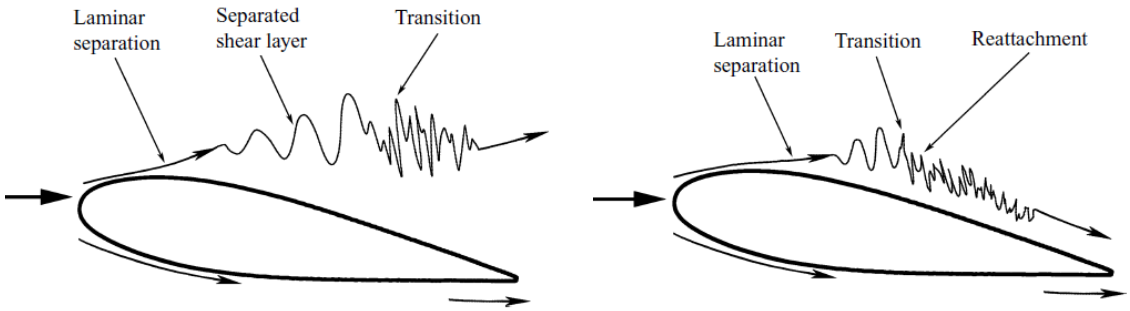

Figure 3.1: Flow over an airfoil at low Re number (images taken from Yarusevych *et al.* [8]): (a) Laminar separation without reattachment. (b) Separation bubble formation

If transition happens quickly enough after separation, the boundary layer will reattach onto the airfoil, forming a recirculating region of low pressure air called laminar separation bubble (LSB) [59, 14]. Figure 3.2 shows the structure of a LSB. Laminar separation bubbles may cause adverse effects, such as decreasing lift force, increasing drag force, reducing stability of the aircraft, vibration and noise. Characteristics of LSB must be understood well to design new airfoils which are not influenced by adverse effects of LSBs. In Figure 3.2 the structure of a LSB is examined in parallel with the pressure distribution along the suction side of the airfoil. The plateau observed in the pressure distribution illustrates the size of the LSB, where the start of the plateau indicates the laminar separation point and the sharp gradient at the end of the plateau is the turbulent

reattachment point.

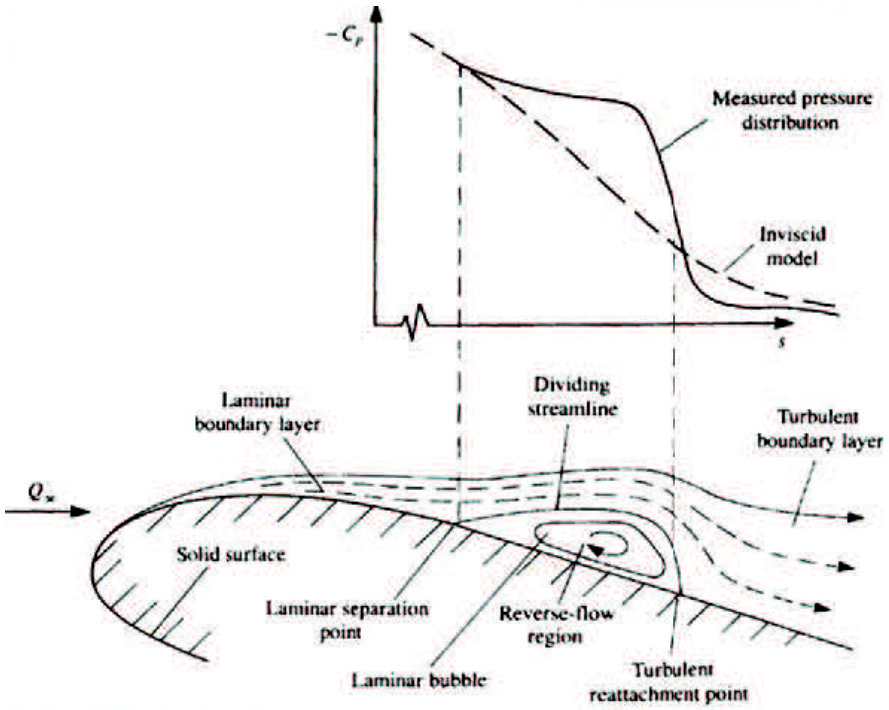

Figure 3.2: Structure of a laminar separation bubble on a curved airfoil surface and effects on pressure distribution (image taken from Katz and Plotkin [9])

3.1.1 Flow characteristics of laminar separation bubbles

The LSB is the governing flow feature when dealing with airfoils at low Re numbers. According to Carmichael [60], the characteristics of the flow over an airfoil can be divided depending on the Re number.

As shown in Table 3.1, airfoil performance is very dependent on Re number. The most important effect of Re number on airfoil performance is on the boundary layer. LSBs keep the flow attached to the airfoil by transferring momentum from free-stream to the boundary layer, but on the other hand, separation bubbles disrupts the flow over the airfoil causing additional drag. The balance between drag caused by the bubble and skin friction drag caused by the turbulent boundary layer is important [10]. From the data collected by Carmichael [60], it is possible to estimate a critical Re range around 50000 where airfoil BL behaves differently. When an airfoil is below its critical Re range, the flow is dominated by viscous forces. The lift generated is relatively low and a marked increase in drag coefficient can occur if laminar flow separates without reattachment. This type of flow is classified as *subcritical*. On the other hand, when an airfoil is above its critical Re range, there is a sudden increase in lift to drag ratio. In *supercritical* flows,

Table 3.1: Characteristics of the flow over an airfoil depending on the Re number.

Re number regime	Characteristics of the flow
[10000-30000]	Complete laminar flow exists over the airfoil in most situations. The lift coefficient is relatively low.
[30000-70000]	In this regime is when LSB first appears. For flow under Re=50000, the airfoil is not long enough for a separated laminar boundary layer to transition and reattach.
[70000-200000]	Airfoil performance significantly improves due to the elimination of LSB at low angles of attack. Boundary layer tripping can further improve the performance by promoting transition and decreasing the size of separation bubbles.
[200000-700000]	LSB appears in most flow situations. Boundary layer tripping losses its effectiveness.
[700000-3000000]	Effects of LSB are negligible. Upper bound of airfoils specifically designed for low Re environment.

the LSB reattaches the airfoil surface decreasing the width of the wake, what results in a lower drag.

In the extensive wind tunnel tests performed by Selig [61] between Re numbers of 60000 and 100000, it was found that the lift coefficient C_L increase less than the predicted slope of 2π from inviscid theory. Upon reaching a critical angle before stall, the slope of the C_L is closer to 2π. On the other hand, drag coefficient C_D increases rapidly at low angles of attack, and upon reaching the same critical angle, it drops significantly. This phenomenon is caused by laminar flow separation and reattachment (Figure 3.1). At low angles, the boundary layer separates without reattachment. This causes the slow increase in lift coefficient due to massive flow separation. The wake is also much wider compared to an attached flow, so more momentum loss is generated and the C_D is increased. In contrast, as the angle of attack is increased, the separated shear layer becomes more unsteady, and in certain situations it can transition and reattach into the surface, forming a LSB (Figure 3.2). This causes the wake to decrease, thus significantly increasing the aerodynamic efficiency. As a result, the lift-drag polar plots exhibit a *zig-zag* shape, compared to the *C* shape commonly seen in high Re airfoils. An example of such polar can be found in Figure 3.3.

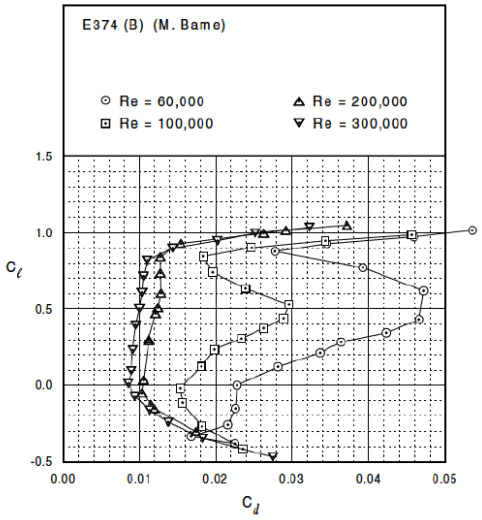

Figure 3.3: *Zig-zag* pattern observed in lift-drag polar at different low Re number (image taken from Li [10]).

Another common phenomena for rounded nosed airfoils at low Re number has been found to be the aerodynamic hysteresis [62]. It is an undesirable effect as it produces widely different values of lift for a given airfoil at a given angle of attack (AoA) and cannot be predicted by any computational method. The hysteresis loop formation is closely related to laminar boundary layer transition and separation on the airfoils and occurs near the airfoil stall angle. Figure 3.4(a) and 3.4(b) shows two possible flow states than can occur at the same angle of attack. For case A, a short laminar separation bubble exists on the upper surface near the leading edge. Downstream this point the flow is mostly attached producing a higher lift. For case B, the flow is in an stalled state, laminar flow extends to the point of separation and therefore lower lift is generated. As the angle of attack increases from an attached flow condition, the adverse pressure gradient can be strong enough to burst a short bubble (Flow state A) into a long one (Flow state B), producing a massive separation and deteriorating the airfoil performance. If the angle of attack is reduced after bursting, a short bubble will not be immediately recovered producing an hysteresis loop, as illustrated in Figure 3.4(c).

The separated but still laminar flow in the boundary layer over a curved airfoil is highly sensitive to external disturbances, such as surface roughness, free-stream turbulence and acoustic excitations, which can cause a premature transition to the turbulent state. Due to this, it is extremely difficult to provide well defined test conditions and to make accurate measurements on airfoils at Re numbers below 5×10^5. Moreover, the forces and pressures to acquire are very small, rising up the required resolution of the sensor. For all these reasons, the bandwidth of the experimental results at low Re number is quite large, compared to experiments at higher Re numbers. There are numerous

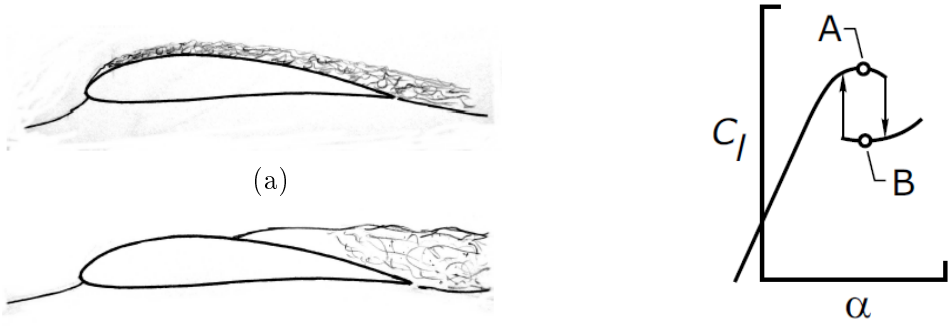

(a) (b) (c)

Figure 3.4: Hysteresis loop formation of an airfoil at low Re number (images taken from Selig [11]): (a) Flow state A. (b) Flow state B. (c) Hysteresis loop.

experimental databases of wind tunnel airfoil tests. One of the most relevant database is the book titled *Theory of wing sections* by Abbott [63], including a summary of airfoil data. However, this extensive database is only available for airfoils operating in fully turbulent conditions, and information on the performance of airfoils at low Re number is very limited in bibliography. Despite the significant effort made by Lissaman [14] and Selig and Guglielmo [61], low Re number airfoil design remains a non-rigorous process due to the lack of reliable experimental data.

3.1.2 Experimental metholodogy

In the last decade, several authors have measured two-dimensional airfoil characteristics to establish lift, drag and moment curves that serve as input data to performance calculations. One of the main contributions to the literature on this topic is the work done by Selig *et al.* at University of Illinois at Urbana-Champaign (UIUC) for over 200 airfoils at low Re numbers (40000 to 500000) [64].

Selig *et al.* describes in [52] the wind tunnel testing (WTT) methodology employed in their studies. The approach described in this paper uses a force balance to obtain lift and moment data and the wake rake method to obtain drag. Most of aerodynamic performance measurements rely on using a combination of a force balance and a pressure system. The main reason is the difficulty associated to measure the small forces experimented by the airfoil in drag direction. The main drawback of wake rake method is the considerable variation that exists in the wake along the spanwise direction. In order to obtain accurate measurements, Selig *et al.* [52] performed eight wake profile measurements at different spanwise locations and averaged that values together with the measurement over the center to obtain the drag at a given angle of attack. This leads to a relatively high time consuming task compared to the direct force balance method.

Another common experimental technique is the surface pressure measurement. For instance, Hansen *et al.* [65] incorporate pressure taps into the surfaces of two standard NACA airfoils of 21 % thickness-to-chord ratio. By this method, they were capable of reproducing the pressure distribution along the upper and lower surfaces of the investigated airfoils and identifying the existence of a separation bubble where the pressure gradient starts to decrease, reaching values closed to zero. In this context, the surface oil-flow visualization technique is very useful to further understand the flow phenomena in low Re airfoils. Oil film or dots on the model surface enable obtaining a picture of the flow pattern at the surface of the model placed in the wind tunnel quickly and easily [66]. The special mixture can be prepared from an appropriate oil and fine pigment (Al_2O_3; TiO_2, powder, fluorescent dye, coloring pigments, graphite). This technique has been applied by Selig *et al.* [52] to allow observation of the lines of separation and reattachment of the flow to the body. Several important flow features can be identified and related to the underlying skin friction and surface tension forces in the region of a laminar separation bubble. Ananda *et al.* [67, 12] performed surface oil-flow visualization tests at a number of angles of attack to find the laminar flow separation point and reattachment (Figure 3.5).

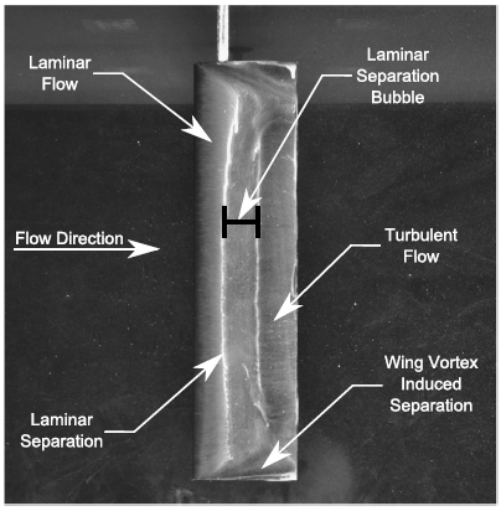

Figure 3.5: Surface oil-flow visualization of the major flow features on the Wortmann FX63-137 rectangular wing (image taken from Ananda *et al.* [12]).

With the increasing capabilities of the force transducers within the last decade, it is possible to find load cells with resolutions small enough to capture accurately these small forces in drag direction. One example is the piezoelectric force transducer type 9067 of Kistler company demonstrates that the resolution is even better than 0.01 N [13]. Another example is the strain gauge load cells manufactured by Interface that Ananda *et al.* [67] used for their custom-designed and in-house fabricated external three-component platform balance. This equipment was validated and used to acquire measurements of

ten wings at low Re number [12]. In addition, Timmer [68] also successfully recorded the forces and moments on a two-dimensional NACA0018 airfoil with a six component mechanical balance system in the Delft University LWST in Reynolds between 0.15 $\times$ 10^6 and 10^6.

3.1.2.1 Force and moment measurement systems

Measurement of steady and fluctuating forces acting on a body in a flow is one of the main tasks in wind tunnel tests (WTT). According to Tropea *et al.* [13], more than 70 % of the tests in a wind tunnel require some kind of force measurement. Historically the instruments were purely mechanical and their mechanism resembled balances for weighing; hence the use of the term *balance* today.

Wind tunnel balances are arranged to measure simultaneously the six different components of aerodynamic loads, three forces in the direction of the coordinate axes and the moments around these axes. These components are measured in a certain coordinate system, which can be either fixed to the model or to the wind tunnel, as shown in Figure 3.6. The wind axis system is aligned to the main flow direction, in which the drag force is defined. The lift force is generally defined as the force on the model acting vertically to the main flow direction. In contrast, the loads acting on the model are given by the balance and the pure aerodynamic loads must then be calculated from these components by using the correct yaw and pitch angles.

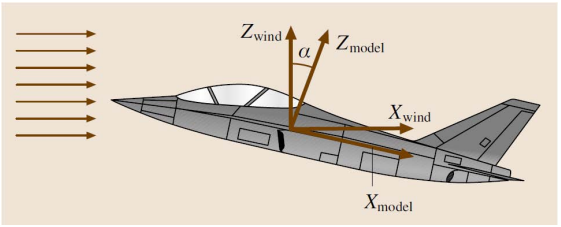

Figure 3.6: Various possible coordinate systems for a wind tunnel and model (Image taken from Tropea *et al.* [13])

The fundamental criterion of all multicomponent load measurements is that all the loads acting on a model must be separated into single components as best as possible. The interactions inside a balance and the deflections caused by temperature gradients are systematic errors that can be separated through calibration. The calibration process is the key point to achieve the required accuracy and reliability on the aerodynamic tests. In order to extract the loads from the balance signals, the following equation must be resolved:

$$F = \overline{E} \times S, \tag{3.1}$$

where F is the force vector, $\overline{E}$ is the evaluation matrix and S the signal vector. Through calibration one obtains an evaluation matrix whose elements take all the interactions and systematic errors into consideration. For a balance with no interactions, the six sensitivities for each component are the diagonal of the evaluation matrix while all other elements become zero.

Balance types are distinguished by the location at which they are placed. If they are placed inside the model they are referred to as *internal balances* and if they are located outside the model or the wind tunnel, they are referred to as *external balances*. External balances provide a higher flexibility as the model can be changed with almost no effort. Traditionally, external balances are designed to mechanically decouple the six aerodynamic loads into unidirectional traction-compression loads. Each unidirectional load is an output signal, and the composition of these signals provides the forces and moments acting on a body. Nowadays, several manufacturers produce commercial balances that provide the aerodynamic loads. The main inconvenient is that the recalibration requires a special facility that is very expensive.

In aerodynamic testing, strain gauge balances were usually applied for this task as, particularly in the past, the main focus was directed on the measurement of steady forces. In many applications, however, balances based on piezoelectric multicomponent force transducers are a recommended alternative solution. Contrary to conventional strain gauge balances, a piezo balance features high rigidity and low interference between the individual force components. High rigidity leads to very high natural frequencies of the balance itself, which is a prerequisite for applications in unsteady aerodynamics, particularly in aeroelasticity. On the other hand, only quasistatic measurements are possible, which is the main disadvantage of the piezo measuring technique. The decay of the charge and fault currents in the amplifier cause a zero-point drift. This effect is magnified when measuring small forces over long time periods. Nevertheless, the drift evolves linearly in time and simple corrections are possible.

3.1.2.2 Source of uncertainties

It is extremely difficult to provide well defined test conditions and to make accurate measurements on airfoils at Re number below 500000. Variations of lift and drag can occur due to wind tunnel setup deficiencies, non uniform model accuracy and local separation bubbles. Furthermore, the forces measured are smaller and the relative uncertainty in the measurement is higher.

The measurement of aerodynamic loads in a wind tunnel is a difficult task due to the required accuracy. In the field of aircraft aerodynamics, where the flow is attached and the interest is focused on drag measurements, a resolution of a drag count ($\Delta C_D = 0.0001$) is required [2]. In other tests where the flow is more or less separated, for example in bluff body flows, situations around stall or when the model is oscillating, a high-end drag measurement has less significance.

The inaccuracies in wind tunnel tests can come from different sources such as coupling and inertial effects. For example, inertial effects coming from the vibration of the model support system may introduce errors in the average result, if the acquisition frequency is not high enough. In addition, angle of attack errors as small as 0.01° can distort significantly the true test results [69].

Coupling effect

As the complete decoupling of the force components is very difficult, some coupling between lift and drag may appear. The balance mounting should ensure a good alignment between the balance axes and the wind or body axes where the forces need to be calculated. This effect is indispensable in airfoil testing, since only a one degree of angular deviation can cause an error of roughly 25 % [70]. In this context, the wind flow direction in the test section has to be determined since it may not coincide with the horizontal direction of the test section and the same error would be committed.

Inertia effects

When testing aerodynamic loads and moments in a wind tunnel, the measured values come from different sources. Together with aerodynamic forces, inertia forces can be expected caused by the oscillatory movements of the model. The model support needs to be very stiff to reduce the impact of inertia loads on the results. Another undesirable source of error is the electronic noise present in the data acquisition system (DAQ). The study and evaluation of these phenomena is important for the validity and accuracy of the measurements.

Gonzalez *et. al.* [70] found in their work that high sampling ratio benefits not only the reduction of the random noise originated in the DAQ system, but also the mean of the measured signal. High sampling rates of at least 2 orders of magnitude above the expected vibration frequency of the system reproduce accurate results. Moreover, a deeper spectral analysis permits the study of the frequency components of the signal and the inertia forces can be identified.

Apart from the inherent inaccuracies of force balance systems, it is typically assumed that the uncertainties in low Re airfoil experiments are mainly attributed to the sensitivity of laminar boundary layers to three external disturbances:

- Acoustic excitation
- Model deficiencies
- Free-stream turbulence level

Acoustic excitation

Acoustic disturbances of certain frequencies can also alter boundary layer behavior [71]. The low Reynolds number stall hysteresis loop (Section 3.1.1) is known very sensitive to the tunnel environment and acoustics. According to Saha [72], exposing the model to a noise of low frequency greatly reduces the hysteresis loop.

Model deficiencies

To achieve the required accuracy, it is essential that the model surface is clean or, in other words, *aerodynamically smooth*. According to the McGraw-Hill Dictionary of Scientific & Technical Terms [73], an *aerodynamically smooth* surface is the one that has irregularities sufficiently small to be entirely embedded in the laminar sublayer. Thus, the smoothness of a surface will depend on the roughness Reynolds number, expressed as:

$$Re_f = \frac{u_\tau z_0}{\nu}, \tag{3.2}$$

where u_τ is friction velocity, z_0 is aerodynamic roughness length, and ν is the kinematic viscosity of air. The critical Reynolds number is in the range of $2.5 \leq Re_f \leq 70$. Aerodynamically rough surfaces introduce errors when measuring the aerodynamic loads on streamlined bodies (such as airfoils) or highly curved bluff bodies as it alters the separation point of the boundary layer.

Level of surface smoothness of the model also alters the size of the stall hysteresis loop [72]. Roughness found on wind turbine blades due to manufacture and/or soiling during operation, is known to increase the thickness of the boundary layer causing earlier stall and higher drag for high Re number [74]. This generates a higher lift to drag ratio than rough airfoils at this Re range. However, at lower Re number, rough airfoils promote transition and decrease the size of separation bubbles. This results in a beneficial effect as the attached turbulent boundary layer improves the airfoil performance. Figure 3.7 shows the general trend of C_L/C_D of smooth and rough airfoils over the Re spectrum.

Traub [75] investigated the impact of surface finish on the behavior of a S8036 airfoil at Re numbers of 100000 and 150000. It was concluded that for this airfoil and test conditions, the measured loads showed little sensitivity to the airfoil's surface finish, as well as to the hysteresis loop. This is consistent with the trend shown in Figure 3.7, since

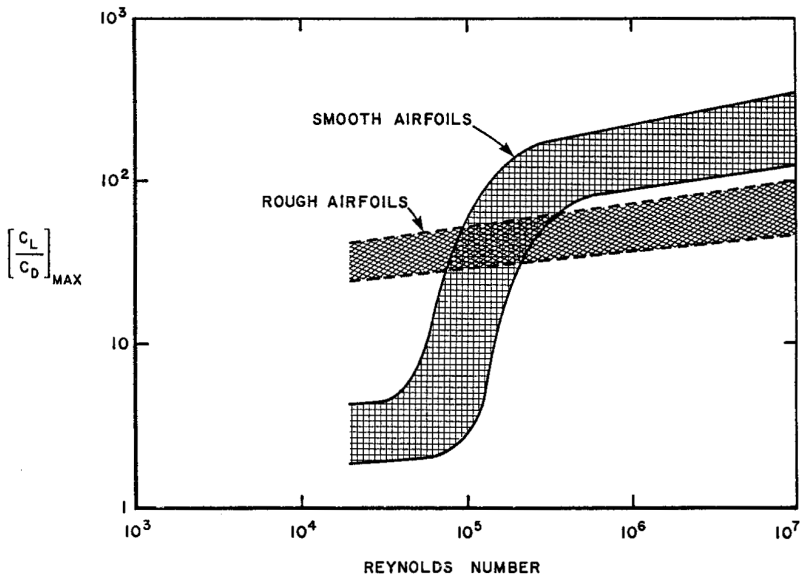

Figure 3.7: Maximum performance depending on Re number for smooth and rough airfoils (image taken from Lissaman [14]).

the aerodynamic performance in the Re range near 10^5 is similar for smooth and rough airfoils.

Non uniform model accuracy have historically been another major experimental uncertainty. Mueller and Batill [71] observed an asymmetric behavior for a symmetric airfoil because of manufacturing defects. Leading edge radius closure can lead to slope discontinuities in the intersection of the upper and lower airfoil surface. This discontinuity can result in the formation of leading edge separation bubbles that produce inconsistent maximum lift values [74]. Although these effects becoming negligible with modern computer numeric control (CNC) manufacturing techniques, special care needs to be taken in the manufacturing process of the airfoil.

Free-stream turbulence level

For most experiments, the dominant environmental factor is free-stream turbulence (FST) level [10]. Low turbulence levels within the LSWT test section are necessary to ensure that laminar flow does not prematurely transition to turbulent flow. According to Gilling [76], inflow turbulence increases the transport of momentum from free flow to the inner region of the boundary layer. This increases the resistance against adverse pressure gradients, so the boundary layer separation point advances along the leeward surface of the airfoil and thereby reduces separation at high incidences corresponding to airfoil stall [54]. As a result, the linear range of the lift curve is extended and the maximum lift is increased, as observed in the experiments performed by Hoffmann [77].

Another important characteristic of turbulence is the dominant size of the turbulence

length scale. The airfoil boundary layer is sensitive to turbulent fluctuations on the order of the size of the boundary layer thickness. If turbulence containing this characteristic length scale is added to the free-stream, the separated boundary layer transitions to a turbulent boundary layer more quickly and therefore reattaches earlier. The length of the separation bubble is reduced causing a smaller hysteresis loop. Hoffmann [77] investigated the effect of FST on lift and drag coefficients of a NACA0015 airfoil. It was found that for an intensity greater than 3 %, hysteresis loop was eliminated, while below this threshold the loop grew in size as turbulence intensity dropped down. Higher levels of turbulence can cause the boundary layer to transition to turbulence before separation and therefore eliminate the separation bubble altogether. The effect FST on airfoils is analyzed separately in chapter 4.

For all these reasons, the drag polars obtained at low Re are less repeatable than data obtained at higher Re, and differences in measured aerodynamic forces are observed when matching flow parameters in different facilities. This is evidenced in the data collected by McArthur [78], where drag polars of the Eppler 387 airfoil obtained in different facilities showed a relatively high disagreement. It is also stated that different measurement techniques employed in each facility could return different results, what makes difficult to estimate what factor is responsible for the disagreement. However, the bandwidth of the results at low Re number is not necessarily a sign of poor measurement techniques, it is a matter of the physics of the flow.

3.1.2.3 2D wind tunnel testing of airfoils

Since National Advisory Committee on Aeronautics (NACA) recognized the need to isolate the wing tip effects in 1939, 2D wind tunnel testing (WTT) has been a standard procedure. 2D WTT aims to mitigate the formation of wing tip vortices (3D effects) by installing plates at the end of the wing [79]. This end plate is a solid boundary much greater than the chord of the airfoil that inhibits the pressure gradient across the surfaces of the wings and eliminates the wing tip vortices. Thus, the incoming fluid experiences a 2D flow and a effectively infinite wing [80].

In any experiment which involves measurement of force, a small gap should exist between the airfoil and the wind tunnel wall or end plates to isolate the model from the end plates so that only the forces acting on the model are measured [72]. Any physical contact between the model and the end plate may degrade the reliability of the measurement, since it would be extremely difficult to remove the end-plate drag from the measurement [2].

While many WTT use end plates with a force balance arrangement, little information in literature analyze the errors resulting from the gap that exist between the model and

the end plate [81, 72]. No particular standard exists to size the gap, except for the criteria established by Barlow *et al.* [2] that a distance of 0.5 % the span of the airfoil would generate negligible effects on lift and drag polars. In order to determine the maximum gap at which the flow can still be considered two-dimensional and tip effects can be neglected, Vaidyanathan *et al.* [80] defined the non-dimensional distance, λ, as the ratio of gap distance, d, to laminar boundary layer thickness, $\delta_{t,laminar}$, over the end plate. In this study several force balance measurements were performed on a NACA0012 wing section for a number of angles of attack (AoA) and λ values at operating Re number of 50000 and 100000. They determined that the critical non-dimensional gap distance is $\lambda_{critical} = 1$ for the given airfoil, so the gap distance should not exceed the laminar boundary layer thickness over the end plate.

Figure 3.8 shows the experimental setup used when a force balance is arranged in wind tunnel airfoil tests at University of Notre Dame. Small gaps between the model and end plates are kept small enough to ensure the two-dimensionality of the flow. Based on the findings of the investigation by Boutilier *et al.* [79] for low Re airfoil experiments, it is recommended that the end plates should be installed outside the wind tunnel wall boundary layer with a spacing of $b/d \geq 7$, where b is the spanwise distance between end plates and d is the model height projected onto a streamwise normal plane.

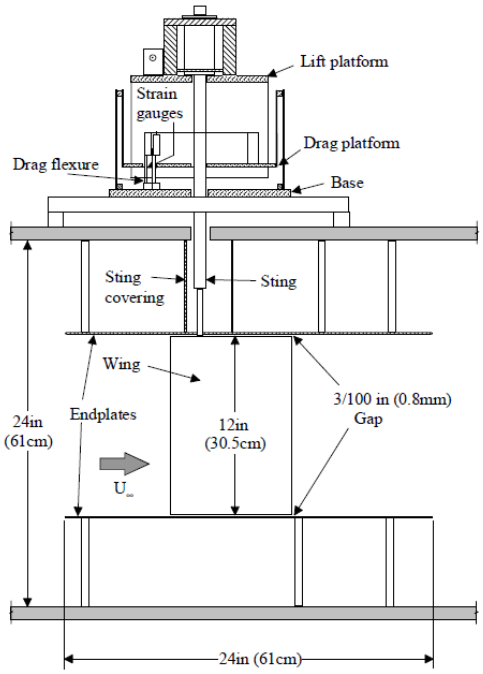

Figure 3.8: Force balance arrangement in the test section at University of Notre Dame, Indiana (image taken from Pelletier and Mueller [15]).

3.1.2.4 Wind tunnel corrections

Compared to the free-stream flow in the unlimited space, the wind tunnel has finite dimensions. Its cross section and its usable length are limited, the static pressure along its axis is not constant and the proximity of the airstream boundaries to the test object modifies the flow around it. The angularity of the flow, the distribution of velocity, the pressure around the model and the shear stresses on its surface are modified, and consequently, the forces and moments acting on the body. To cope with systematic errors resulting from these effects, the standard practice is to perform *corrections* after the measurement. Different expressions are used to account for LSWT corrections, depending on the body shape (bluff or streamlined body) and the test section type (open or closed). For an airfoil placed in a closed test section the following perturbations are present:

Solid blockage

In wind tunnel tests, the ratio of the frontal area of an object to the stream cross-sectional area, known as *blockage ratio*, reflects the relative size of the test item to the test section. It is usually chosen in the range of 0.01-0.1 with 0.05 being typical. In the case of a closed test section, the surface stresses are larger than for the corresponding free-air condition, as the tunnel walls confine the flow around the model reducing the effective area and hence, the incoming flow speed or dynamic pressure is increased. Solid blockage is a function of the model size and test section dimensions [52].

$$\epsilon_{sb} = \frac{K_1 M_v}{A_{ts}^{3/2}}, \tag{3.3}$$

where K_1 equals 0.74 for a wing spanning the tunnel breadth and 0.52 for one spanning the tunnel height [2], M_v is the model volume and A_{ts} is the test section area. If greater accuracy is required, the boundary layer displacement thickness around the perimeter can be subtracted to the geometric area.

Wake blockage

In a closed test section, wake blockage increases the measured drag. This effect is a result of the finite size of a body wake and it is caused by the fact that the airstream is not free to expand like in an infinite stream. In this sense, it is somewhat similar to solid blockage, with the difference that it is function of the body shape and the measured drag force on the model.

$$\epsilon_{wb} = \left(\frac{c}{2h_{ts}}\right) C_{D_u}, \tag{3.4}$$

where c is the chord, h_{ts} is the wind tunnel height and C_{D_u} is the measured drag.

Streamline curvature

This refers to the alteration of the curvature of the streamlines of the flow about a body in a wind tunnel compared to the curvature of the streamline in a infinite stream. Due to the effect of finite distances to boundaries, the airfoil effective camber is increased as the streamlines are squeezed together. For an airfoil in a closed wind tunnel, the lift coefficients, the pitching moment about the quarter-chord point and the angle of attack are increased.

Horizontal buoyancy

This refers to the variation of the static pressure along the test section when no model is present. The axial pressure gradient dp/dx produces a drag force analogous to the hydrostatic force on objects in a stationary fluid in a uniform gravitational field. It is assumed that the axial force pressure gradient with a model in the test section is the same as that in the empty tunnel.

3.2 Experimental setup

A good experimental setup is of great importance to produce accurate measurements at low Re numbers. The standard procedure for WTT of airfoil is to install plates at the ends of the wing section to mitigate the tip vortices. This way, the airfoil is assumed to experience a 2D flow. In the current approach, a force balance technique is employed to measure the aerodynamic data. Figure 3.9 shows a sketch of the experimental setup.

The airfoil has a chord length of c= 150 mm and is placed in the middle of the test section with two splitter plates at the top and bottom ends. The leading edge of the end plates have a streamlined shape to reduce the separation effect [82]. The end plates are assembled to the wind tunnel structure at a distance of 50 mm from the floor and top wall. This distance is enough to keep the airfoil outside the boundary layer of the LSWT [79] (Section 2.3.4). Moreover, the spanwise length of s=900 mm results in an aspect ratio of the wing of AR=s/c=6 that minimizes the effect of cross flows caused by the end plates.

The airfoil is mounted on a sting at 0.3c=45 mm from the leading edge. The wing is then assembled into a shaft support and screwed to the dynamometer, which is fixed to the rotary table to allow the rotation of the model. This way, the aerodynamic forces acting on the model are mechanically transferred to the force balance. To measure only the forces acting on the model, small gaps exist to isolate the airfoil from the wind tunnel floor and from the end plates.

The gap between the end plates and the airfoil is set to 2 mm. According to Barlow

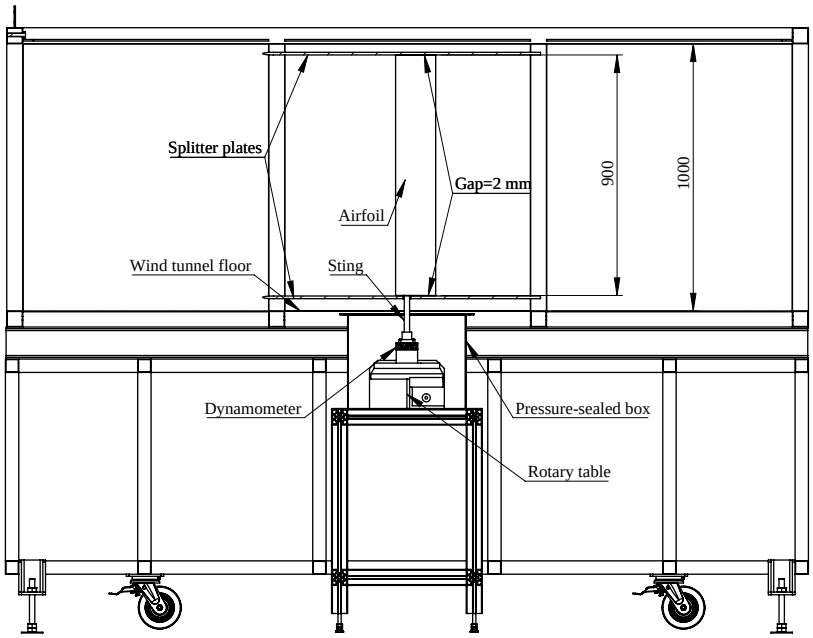

Figure 3.9: Experimental setup

et al. [2], a distance of 0.5 % the spanwise length of the wing produces negligible effects on lift and drag measurements. With the current configuration this would result in a limiting gap size of 4.5 mm, so the gap size employed in under the admissible limit. Other authors such as Vaidyanathan *et al.* [80] state that the gap distance should not exceed the laminar boundary layer thickness over the end plate. The laminar boundary layer width can be approximated by *Blasius* solution [58]. For 10 m/s of flow velocity, a laminar boundary layer of 4.3 mm is expected at the location where the airfoil is placed, so the gap adopted in the experimental setup meets also this requirement.

To diminish the effect of the gap on the wind tunnel floor, the rotary table is located inside a pressure-sealed box. A sealing joint between the wind tunnel floor and the box maintains the same pressure in the test section and in the box. Thus, the flow is prevented from blowing into the test section through this gap due to the pressure difference with the room. In addition, a sting covering is mounted between the low end plate and the floor to isolate the sting from the airfoil force measurement.

Figure 3.10(a) shows an image of the real configuration arranged at the LSWT where the NACA0021 airfoil is installed inside the test section. To validate the experimental setup, a surface oil-flow visualization is performed. A special mixture of oleic acid and TiO_2 powder is impregnated over the airfoil surface for flow visualization. As shown in Figure 3.10(b), this technique permits to visualize the flow pattern at the surface of the model placed in the wind tunnel. The characteristic flow regions of low Re airfoils

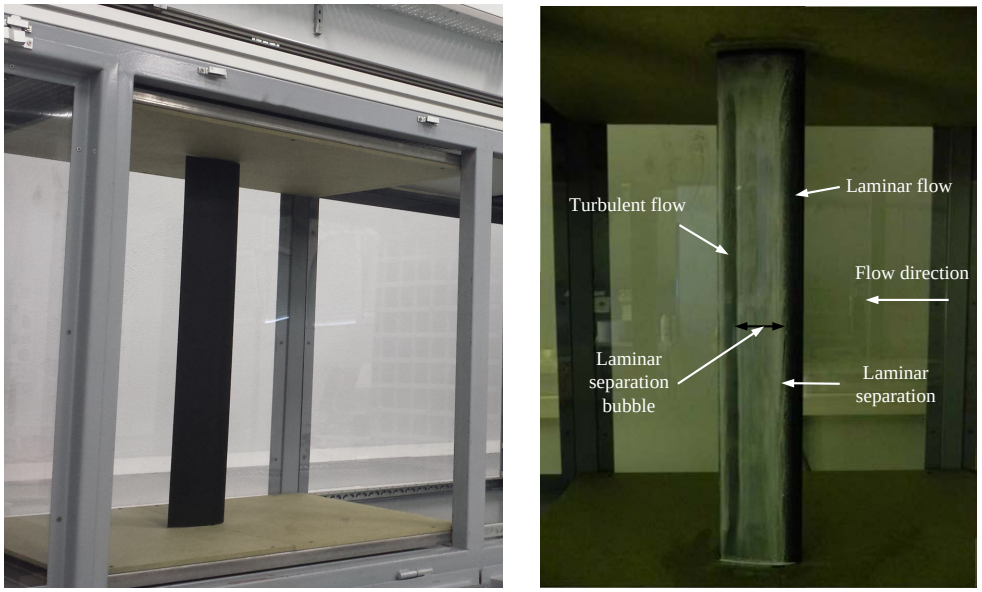

(a) (b)

Figure 3.10: Experimental setup arranged at MU. (a) NACA0021 airfoil installed inside the test section (b) Surface oil-flow visualization

can be can be detected, namely the laminar and turbulent flow regions, the laminar separation point and the size of the laminar separation bubble. The regions are uniform and constant in the spanwise direction and no wing vortex induced separation is observed at the model ends. By this observations, it can be said that the end plate configuration arranged ensures a good two-dimensionality of the flow.

3.2.1 Instrumentation and data acquisition system

In order to measure the forces acting on the body of interest, a six-component force balance with reference Minidyn 9256C1 from KISTLER company is equipped behind the test section floor. The force balance is composed of four 3-component piezoelectric transducers equally spaced that allows the calculation of reaction forces and moments.

These force transducers are extremely sensitive (26 pC/N). The dynamic threshold of the force balance is about 2 mN. However, the maximum achievable resolution of the measuring chain is often given by the charge amplifier, the N/V scale employed and the resolution of the acquisition system. The error in the measuring chain is below 2 % of the full scale output (FSO) and includes sensor linearity, hysteresis, repeatability and charge amplifier error and linearity. The minimum scale that can be adjusted in the charge amplifier 5070A that is used is 1 N/V for a measuring range of ± 10 N. This means that the minimum force that can be measured with confidence is 0.2 N, which is considered to be small enough for measurements of drag force in airfoils at low Re number.

However, the 5070A charge amplifier has an inherent electrical drift about ± 0.03 pC/s, what can induced to significant error specially if long tests are taken in the low measuring range. Since the zero point drift varies linearly in time, it can be easily corrected by measuring the voltage at the beginning and at the end of the test when the fan of the wind tunnel is not blowing. Then, the time of each measurement is recorded together with the output voltages and a simple linear correction is applied to the saved data.

The six signals coming from the amplifier are recorded by a NI9201 acquisition card together with a NI cDAQ-9174 chassis which is connected via USB to the PC. A NI ISM 7400 series Nema 23 stepper motor drives the rotary table that allows to rotate the model at different angles of incidence. This rotation is the fourth axis of the motion control system, which is developed via LabView environment. The embedded NI cRIO-9031 controller together with the 4-axis SISU 1004 interface module is responsible for controlling at real-time the stepper motors.

As for the case of traverse system, a graphical interface allows to communicate the motion control while the results are monitored. A LabView code is developed to automate the recording of the measured forces with the scanning of different incidence angles.

3.2.2 Airfoil model accuracy

The sensitivity of laminar boundary layers to external disturbances can increase significantly the bandwidth of the results. One of these disturbances is the model deficiencies that arise from the manufacturing process.

The airfoil used in the force measurements is designed using a computer-aided design (CAD) package and manufactured using a computerized numerical control (CNC) machining center. The material of the airfoil is Polyoxymethylene (POM), also known as polyacetal. This material is an engineering thermoplastic used in precision parts requiring excellent dimensional stability. It has high stiffness and low density, which is desirable to minimize the inertia forces caused by the flow induced vibrations on the model.

A high quality surface finish must be achieved to ensure that the airfoil is *aerodynamically smooth* and has irregularities sufficiently small to be entirely embedded in the laminar sublayer. The smoothness of a surface will depend on the roughness Reynolds number defined in Equation (3.2). To evaluate this equation, the skin friction is estimated using the Schlichting skin-friction correlation [58]

$$C_f = 0.02666 Re^{-0.139}. \tag{3.5}$$

This correlation takes into account that the flow is laminar for the first part of the plate and provides some corrective factors using Blasius's equations. With the skin friction coefficient the wall shear stress is computed as $\tau_w = C_f \frac{1}{2}\rho U$ and the friction velocity can be obtained by $u_\tau = \sqrt{\frac{\tau_w}{\rho}}$. Once the friction velocity is determined, the aerodynamic roughness length z_0 can be defined by Equation (3.2). Considering a free stream velocity of 10 m/s and the roughness Re number to be below one, so that viscous effects are dominant the aerodynamic roughness length is found to be $z_0 \approx 35$ μm. This value represents the maximum height of the irregularities that are acceptable to consider a surface finish as *aerodynamically smooth*. As a verification, the y^+ value can be calculated as $y^+ = \frac{\rho u_\tau y}{\mu}$ introducing the z_0 value as the distance y from the wall. This leads to a value of $y^+ \approx 1$, which is inside the laminar sublayer.

The roughness on the airfoil is measured using the surface-finish testing instrument SJ-310 from Mitutoyo company. This device has a contact surface detector capable of determining the small irregularities present along the length of study. The apparatus outputs the arithmetic average deviation R_a, the average maximum height R_z and the maximum height R_t of the profile for the length of the surface analyzed. The length of the measurements is taken following the standards given in ISO 4287-1997 norm at different locations of the airfoil, near the leading and trailing edges and also at medium chordwise lengths. Table 3.2 summarizes the average of these measurements for the orientations tested. As can be observed, the roughness is quite below the maximum admissible roughness.

Table 3.2: Averaged roughness parameters for the airfoil manufactured

Orientation	R_a	R_z	R_t
Chordwise	1.4±0.1	7.4±0.5	9.9±1.0
Spanwise	0.7±0.2	4.4±1.0	6.5±2.0

Non uniform model accuracy is historically another major experimental uncertainty. Leading edge radius closure can lead to slope discontinuities in the intersection of the upper and lower airfoil surface. In order to determine the accuracy of the model it is tested using an absolute measuring arm 7320SI with a fully integrated and certified RS3 laser scanner from ROMER company. This metrology system is used to obtain a point cloud of about 35000 points for a 100 mm of airfoil span. The reverse engineering toolbox in the CAD package has enabled to obtain a cut section at the midplane of the airfoil to compare against the original airfoil design. Figure 3.11 shows both profiles in detail.

At a first view, the manufactured airfoil seems to be free from large imperfections, as both edges can be hardly distinguished. However, as it is observed in the leading edge detail, a slight slope discontinuity exists in the upper edge, while the lower edge coincides

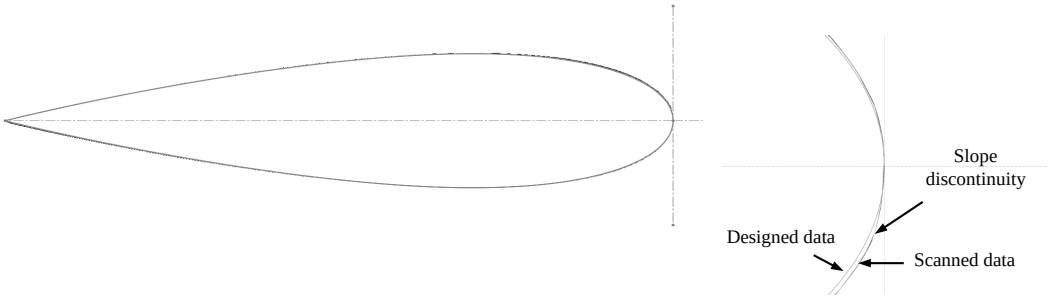

(a) (b)

Figure 3.11: Comparison between designed and scanned airfoil edges (a) General overview (b) Leading edge detail

with the designed profile with reasonable accuracy. Although this manufacturing defect is little, it may produce an asymmetric behavior of the performance data for a symmetric airfoil [71].

3.2.3 Balance alignment

As noted in section , it is of great relevance to correctly align the airfoil with the incoming flow, in order to minimize the coupling effect between lift and drag. With this purpose, a specific assembly fixture is designed to make the axis of the airfoil and the dynamometric balance coincident. Figure 3.12 shows a sketch of the holding system. The airfoil and the shaft support are transparent to clearly show the keys equipped in the sting.

The airfoil has a hole with a key groove precisely machined at the bottom surface oriented with respect to the chordline of the airfoil. The sting fits in with this hole by means of a key located at its upper end. In the lower end of the sting, another key which is machined to be coincident with the upper key is assembled to the flanged shaft support with keyway. Thanks to the tight tolerance of the keyways and the shaft diameter, it is ensured that no misalignment error is occurred during the mounting of the different components. To correctly position the shaft support with respect to the force balance, a dial indicator is used to render both elements parallel. The alignment surfaces of the shaft support is machined to the same standard as the surface of the force balance. Therefore, the axes of the force balance and the model are assumed to be coincident. The rotary table has a worm wheel mechanism drived by a stepper motor with a resolution of 25000 steps/rev, what results in a minimum angle of 0.01°. This resolution is considered to be small enough for airfoil WTTs [69] .

In order to orient the whole system with the incoming flow, several force measure-

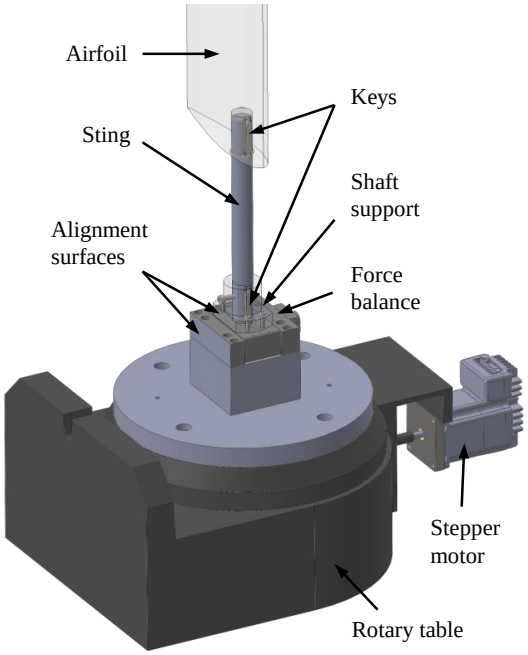

Figure 3.12: Designed holding system for the airfoil

ments are taken at different incidence angles ranging from $-8°$ to $8°$. The acquisition rate is 500 Hz, which is considered to be high enough to overcome errors due to inertia forces [70] and low enough to be far from the force balance resonance frequency, what would induce some errors in the measurements. A total of 7500 samples are recorded together with the time of each signal to perform the drift correction at the post processing stage.

Since the NACA0021 airfoil is symmetric, the lift at zero incidence angle is zero. When plotting the lift force against the angle of attack (AoA), if some alignment error exists the lift curve crosses the zero abscissa for a certain angle that can be attributed as the error committed. The procedure proposed is to make several scannings to continuously correct the error in the angle positioning until a satisfactory position is reached. It should be noted here that this procedure is valid if a the airfoil model is free from imperfections.

Figure 3.13(a) shows the different scannings performed. The first scanning R1 shows that an error of $1.28°$ is committed. This error needs to be corrected since the lift curve is not symmetric and it can lead to an incorrect estimation of the stall angle, as it is observed in the sudden drop at $-7°$. In the second scanning, R2, the angle obtained in R1 is introduced as zero angle prior to the experiment. This way the lift curve represents a more symmetric curve and it crosses the C_L quite near zero. A third measurement R3 is performed for further improvement of the positioning. The resolution near the zero angle of attack for R3 is increased to better determine the error committed. Figure 3.13(b) shows a detailed view of the R2 and R3 tests. In R2 still exists a little deviation

of $-0.03°$, which is corrected for case R3. A final error of $0.01°$ is achieved, the best alignment possible given the resolution of the stepper motor. This zero angle reference is used for all the tests performed in Section 3.3.

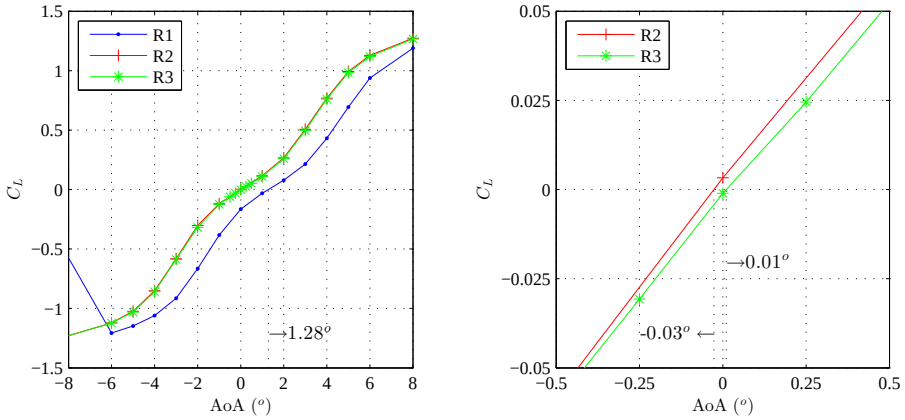

(a) (b)

Figure 3.13: Lift curve during the balance alignment process (a) R1,R2 and R3 scannings (b) Detail of R2 and R3 scanning

3.3 Performance data measurements

The experiments are conducted at a Re number of 10^5 with a relatively broad angle of attack (AoA) range, from $-4°$ to $40°$. The AoA is changed by rotating the model to the desired position with the rotary table while the wind is blowing. The measurement of the aerodynamic forces at the corresponding AoA is recorded as a separate measurement, leaving sufficient time to let the forces settle down after the rotation. As the airfoil rotates in conjunction with the dynamometer, the F_x and F_y forces are measured in the coordinate frame of the force balance. Then, a decomposition from the model axes into the wind axes is required at the post-processing stage. The AoA angle is established positive in the clockwise direction to make it coincident with the coordinate frame of the dynamometer.

The aerodynamic forces D and L can be obtained as follows:

$$\begin{Bmatrix} D \\ L \end{Bmatrix} = \begin{bmatrix} \cos(\text{AoA}) & -\sin(\text{AoA}) \\ \sin(\text{AoA}) & \cos(\text{AoA}) \end{bmatrix} \begin{Bmatrix} F_x \\ F_y \end{Bmatrix} \tag{3.6}$$

The temperature T and atmospheric pressure P_{atm} is also recorded during test. With this information, the air density ρ is calculated from the ideal gas law as P_{atm}/RT.

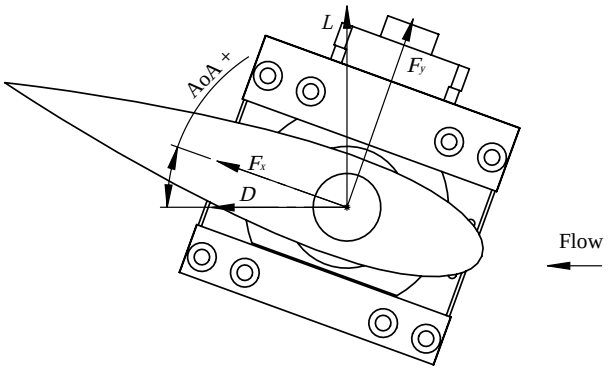

Figure 3.14: Decomposition from model axes into wind axes

3.3.1 Uncertainty analysis

Prior to the experimental tests, an uncertainty analysis is performed to asses the accuracy of the measurements. Figure 3.15 displays the error committed by the force balance approach. Up to three repetitions are performed independently for each angle position. The error committed is expressed by the standard deviation of the force measured as $\Delta F = \left(\frac{1}{N}\sum_{i=1}^{N}(F_i - F_{mean})^2\right)^{\frac{1}{2}}$, being N the number of repetitions. This value is then normalized to obtain the error in the drag ΔC_D and lift ΔC_L coefficients.

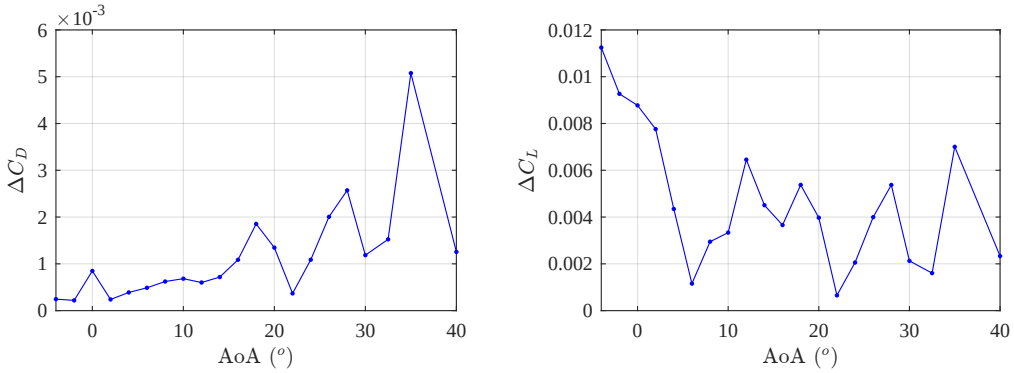

(a) (b)

Figure 3.15: Error committed by the force balance approach (a) ΔC_D coefficient error (b) ΔC_L coefficient error

The error committed in drag coefficient estimation is under $\Delta C_D < 0.001$ for low angles of attack. At higher angles the error can increase up to $\Delta C_D = 0.005$. The reproducibility of the results in the drag direction is acceptable, taking into account the small forces that are measured. In lift direction the error committed is higher owing to the less sensitivity of the dynamometer in y direction compared to the sensitivity in x direction. At negative angles the error $\Delta C_L = 0.011$ is maximum and then diminishes for higher angles of attack down to $\Delta C_L < 0.007$.

3.3.2 Wind tunnel corrections

The aerodynamic coefficients are obtained from the measured aerodynamic forces, drag D and lift L, as follows;

$$C_{D_u} = \frac{D}{1/2\rho s c V_m^2}, \tag{3.7}$$

and

$$C_{L_u} = \frac{L}{1/2\rho s c V_m^2}, \tag{3.8}$$

where s is the span of the airfoil and c is the chord line and the subscript $_u$ denotes that the value is uncorrected.

The presence of wind tunnel walls increases the measured aerodynamic coefficients because of the increase in velocity at the model V_m. The two-dimensional flow is affected by the lateral boundaries and four different phenomena occur; solid blockage ϵ_{sb}, wake blockage ϵ_{wb}, buoyancy and streamline curvature (Section 3.2.3). The measured quantities that must be corrected can be subdivided as stream and model quantities.

According to Selig *et al.*[52], the most important stream quantity is the velocity at the model. This velocity can be obtained from the free stream velocity measurement by applying the proper corrections to account for solid and wake blockage, as well as for the buoyancy due to the boundary layer growth. The velocity correction is expressed as

$$V_m = V_u K(1 + \epsilon_{sb} + \epsilon_{wb}). \tag{3.9}$$

The K factor considers an additional velocity correction that is required to correct the boundary layer growth when splitter plates are used. It can be obtained by a calibration process with the model out of the test section by measuring the velocity upstream (but inside the splitter plates) and the velocity at the model. This way, a calibration curve is reproduced that relates the increase in velocity from the upstream position to the model location as function of the free stream velocity as

$$V_m = K V_u, \tag{3.10}$$

where K is a function of V_u. Other free stream quantities such as the Re number and dynamic pressure can be obtained from the corrected value of velocity.

The model quantities are corrected to account for solid and wake blockage using the expressions given by Selig [52]. These correction equations for lift, drag, moment and angle of attack are expressed as

$$C_D = C_{D_u} \frac{1-\epsilon_{sb}}{(1-\epsilon_b)^2}, \tag{3.11}$$

$$C_L = C_{L_u} \frac{1-\sigma}{(1-\epsilon_b)^2}, \tag{3.12}$$

$$C_M = \frac{C_{M_u} + C_{L_u}\sigma(1-\sigma)/4}{(1-\epsilon_b)^2}, \tag{3.13}$$

and

$$\alpha = \alpha_u + \frac{57.3\sigma}{2\pi}(C_{L_u} + 4C_{M,c/4_u}), \tag{3.14}$$

where $\epsilon_b = \epsilon_{sb} + \epsilon_{wb}$ and $\sigma = \frac{\pi}{48}(\frac{c}{h_{ts}})^2$. For a model mounted horizontally h_{ts} is the test section height. However, with the current configuration the airfoil is mounted vertically so the width of the wind tunnel is considered here. $C_{M,c/4}$ is the pitching moment coefficient about quarter chord of the airfoil.

Figure 3.16 shows the comparison between corrected and uncorrected aerodynamic coefficients for the AoA range studied. It can be observed how the correction takes relevance as the AoA is increased, due to the higher blockage ratio.

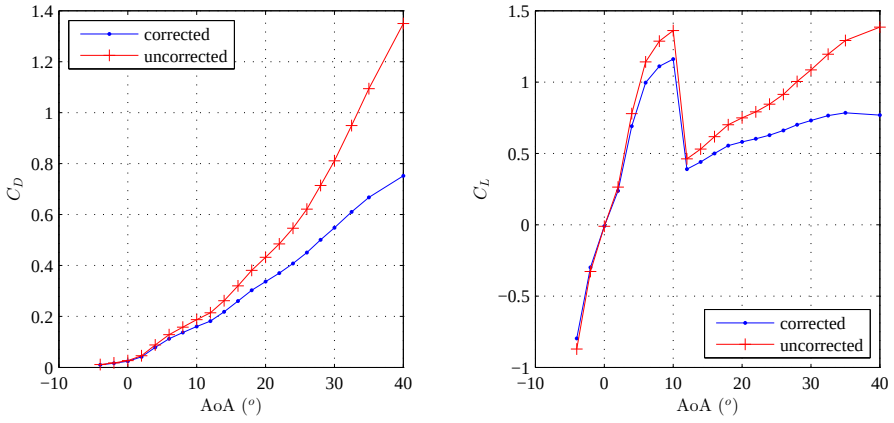

(a) (b)

Figure 3.16: Corrected vs uncorrected aerodynamic coefficients (a) C_D (b) C_L

3.3.3 Comparison with similar tests

Due to the limited performance data of airfoils operating at low Re numbers in bibliography, it is hard to find exactly the same airfoil operating at the same low Re number. However, two experiments are found with very similar characteristics.

One experiment is the work done by Timmer [68] at Delft University, which is a reference facility in the wind energy field. The turbulence intensity is extremely low,

0.02 % at a Re number of 0.15×10^6. Although the measurements were performed for a different airfoil NACA0018, it may serve as a qualitative comparison. The forces on the model were recorded with a six component mechanical balance system. The 0.25 m chord numerically milled steel model is placed horizontally in the tunnel, completely spanning the 1.80 m width of the test section, but leaving a gap at both ends smaller than 0.5 mm.

The other experiment is the work done by Hansen *et al.* [65] at the wind tunnel of the university of Adelaide. A Re number of 120000 is investigated on a NACA0021 airfoil. The airfoil is fabricated in aluminium using a CNC milling machine. A high quality surface finish was achieved on the models and the trailing edges were free of imperfections. The wind tunnel has a cross-sectional dimensions of 500 mm by 500 mm and the Re number is 120000 based on the free stream velocity of 25 m/s and the chord length of the airfoil. A gap size of 3 mm is chosen between the wing tips and working section ceiling to minimize three dimensional effects. Lift and drag measurements are obtained using the six component load cell from JR3 company which is accurate to 0.25 %.

Table 3.3 summarizes the main characteristics of each experiment for clarity. It is noteworthy here that all the experiments use the a force balance approach to measure drag and lift data.

Table 3.3: Wind Tunnel data

Test	Airfoil	Re	Wind Tunnel
Torrano2016	NACA0021	100000	Mondragon Unibertsitatea
Timmer2008 [68]	NACA0018	150000	Delft University
Hansen2014 [65]	NACA0021	120000	University of Adelaide

Figure 3.17 shows a comparison between the drag and lift curves obtained on each test.

According to the coordinate frame defined in Figure 3.14, the lift curve for the data obtained at MU is negative. The sign of this curve is reversed for better comparison with the rest of the tests. It can be observed that the lift curve has similar trends taking into account that the Re number is not exactly the same. In the three experiments it is evident the effect of a laminar separation bubble as the lift curve slope is different from the ideal lift slope (2π rad^{-1}). The ideal lift slope is plotted as black continuous line to ease the comparison. The laminar separation bubble effect on the lift curve obtained at MU is more pronounced compared to the other experiments, rising the $C_{L_{max}}$ value. To some extent, this can be explained as a consequence of the Re number effect. The effect

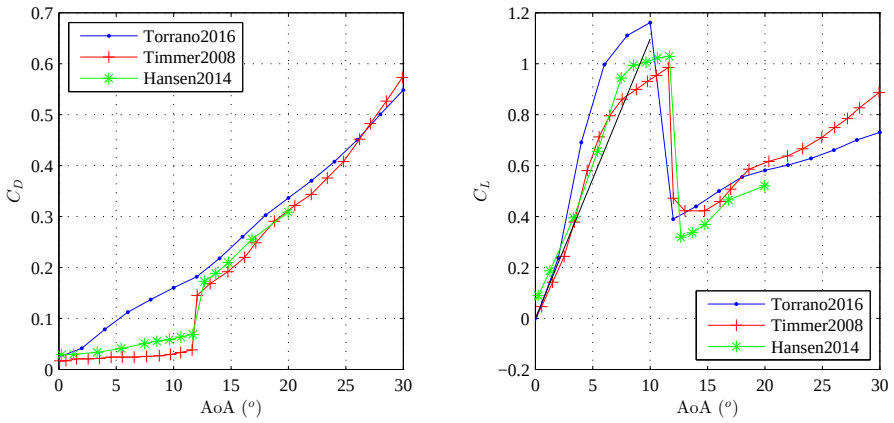

(a) (b)

Figure 3.17: Comparison with similar tests (a) C_D coefficient (b) C_L coefficient

laminar separation bubbles takes more relevance when Re number is decreased. The stall angle is around 12° for the other two experiments, while in the current experiment is around 11.25°. All the lift curves experience a sudden stall characteristics to C_L values around 0.4 and then the lift curves increase with the AoA.

The drag curves behave similarly at the post-stall situation where the flow is separated. However, the drag curves obtained at pre-stall in the current investigation are higher compared to the other tests and the sudden rise of the C_D curve observed at stall is nonexistent. This inconsistency can be due to several reasons.

A possible cause may be that the force balance is not able to measure such small forces in drag direction with accuracy. In order to discard this source of error, the profile drag is also measured by the momentum deficit method (Figure 3.18(a)). This drag force estimation consists in doing several velocity measurements with the cobra probe in the wake of the airfoil along different locations. After application of the two-dimensional momentum and continuity equations to a control volume that covers initial upstream and final downstream conditions of the airfoil, the drag force per unit span can be calculated from:

$$d = \rho \int_{\infty}^{\infty} u_1(U_\infty - u_1)dy. \tag{3.15}$$

It is assumed that the location of the measurements is far enough behind the airfoil so that the static pressure has returned to the upstream tunnel static pressure. To ensure this condition the cobra probe is located at 500 mm (more than 3 chord lengths) downstream of the trailing edge of the airfoil. Up to 5 separate tests are done for $AoA = 0°$, $5°$, $10°$, $15°$ and $20°$. The cobra probe is traversed along different lengths

depending on the size of the wake, ranging from 40 mm for the case of $AoA = 0°$ to 160 mm for the case of $AoA = 20°$ with points nominally spaced 5 mm. Figure 3.18(b) reports the comparison between the drag force measurements employed.

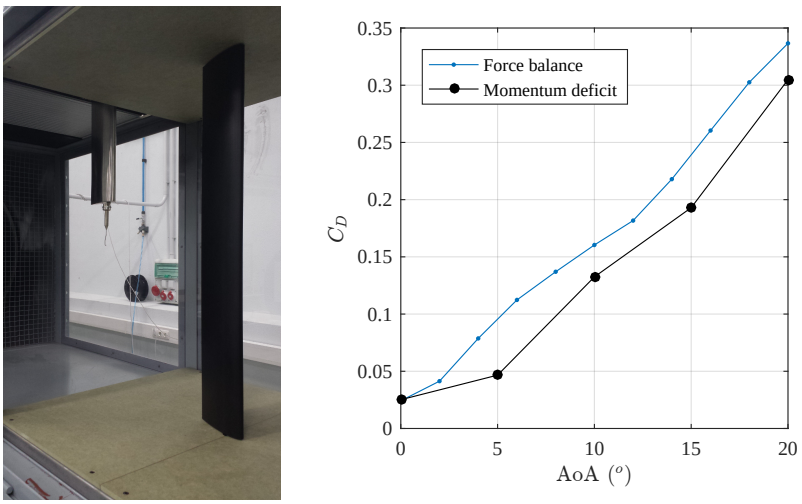

(a) (b)

Figure 3.18: Comparison between drag force measurement systems. (a) Experimental setup to obtain drag force by momentum deficit method (b) C_D coefficient

It should be noted here that the measurements are only taken over the center of the span. In order to obtain an accurate value for the drag coefficient, wake momentum measurements need to be taken at different spanwise locations to obtain the average drag at a given angle of attack. Since the interest is in obtaining another experimental value of the drag coefficient to validate the force balance measurements, it is believed that this single measurement can be used. This being said, it can be observed the drag values obtained with both methods are within a reasonable agreement. Comparing the drag value obtained by the momentum deficit method at $AoA = 10°$ ($C_D \approx 0.13$), it is observed that it is higher than the drag coefficients reported by Timmer [68] and Hansen *et al.* [65] ($C_D \approx 0.05$). These results suggest that the error committed in the drag curve is not caused by the force balance system.

This inaccuracy can be attributed to the model deficiencies observed in Section 3.2.2. The surface finish is sufficiently smooth to not alter the results. In contrast, the manufacturing defect observed in Figure 3.11(b) can cause an asymmetric behavior for a symmetric airfoil [71]. To clearly check the symmetry of the results, Figure 3.19 plots the drag and lift curves from $-14°$ to $14°$.

As can be seen, the drag curve is asymmetric. The slope discontinuities in the lower surface of the airfoil near the leading edge may produce this inconsistency (Figure 3.11 (b)). As pointed out by Graham [83], a discontinuity in curvature where the profile

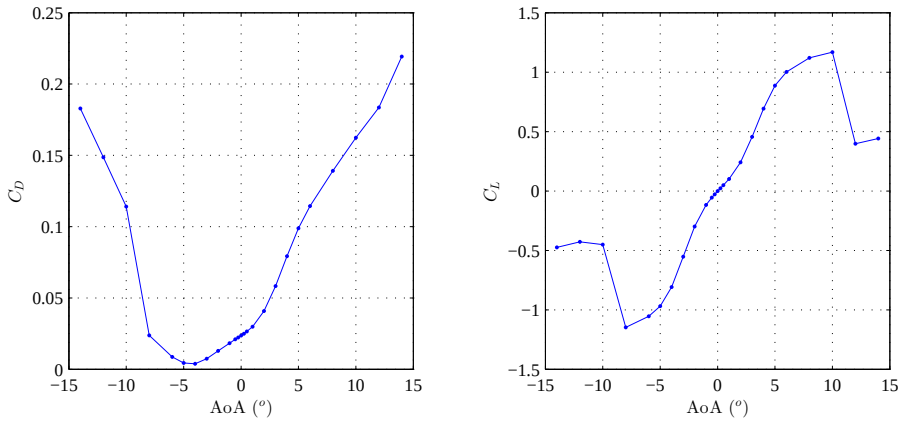

(a) (b)

Figure 3.19: Drag and lift polars for the NACA0021 at Re=10^5 obtained at the LSWT of MU (a) C_D coefficient (b) C_L coefficient

change from the small leading edge circle to the large circle of the basic profile can cause flow separation under low speeds. This lead to a premature drag rise rather than the delayed drag rise obtained with optimum airfoils.

This occurs when the model is rotated to positive angles (see Figure 3.14). The slope discontinuity near the leading edge is on the suction side and causes a premature flow separation increasing the drag values at positive AoA angles.In contrast, when rotating the model towards negative AoA, the suction side is free of imperfections. This results in an attached flow condition and generates lower drag values until stall condition is reached at $-8°$, where a sudden rise in the drag occurs.

Regarding the lift curve, a higher symmetry is obtained. The same maximum values of $C_L = 1.6$ are obtained before the stall at both sides, the de lift coefficient drops down to $C_L \approx 0.5$. The only difference in the location of the stall angle, which is around $-8°$ from negative AoA and $10°$ for positive angles.

3.4 Conclusions

In this chapter an experimental methodology is presented to measure the aerodynamic coefficients of an airfoil at Re = 100000. Due to the difficulties when dealing with airfoils at this regime, the most common sources of error are thoroughly investigated. The surface oil-flow visualization reveals that the LSWT conditions in the test section are well defined, as the characteristic flow regions are detected. In other words, the appearance of the laminar separation bubble indicates that the turbulence level and the acoustic excitation do not promote an early transition into turbulent state. In addition,

the use of splitter plates at the ends of the model ensures the two-dimensionality of the flow.

The uncertainty analysis performed for the force balance approach reveals that the error committed in the measurement of drag coefficient is under $\Delta C_D = 0.005$ and under $\Delta C_L = 0.011$ in case of lift coefficient. Furthermore, the results are in good agreement when compared with the momentum deficit method, confirming that the dynamometer has a resolution fine enough to not induce significant errors in the performance data measurements.

Once the different sources of errors are studied, it can be said that the differences observed in the drag measurements are caused by the small imperfections of the model. In spite of this inaccuracy, the results provided have an acceptable accuracy when compared to similar tests. These model inaccuracies may induce some misalignment with the incoming flow velocity during the balance alignment procedure adopted. This can result in additional errors due to the coupling effect between lift and drag.

Overally, it is believed that the current experimental methodology is well suited for the investigation of airfoils operating at low Re number. What is more, the lift curve is well captured, which is of interest here to analyse the effect of increasing free-stream turbulence levels on the stall behavior.

Chapter 4

Testing of airfoils in turbulent inflow conditions

Since vertical axis wind turbines (VAWT) and horizontal axis wind turbines (HAWT) operate in the atmospheric boundary layer (ABL), they are subjected to high turbulence intensity levels. It is acknowledged that free-stream turbulence (FST) can significantly alter the efficiency and power extraction of such devices. However, most available data in literature is obtained for aeronautical applications, which are characterized by a low turbulence level. This chapter aims to experimentally study the effect of free-stream turbulence on the aerodynamic performance of a NACA0021 airfoil.

With this purpose, a grid is installed at the entrance of the LSWT test section to generate prescribed turbulent inflow conditions. This technique permits to experimentally reproduce the high intensity turbulence levels that exist in the atmospheric boundary layer. Prior to this experiments, a preliminary study is done to characterize the decay of grid-generated turbulence in order to define the different turbulence levels to be tested. Subsequently, airfoil performance data measurements under these conditions are conducted.

4.1 Introduction

First, a summary of the basic theory behind the turbulent flow motions is provided, pointing out the notion of containing length and time scales defined in Kolmogorov's phenomenology of turbulence. Then, the most relevant techniques for studying the behavior of turbulent flows are collected from the experimental point of view.

4.1.1 Turbulence

Everyday life gives us an intuitive knowledge of turbulence in fluids: the smoke of a cigarette, the chaotic motion of a river, turbulence in an airplane etc. In spite of its constant presence, we have not found an appropriate definition of a turbulent flow. Lesieur [84] proposes tentatively the following definition of turbulence:

- Firstly, a turbulent flow is unpredictable, in the sense that a small uncertainty as to its knowledge at a given initial time will amplify so as to render impossible a precise deterministic prediction of its evolution.
- Secondly, it satisfies the increased mixing property. The readily available supply of energy in turbulent flows tends to accelerate the homogenization (mixing) of fluid mixtures. The characteristic which is responsible for the enhanced mixing and increased rates of mass, momentum and energy transports in a flow is called turbulent diffusivity.
- Thirdly, it involves a wide range of spatial and temporal scales. The third condition is maybe the one that represents the biggest challenge when dealing with turbulent flows: its multi-scale nature.

4.1.1.1 The notion of scales

Since the pioneering work by Richardson in 1922 [85], turbulence is considered as a multiple scale phenomenon which contains eddies of different sizes and scales. The mechanical energy is injected at some large scale structures. As these eddies become unstable, they split into many small eddies hence transferring their energy to the smaller ones. This process goes on until the Reynolds number of smallest scale structures becomes unity, resulting in the stability of eddies and hence, their energy is damped through viscous dissipation. This process is known as the *energy cascade*, Figure 4.1 gives an idea of it.

Although Richardson model gives a conceptually valid vision of turbulence, several fundamental questions remain unanswered: what is the size of the smallest eddies that are responsible for dissipating the energy? How many degrees of freedom have a turbulent flow? The idea of multiple scale nature of turbulence was formulated in the form of a theory by A.N. Kolmogorov in 1941 [86]. Using several hypotheses he devised a phenomenological theory which is known as Kolmogorov's Phenomenology of turbulence. A detailed discussion on this theory and its limitations may be found in Frisch [21]. Before going into the discussion on the Kolmogorov's phenomenology, which was actually based upon the Richardson's cascade theory, it is essential to define few characteristic length scales that are present in turbulent flows:

Big whorls have little whorls
that feed on their velocity.
And little whorls have lesser
whorls and so on to viscosity.

(a)

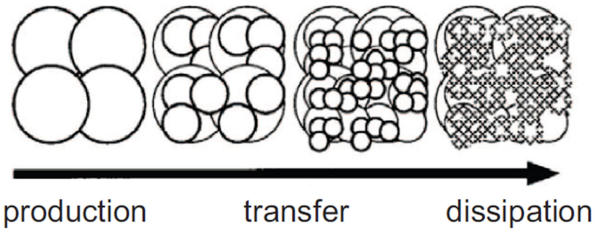

(b)

Figure 4.1: Richardson's idea of cascade of scales (a) Richardson's verses describing the notion of scales in turbulence inspired from a Jonathan Swift's verse. (b) Kolmogorov's illustration of Richardson's idea of cascade of scales (image taken from Manneville [16]).

- *Flow length scale or large scale* (L): this length scale is the characteristic of turbulence generation mechanism and mostly based upon the flow geometry. For example, while studying wakes behind a cylinder or sphere, this scale is the diameter of cylinder or sphere; in case of grid generated wind tunnel flow it is the mesh size of the grid etc.

- *Integral length scale* (l): in the developed turbulent flow region the integral length scale corresponds to the size of the largest eddy present therein.

- *Taylor microscale* (λ): an intermediate length scale which is much smaller than integral length scale and much greater than dissipative length scale.

- *Dissipative or Kolmogorov length scale* (η): this length scale is considered to be the smallest length scale present in turbulent flows at which all the injected energy that was transferred through the intermediate scales dissipates due to viscous dissipation.

Most of the complexities and the richness of turbulence lie in the entire range of scales between l and η (known as the inertial range of turbulence), where multiscale structures coexist and interplay in the energy cascade process. In this range specific statistical properties prevail due to local spatial and temporal correlations between eddies. At small scales (below η), the flow is dominated by viscous effects and becomes smooth, while at larger scales (above l) eddies are fully uncorrelated.

4.1.1.2 Taylor microscale

Local isotropy greatly simplifies the statistics of turbulence. Consider for example the average turbulence kinetic energy dissipation rate per unit mass ϵ, which is given by Hinze [87]

$$\epsilon = \nu \overline{\left(\frac{\partial u_i}{\partial x_j} + \frac{\partial u_j}{\partial x_i} \right) \frac{\partial u_j}{\partial x_i}}, \tag{4.1}$$

using tensor notation and summation on repeated indices, where ν is the kinematic viscosity. Here a Cartesian coordinate system $x_i = (x, y, z)$ is used with x-axis along the flow direction, y-axis normal to the solid surface and z-axis in the spanwise direction. The respective mean-velocity components in these directions are $U_i = (U, V, W)$ and the fluctuating components are $u_i = (u, v, w)$. Overbars denote time averages. If the dissipating range of eddy sizes is statistically isotropic, Equation (4.1) reduces to [88]:

$$\epsilon = 15\nu \overline{\left(\frac{\partial u_1}{\partial x_1} \right)^2}. \tag{4.2}$$

Moreover, Taylor introduced a turbulent length scale λ (known as *Taylor microscale*) defined as:

$$\lambda^2 = \overline{u_1^2} / \overline{\left(\frac{\partial u_1}{\partial x_1} \right)^2}, \tag{4.3}$$

in terms of which:

$$\epsilon = 15\nu \frac{\overline{u_1^2}}{\lambda^2}. \tag{4.4}$$

Although Taylor linked the length scale λ with that of the finest-scale eddies responsible for turbulence energy dissipation that has long been recognized as incorrect.

4.1.1.3 K41; Kolmogorov's phenomenology of turbulence

A.N. Kolmogorov developed the nowadays known statistical description of turbulence in 1941 [86]. A phenomenological description of the turbulent cascade, based on dimensional considerations and assuming homogeneous and isotropic turbulence (HIT) with a self-similarity of statistical properties of eddies within the inertial range of scales. The theory advanced by Kolmogorov is based on several hypotheses; Kolmogorov's first hypothesis of local isotropy, states that in the case of fully developed turbulence the small scales statistics are independent of their generation mechanisms. This implies the statistical restoration of symmetries which actually were broken by the turbulence generation mechanisms. This is valid for small scale structures away from boundaries. According to this proposition the large scales may still be anisotropic but the isotropy is recovered at inertial and dissipative scales. Furthermore, in his first similarity hypothesis Kolmogorov

stated that in the limit of high Reynolds number, the statistics of turbulent structures having scales much smaller than integral length scale can be universally determined only by viscosity ν and mean dissipation rate ϵ. In Kolmogorov's phenomenology the characteristic length, time and velocity scales below which the viscous effects dominate are determined through classical dimensional analysis as:

$$\eta = \left(\frac{\nu^3}{\epsilon}\right)^{1/4}, \tag{4.5}$$

$$\tau_\eta = \sqrt{\frac{\nu}{\epsilon}}, \tag{4.6}$$

and,

$$u_\eta = (\epsilon\nu)^{1/4}. \tag{4.7}$$

These dissipative length, time and velocity scales are often named after his name as Kolmogorov length scale η, Kolmogorov time scale τ_η and Kolmogorov velocity scale u_η respectively. The Reynolds number based upon these length and velocity scales verifies the relation:

$$Re_\eta = \frac{\eta u_\eta}{\nu}. \tag{4.8}$$

Note that the above mentioned length, time and velocity are known to be the smallest scales present in any turbulent flow and these represent the smallest eddies which dissipate in the form of heat all of the energy they have received from larger structures. The Reynolds number based on these scales is unity which conforms to the energy cascade idea of Richardson.

The second similarity hypothesis of Kolmogorov, states that in every turbulent flow at sufficiently high Reynolds number, the statistics of the motions at inertial range scales have a universal form independent of viscosity ν and uniquely determined by the energy dissipation rate ϵ. Figure 4.2 shows the spectral distribution of the turbulence energy. It indicates the energy contained by eddies $E(\kappa)$ as a function of the wave number κ, which is related to the size of previously described length scales present in turbulent flows (Section 4.1.1.1),

$$\kappa = \frac{2\pi}{\ell}, \tag{4.9}$$

where ℓ is the characteristic length of eddies.

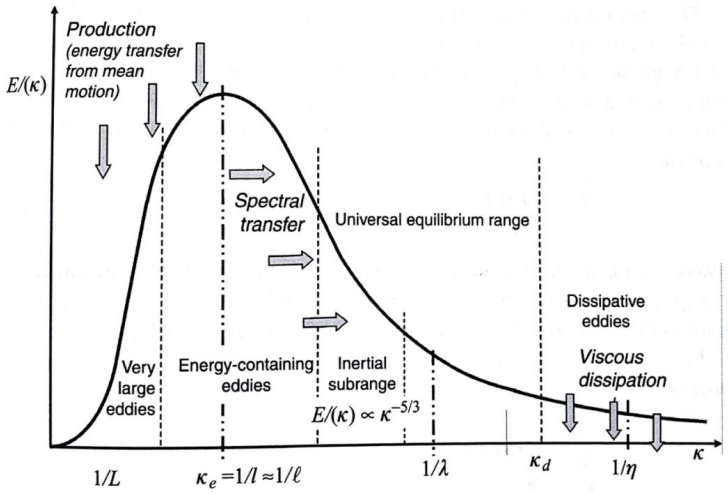

Figure 4.2: A schematic diagram of the energy spectrum for high Reynolds number turbulence (image taken from Hanjalic and Launder [17])

.

One of the big successes of K41 is the prediction of the spectrum of the kinetic energy of turbulent eddies (the celebrated $\kappa^{-5/3}$ law). It follows from Kolmogorov's first similarity hypothesis that, in the inertial subrange the spectrum is a universal function of ϵ and ν. From the second hypothesis it follows that, in the inertial range the spectrum is:

$$E(\kappa) = C\epsilon^{2/3}\kappa^{-5/3}, \tag{4.10}$$

where C is a universal constant. Sreenivasan *et al.* [89] study different types of flows, for high enough Reynolds numbers and found a value of $C = 0.53 \pm 0.033$. The $\kappa^{-5/3}$ law is plainly evident, as seen in Figure 4.3 which show data collected by Saddoughi and Veeravalli [18], where the slope in the inertial sub-range is $-5/3$.

However, as rapidly objected by Landau [90], K41 fails predicting one important statistical property of turbulence known as intermittency. This appears as the fact that energy dissipation (which is related to the viscous friction between fluid elements at small scales) is highly unevenly distributed in space. To account for intermittency, Kolmogorov proposed in 1962 a refined version of his self-similar phenomenology, including Obukhov suggestion [91] that the energy dissipation rate exhibits strongly non-Gaussian fluctuations. However the description of intermittency and its origins are still mysterious, and its modelling remains an active field of research [92], whose development still requires accurate experimental data (reference measurements for intermittency date back to the 90's [93]).

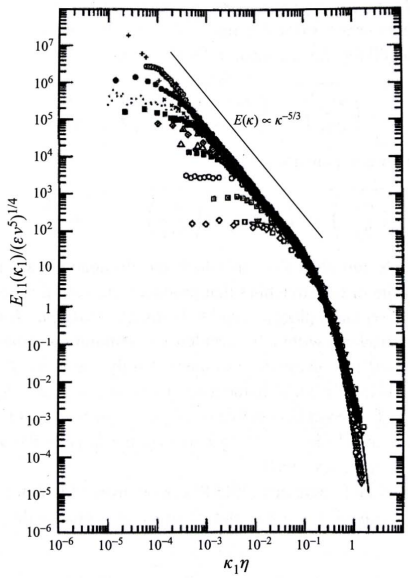

Figure 4.3: A collection of measured one-dimensional spectra in different flows at different Reynolds number (Image taken from Saddoughi and Veeravalli [18]).

4.1.2 Experimental characterization of turbulent flows

The flow field variables mentioned in Table 2.1 are independent of the reference frame due to Galilean invariance. This statement is true for flow variables (except for the velocity itself) and their gradients. However, it is not true for partial derivatives in time. The variation of the fluid-mechanics quantities between different flow elements could depend on their relative position and velocity, and thus on the way in which such quantities are evaluated. Therefore, it is not trivial to consider the differences between the flow description obtained at a fixed point (*Eulerian* description) and the one in motion (*Lagrangian* description).

From the experimental point of view, it is not simple to obtain fluid-mechanics variables along flow trajectories. Only a few techniques allow the *Lagrangian* description to be obtained. Among the others, the PTV (Particle Tracking Velocimetry) technique is now well established to derive tracer particle velocities along trajectories. Traditional approaches (including Kolmogorov phenomenology, Section 4.1.1.3) of turbulence are done in the *Eulerian* framework.

Statistical eulerian description of turbulent flows

An *Eulerian* measurement of turbulence is performed with a probe at a fixed location. This essentially consists of high resolution velocimetry measurements (Section 3.2.3). These measurements give access to important statistical quantities, including one point statistics of velocity and velocity gradients, but also multi-point statistics essential for

the investigation of turbulent spectra, correlations and structure functions, commonly used to describe scale by scale statistics and intermittency.

The problem of statistics is closely linked to the random nature of turbulent flows. The value of a fluid-mechanics variable at a given point and time can be considered as the sum of a mean term, plus a term containing all the information on coherent structures in the field (large and intermediate scales), plus a random term containing all incoherent fluctuations (small scales). The goal of this description is to try to separate the three contributions from each other to determine all possible effects to which the flow variable is subjected under the influence of the flow motion.

To study turbulence from a continuous record of measurements from a single point, it is necessary to assume that the turbulence is frozen. As the mean flow advects the eddies past the sensor, the fundamental properties of the eddies remain unchanged, or frozen, a strategy known as Taylor hypothesis of frozen turbulence [88], that mathematically can be expressed for any variable ϕ that can be used to study turbulence as follows:

$$\frac{d\phi}{dt} = \frac{\partial\phi}{\partial t} + U\frac{\partial\phi}{\partial x} + V\frac{\partial\phi}{\partial y} + W\frac{\partial\phi}{\partial z}, \tag{4.11}$$

Where the respective mean-velocity components in the directions x, y, z are U, V, W. Since the turbulence is frozen, total derivative is equal to zero $\frac{d\phi}{dt} = 0$, and the expression 4.11 can be written as:

$$\frac{\partial\phi}{\partial t} = -U\frac{\partial\phi}{\partial x} - V\frac{\partial\phi}{\partial y} - W\frac{\partial\phi}{\partial z}. \tag{4.12}$$

Figure 4.4 gives an example on how this hypothesis is applied.

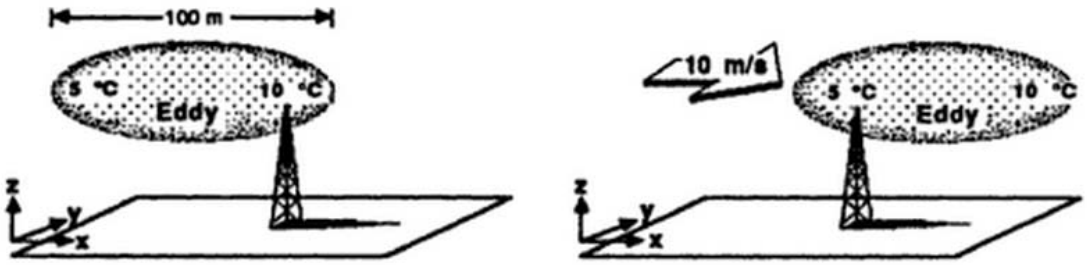

(a) (b)

Figure 4.4: Illustration of Taylor Hypothesis. (a) An eddy that is 100 m in diameter has a $5°C$ temperature difference across it. (b) The same eddy 10 seconds later is blown downwind at a wind speed of 10 m/s (image taken from Stull [19])

Considering the example in the Figure 4.4, and assuming that the flow is entirely in the x direction, the local change is given by:

$$\frac{\partial \phi}{\partial t} = -U \frac{\partial \phi}{\partial x}. \tag{4.13}$$

Through this expression, it is possible to obtain a reasonably accurate estimate spatial velocity derivative from the (simpler to measure) rate of velocity variation with time at the point in question. This relation is valid if the flow turbulence level I is low ($I = u/U << 1$, where u is the fluctuating velocity and U is the mean-rate velocity) and the translational velocity is uniform. Then, the substitution $t = x/U$ is a good approximation.

Prerequisites for Measurements in Turbulent Flows

Turbulent flows involve several features that makes their characterization a difficult task. The main difficulties can be resumed as follows:

- Extreme sensitivity to initial and boundary conditions
- Unpredictability and randomness
- Wide range of scales in space and time
- Fully three-dimensional nature

Due to the previous considerations, there are some peculiar characteristics of a measuring system to be considered when dealing with turbulent flows experimentally.

Spatial and time resolution

To resolve the wide range of scales observed in turbulent flows, a measurement system should be able to identify rapid changes in fluid-mechanics variables both in space and time. To do this, the probe of the system, must be small enough compared to the smallest spatial scale in the flow and must respond at least as quickly as the smallest time scale of the flow.

The spatial resolution is the inverse of the minimum detectable length in the flow field $SR = 1/d_{min}$, where d_{min} is related to the characteristic size of the sensor. A system with high spatial resolution is able to perform a measurement over a small length. For example, in hot-wire anemometry, the sensor is a thin wire (diameter of a few microns) and $SR \approx 10^5$ m^{-1}, while a Pitot tube (with a hole diameter of about 3 mm) has $SR \approx 10^2$ m^{-1}. In this sense, hot wire anemometry is able to detect small moving spatial structures of the velocity much better than a Pitot tube.

Similarly, the time resolution is the inverse of the minimum detectable time interval in the flow field $TR = 1/\Delta t_{min}$, where Δt_{min} is the maximum time among the time interval requested by the whole measurement system to perform a measure (measurement interval) and the time interval for the sensor to respond to a variation of the considered fluid-mechanics variable (the response time). A system with high time resolution is able to take measurements separated by small time intervals and to capture fast fluctuations. For instance, in hot wire anemometry, due to the small sensor size and the fast electronics, the system takes a measurement quite rapidly (it is really an analogue system which is resampled digitally) so that $TR \approx 10^5$ Hz. In contrast, for Pitot tubes the inertia of the manometer fluid limits the time interval to a fraction of a second, so that $TR \approx 10^1$ Hz. However, modern pressure transducers are able to respond quite rapidly to pressure changes ($TR \approx 10^3$-10^4 Hz).

The smallest (d_{min}, Δt_{min}) and largest (d_{max}, Δt_{max}) measurable lengths and times must be evaluated preliminarily for the measurement system under consideration and compared to the expected flow scales to know the effective range that can be investigated. When considering the distribution of energy among the different wavenumbers, the sampling theorem states that the energy content can be effectively detected only up to $\kappa_{max} = \pi/d_{min}$. In the same way, for the distribution of energy among the different frequencies, the sampling theorem states that the energy content can be effectively detected only up to $f_{max} = 1/(2\Delta t_{min})$. In this sense, the spatial and temporal resolutions correspond to two times the maximum wavenumber and frequency which can be detected by the measurement system.

Grid-generated turbulence

In this study, the canonical case of homogeneous and isotropic turbulence (HIT) is considered, which remains a unique playground for the investigation of fundamental properties of turbulence. It is by far the most documented configuration of turbulence and the field of predilection for the development of models. From the experimental point of view, HIT flow conditions are known to be almost perfectly achieved in grid-generated turbulence [20]. Such grids are commonly used to characterize fundamental properties of turbulence.

Figure 4.5 shows the typical configuration of a passive grid, which consists of a series rods arranged forming a uniform mesh of size M. In the region just downstream the grid the wakes of the rods interact and turbulence is produced (production zone) which results in an increase of fluctuations. Once the turbulent flow is developed, its energy is transferred into successive smaller eddies and it is finally dissipated at small scales by viscosity. This technique experimentally reproduces the Richardson's idea of cascade of scales.

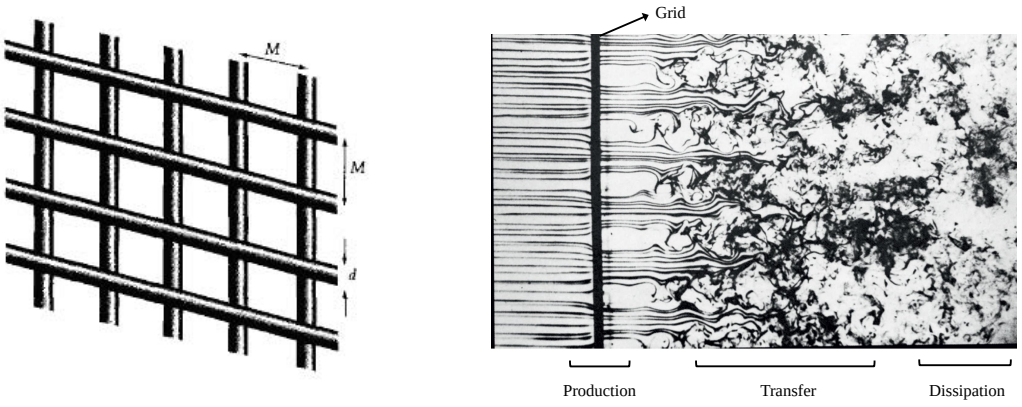

(a) (b)

Figure 4.5: Schematic view of grid-generated turbulence (a) Passive grid configuration (image taken from Pope [20]); (b) Turbulence generated by a passive grid (image adapted from Frisch [21])

This type of test is usually done in a wind tunnel, where a grid is located at the entrance of the test section and turbulence statistics are recorded downstream of the grid. The flow is statistically stationary; statistics only vary in the x direction. In the frame moving with the mean velocity U, the turbulence is homogeneous, and it evolves with time ($t = x/U$). Taylor's frozen turbulence hypothesis for time transformation into space can be used [88]. In the following Figure 4.6 a typical sketch for grid generated turbulence in a wind tunnel, together with the decay of isotropic turbulence along the streamwise length of the wind tunnel. The distance is normalized by the mesh size (x/M).

In the absence of external forcing, this results in the continuous decay of the observed energy of fluctuations. The downstream interaction of the wakes of the rods forming the grid generates a turbulent velocity field which is empirically known to become statistically homogeneous and isotropic (if the grid has the proper solidity, of the order 30-40 %) at a distance of the order of 30 mesh-sizes from the grid. The generated turbulence is then statistically stationary and statistics only vary in the x (streamwise) direction as turbulence decays.

According to Pope [20], the rate of decay of the turbulence kinetic energy k, and the rate of growth of the integral scale L, defined as the velocity correlation scale, evolve according to power laws in the streamwise direction, as follows:

$$\frac{k}{U^2} = A\left(\frac{x - x_o}{M}\right)^{-n}, \tag{4.14}$$

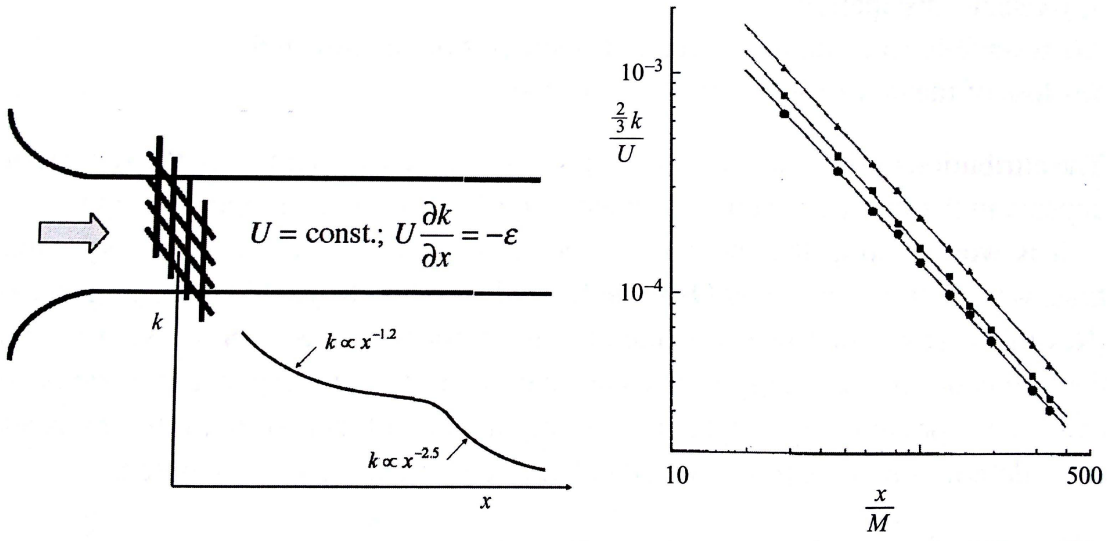

(a) (b)

Figure 4.6: Decay of isotropic turbulence generated by a grid in a wind tunnel. (a) a sketch of the experiment (image taken from Hanjalic and Launder [17]). (b) Experimental results for the inertial period (image taken from Comte-bellot and Corrsin [22]

and,

$$\frac{L}{M} = A'\left(\frac{x - x_o}{M}\right)^{n'}, \tag{4.15}$$

where U is the flow mean velocity, x is the streamwise distance from the grid along the tunnel and M is the mesh spacing. The A, A', x_o, n and n' are parameters to be determined experimentally. From the decay of the average kinetic energy, it is then possible to deduce the decay of energy dissipation ($\epsilon = Udk/dx$) and therefore the downstream evolution of the dissipative scale of the flow ($\eta = \sqrt[4]{\nu^3/\epsilon}$) as well as the dissipative time scale ($\tau_\eta = \sqrt{\nu/\epsilon}$). Characterizing the decay of turbulence as given by Equations (4.14) and (4.15) therefore allows to extract most of the relevant global characteristics of the turbulent flow.

The prediction of these decaying exponents leads to a deep analysis. There has been a longstanding debate as to whether the large scales in grid turbulence is classified as of the Batchelor [94] or Saffman [95] type. Depending on the value of n exponent, different types of decay exist, Saffman ($n = 6/5$) and Batchelor ($n = 10/7$), as discussed by Krogstad [96]. Note that the theoretical understanding of the physical mechanisms of turbulence decay (even for the case of HIT) is far from being complete, in spite of more than fifty years of research. New approaches based on Langevin equation for big structures, recently introduced by A. Llor and co-workers [97] may offer an interesting unifying framework. Besides the existence of a slow transient of the decay has been

recently proved by the A. Llor and co-workers (private communication), gives a clear theoretical base to explain the extreme difficulty to determine experimentally such decay coefficient.

There have been many measurements of decay exponents over the years. Comte-Bellot & Corrsin [22] found $1.15 < n < 1.29$ and Warhaft & Lumley [98] estimated $n = 1.34$, to mention just a few obtained coefficients. In most cases the uncertainty in the determination of the exponent is linked to the unknown virtual origin x_o. In recent years, numerous wind tunnel experiments have been focused on homogeneous turbulence generated by different type of grids; passive [96, 99], active [100, 101], and multiscale (fractal) [102, 103, 104, 105]. Decaying isotropic turbulent flow has long served as important benchmark test case for turbulence theories, models, and computer simulations.

4.1.3 Free-stream turbulence effect on airfoils

When planning any wind tunnel experiment or numerical simulation, the Reynolds number must be considered to properly simulate the ratio of inertia to viscous forces and to ensure the validity of the results. The turbulence characteristics of the incoming flow are also important parameters that need to be addressed. The aerodynamic behavior of an airfoil can be strongly affected by the FST level both qualitatively and quantitatively, specially in the angle range near the stall. Despite the relevance of the inflow turbulence effect on the aerodynamic performance, most available data in literature is obtained for aeronautical applications, which are characterized by a low turbulence level (less than 1 %) and low AoA. However, there are applications that are subjected to high FST levels, such as HAWT and VAWT, which operate inside the atmospheric boundary layer (ABL). The turbulence level in the ABL can vary from 5 % (offshore) to 25 % [106, 107]. These high turbulence levels can be originated from the shear in the ABL or from the wake of other wind turbines if they are placed in a wind farm.

Generally, VAWTs have symmetrical blade profiles with relatively high thickness-to-chord ratio (NACA0018 [68], NACA0021 [65]) as a balance between aerodynamic performance and structural integrity. For thick airfoil sections, boundary layer separation typically initiates from the trailing edge and gradually progresses towards the leading edge with increasing AoA [65]. The stall characteristics are then more gradual compared to thinner airfoil sections, where the separation initiates from the leading edge, causing a sudden loss in lift. Therefore, thick airfoils are desirable in applications where the wind speed can be variable such as the inflow conditions in wind turbine blades, as more gradual stall characteristics increases efficiency and reduces noise emissions.

Inflow turbulence is often neglected due to the complexity of measuring in situ the real flow characteristics and simulating them in a wind tunnel or in numerical models.

A common technique to generate prescribed turbulent flow conditions is the use of grids (Section 4.1.2) at the entrance of the test section [77, 108, 109, 54, 53, 110].

One of the most complete study is the work done by Devinant *et al.* [54]. They used three grid with different design parameters (mesh size M and rod thickness d) at a fixed location upstream the NACA 65-421 to generate turbulence levels from 0.5 % to 16 % and for Re numbers between 100000 and 700000. As these low-power wind turbines airfoils may operate at angles of attack beyond the stall, the tests were conducted for a very broad AoA range from $-10°$ to $90°$. Their results were consistent with previous experimental tests [77, 108], as they observe that high turbulence levels have a major effect on the aerodynamic properties, as the stall angle is delayed with increasing turbulence level. They concluded that turbulence effect should be considered to develop a correct description of these phases of wind turbine operation in which part of the blade is stalled.

Sicot *et al.* [53] extended the previous work of Devinant *et al.* [54] by including PIV measurements to obtain a global overview of the flow around the airfoil. PIV measurements illustrated the formation of two shear shear layers, one from the leading edge and one from the trailing edge, where Kelvin-Helmholtz instabilities developed, and further downstream, the appearance of the Von Karman vortex. In addition, the spectral analysis of the aerodynamic load fluctuations together with the simultaneous surface pressure measurement around the airfoil showed that neither the inflow turbulence level nor the Re number have a significant effect on von Karman vortex shedding frequency.

Torres-Nieves *et al.* [111] studied the effect of free-stream turbulence (FST) with levels up to 6.14 % generated by an active grid [101]. A 0.25 m chord model with an S809 profile, common for horizontal-axis wind turbine applications, was tested at a wind tunnel speed of 10 m/s, resulting in Reynolds numbers based on the chord of Re ≈182,000. Results indicate that when the flow is fully attached, turbulence significantly decreases aerodynamic efficiency. In contrast, when the flow is mostly stalled, the effect is reversed and aerodynamic performance is slightly improved. Analysis of the mean flow over the suction surface shows that free-stream turbulence is actually advancing separation, at stall conditions, particularly when the turbulent scales in the free-stream are of the same order as the chord. This results are then consistent with the mentioned studies where passive grids were employed to generate free-stream turbulent conditions.

4.2 Generation of high FST levels

The NACA0021 airfoil is commonly used in VAWT applications, where high turbulence levels are expected. For this reason, a comparative analysis is performed at different FST turbulence levels. To generate prescribed turbulent flow conditions, a passive grid (Section 4.1.2) is installed in the test section upstream the model. The downstream interaction of the wakes of the rods forming the grid generates a turbulent velocity field. Figure 4.7 shows a sketch with the grid design parameters used.

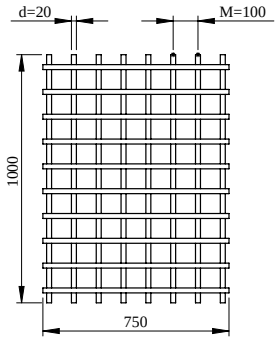

Figure 4.7: Grid design parameters (dimensions in mm)

The grid is comprised of 8 vertical per 10 horizontal bars that fully covers the cross-sectional area of the test section. The mesh spacing is M= 100 mm and the thickness of the bars is d=20 mm, what results in a solidity of 36 %. This grid solidity is between 30-40 %, which is empirically known to become statistically homogeneous and isotropic at a distance of the order of 20 mesh-sizes from the grid.

Devinant *et al.* [54] placed the grid at a fixed distance far enough upstream the test section so that the turbulence generated is assumed to be homogenous when reaching the airfoil. They created different turbulence levels by changing the topology of the grids. Three different grids employed with mesh sizes of 100, 280, 360 mm produced mean longitudinal turbulence levels of 4.1 %, 9.7 % and 16 %, respectively. They stated that recorded turbulence levels were equal in the other two directions so the turbulence created was nearly isotropic.

In the work done by Swalwell and Sheridan *et al.* [108], turbulence was generated by the same grid placed at different locations upstream the model. The turbulence intensities and scales of the generated turbulence were just cited and no mention on the homogeneity and isotropy conditions was made.

In the current investigation, the same methodology is followed, a unique grid is used at three different locations (x/M= 5 / 10 / 15, being x the streamwise distance from the grid to the pivot point of the airfoil located at $0.3c$). In order to study the turbulence

characteristics that the model experiences, the turbulence intensity is measured along the streamwise direction. Figure 4.8 (a) shows the points where the measurements are taken. This measurements are performed at the middle height of the test section and centered with respect to the wind tunnel width. To have a more general view of the turbulence flow properties reaching the airfoil, some 2D maps are also captured at the limit positions (x/M=5 and x/M=15). Figure 4.8(b) shows the points for the 2D contours. A total of 45 points are taken with an spacing between each other of 50 mm. The points are coincident with the midpoint of the vertical and horizontal bars, with the junction between the bars, and also with the middle of the mesh spacing, where maximum differences are expected.

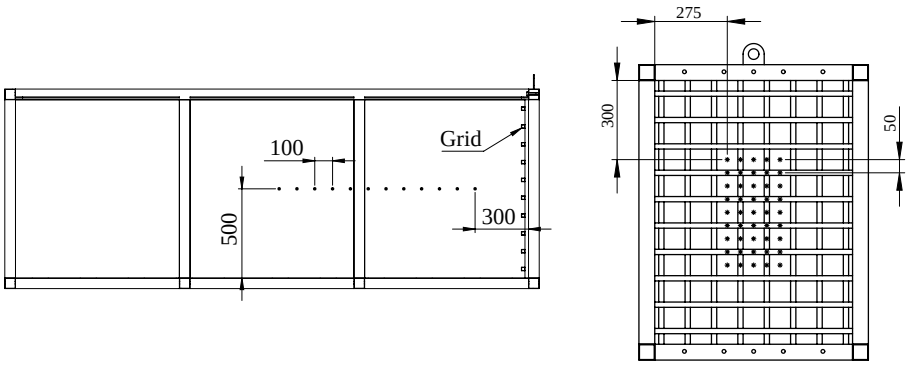

(a) (b)

Figure 4.8: Location of the experimental measurements (a) Points were the measurements are taken to measure the decay of turbulence (dimensions in mm) (b) Points for the 2D map at $x/M = 5$ and $x/M = 15$ (dimensions in mm)

The data sampling frequency is set to 2500 Hz and the acquisition time is 30 seconds. Since the airfoil is to be tested at a chord Re number of $\mathrm{Re} = 10^5$, the velocity is set to $U = 10$ m/s. It should be noted here that the presence of turbulence grids in the flow creates head losses in the wind tunnel circuit, so the rotational speed of the fan needs to be increased to reach the desired velocity. Figure 4.9 shows the decay of the turbulence intensity along the test section length.

Given the mesh size employed and the test section length upstream the model, the generated turbulence is expected to be anisotropic and inhomogeneous, since the model is located below $x/M < 20$. Figure 4.10 shows the turbulence intensity variation across the 2D contours plots obtained. Dotted lines are plotted simulating the grid to see the location that corresponds to the measurement.

The results show relatively high differences for the case of $x/M = 5$. According to Figure 4.9, the turbulence intensity is ≈ 14 %. However, values up to 15 % are reached in some points that coincide with the mesh gap. The presence of the grid is still notorious in the wakes behind the grid, since lower turbulence intensity values are obtained. Behind

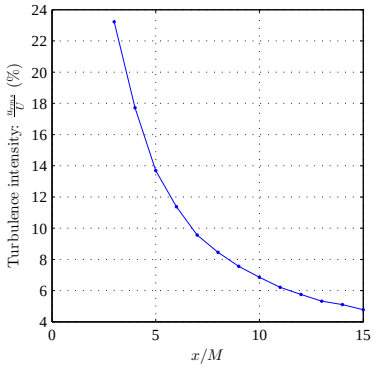

Figure 4.9: Turbulence decay along the streamwise direction

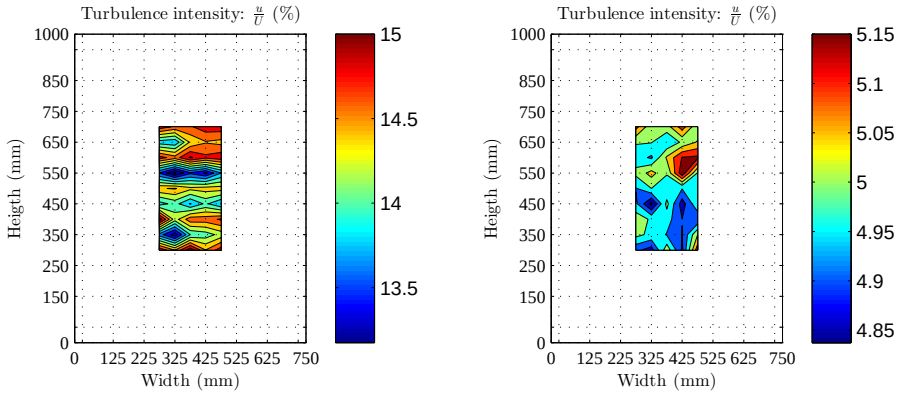

(a) (b)

Figure 4.10: Turbulence intensity variation at different cross-planes: (a) $x/M = 5$ (b) $x/M = 15$

the horizontal bars, values below 13.5 % are measured. The results show a more gradual distribution of the turbulence intensity for the $x/M = 15$ cross-plane. An approximated value of ≈ 5 % is obtained at the center while the upper and lower limits are within $\pm$ 0.15 % for the rest of the points analyzed.

Table 4.1 summarizes the turbulence intensity value at each location.

Table 4.1: Turbulence intensity decay at different locations

x/M	5	10	15
$I(\%)$	14	7	5

4.3 Low Re airfoil measurements under different FST levels

The experimental tests are arranged to analyze the effect of high turbulence levels on the aerodynamic properties of the NACA0021. With this purpose, the grid is installed upstream the airfoil at three positions to produce the intensity levels noted in Table 4.1. Figure 4.11 shows a photo of the experimental setup where the grid located at the maximum upstream distance of x/M=15.

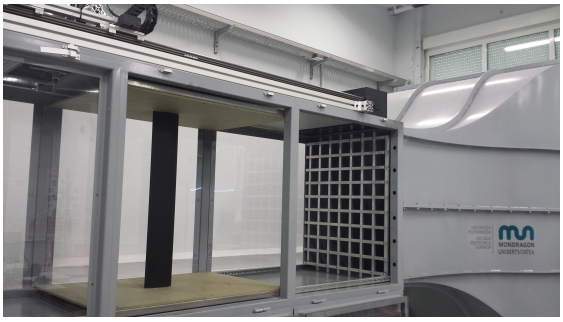

Figure 4.11: Experimental setup arranged for the investigation of FST level effect on aerodynamic coefficients of a NACA0021 airfoil.

The measurements are compared with the data obtained without grid installed inside the test section. Figure 4.12 shows the drag and lift polars obtained under the different FST levels tested. The measurement under smooth flow conditions is named as I =0.3 %, which is the value of the turbulence intensity with the empty test zone (Section 2.3.2). The other measurements are named according to the intensity level that reaches to the airfoil at that grid position (Table 4.1). The angle of attack is increased from $-4°$ to $40°$ with increments of $2°$.

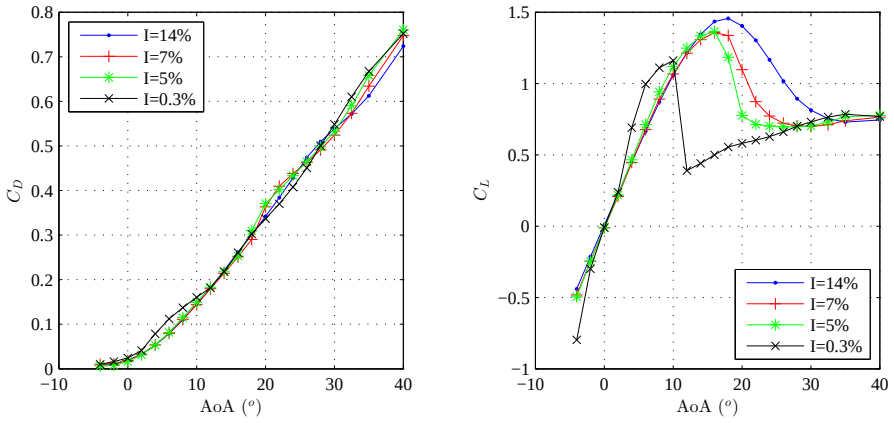

(a) (b)

Figure 4.12: Aerodynamic coefficients under different FST levels (a) C_D curve (b) C_L curve

The results obtained are consistent with previous investigations [77, 108, 54]. Drag curve does not experience significant changes with increasing turbulence. The main interest is on the lift curve and the stall characteristics.

As noted before in Section 3.3.3, the slope of the lift curve for AoAs prior to stall is not linear as a consequence of the formation of a laminar separation bubble (LSB). The drop of the C_L value is caused by the sudden jump of the separation point from the trailing edge region to the leading edge. This leading edge stall is generally due to the behavior of the LSB located in the downstream vicinity of the leading edge [54].

In contrast, the presence of turbulence promotes the transition and eliminates the LSB. As a result, the linear range of the lift curve is extended and the maximum lift is increased. This effect is also observed in the experiments performed by Hoffmann [77] and Swalwell [108].

Consistent with this investigations, the $C_{L_{max}}$ value is maximized with the increasing turbulence, and the higher turbulence level, the more gradual stall characteristics. This is due to the fact that inflow turbulence increases the transport of momentum from free flow to the inner region of the boundary layer [76]. This increases the resistance against adverse pressure gradients, so the boundary layer separation point advances along the leeward surface of the airfoil and thereby reduces separation at high incidences corresponding to airfoil stall [54].

At higher incidence angles, the entire leeward surface is stalled and the aerodynamic loads result essentially from surface pressure differentials between upper and lower surfaces [54]. This is the reason why the the lift curves converge upon reaching high incidence angles ($AoA > 30°$).

4.3.1 Hysteresis effect

Turbulence has also a considerable effect on the hysteresis cycle of rounded nosed airfoils at low Re number. To analyze the influence of high FST levels on the lift curve, the angle of attack is gradually increased until a post stall situation is reached. Afterwards, the angle of attack is decreased. The angle increments near the stall are diminished to have a better resolution in this zone. Figure 4.13 plots the hysteresis cycles for the smooth flow, and for turbulence intensities of 5 % and 7 %.

The laminar separation bubble present for the smooth flow case is responsible for producing the hysteresis cycle at 0.3 %. As the angle of attack increases from an attached flow condition, the lift curve is maximum. At this situation, the adverse pressure gradient can be strong enough to burst a short bubble into a long one, producing a massive separation and deteriorating the airfoil performance. When the angle of attack is reduced

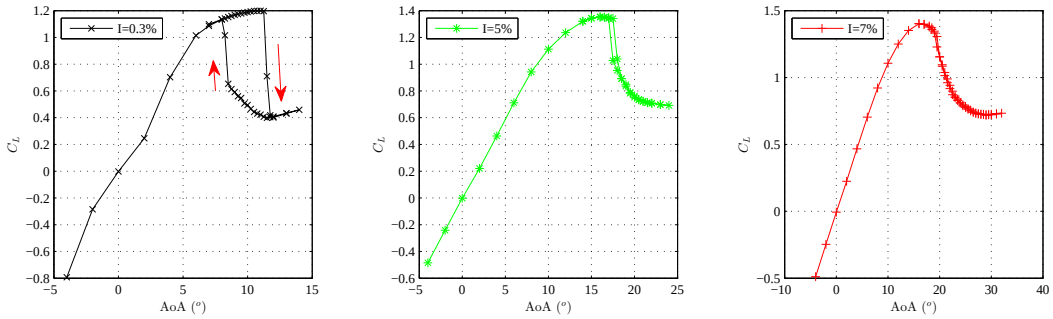

(a) (b) (c)

Figure 4.13: Hysteresis effect on C_L under different FST levels (a) $I = 0.3\%$ (b) $I = 5\%$ (c) $I = 7\%$

after bursting, a short bubble is not immediately recovered producing the hysteresis loop.

It can be observed from the case of 5 % that the length of the separation bubble is reduced causing a smaller hysteresis loop. For the case of 7 %, the higher level of turbulence here can cause the boundary layer to transition to turbulence before separation and therefore eliminate the separation bubble altogether. This behaviour was also observed by Hoffmann [77], who found that below a certain threshold the loop grew in size as turbulence intensity dropped down.

4.4 Conclusions

A passive grid is installed in the test section to generate prescribed turbulent inflow conditions. The decay of the grid-generated turbulence is measured to obtain the turbulence level as a function of the downstream distance of the grid. This relation serves to define the desired turbulence level with the grid distance upstream the airfoil. Consistent with the empirical rules which establish that HIT conditions are not achieved until $x/M = 20$, the turbulence intensity mappings performed at $x/M = 5$ and $x/M = 15$ suggest that the generated flow properties are anisotropic and inhomogeneous.

Regarding the performance data measurement under different FST, the results are in accordance with the available studies in literature. The presence of turbulence promotes the transition and eliminates the laminar separation bubble. As a result, the linear range of the lift curve is extended and the maximum lift is increased. Another consequence of the elimination of the LSB is on the hysteresis cycle, which is gradually reduced with the increasing turbulence until it is totally eliminated for a turbulence level of 7 %.

Chapter 5

Modelling of the decay of grid-generated turbulence

The motivation of the present chapter is to use RANS solutions as a tool to design passive grids with prescribed turbulent characteristics. These simulations permit more robust analysis than the few empirical rules generally employed to characterize the downstream turbulence decay. Due to its low computational cost compared to DNS or LES, parametric studies are easier to achieve with RANS solutions to investigate the role of the solidity, global grid size, mesh size and number of rods.

The objective is then to test the ability of different turbulence models to capture the large scale properties of decaying grid-generated turbulence for design purposes of the grid. The numerical simulations are prepared to reproduce the experiments performed at *Laboratoire des Ecoulements Geophysiques et Industriels* (LEGI), where a $\mathrm{Re}_\lambda = 100$ based on the Taylor microscale is obtained downstream a passive grid. These experiments are then used to validate the numerical simulations.

It is noteworthy here that the development of such a design tool was motivated by the need to prepare a very large scale grid turbulence experiment that was performed in 2014 in the S1MA wind tunnel of ONERA in Modane (France), in the frame of ESWIRP European project [112, 113].

5.1 Introduction

Despite the complexity of the properties of turbulent flows, it is possible to predict the fluid motion. The Navier-Stokes equations, named after Claude-Louis Navier and George Gabriel Stokes, describe the motion of fluid substances. These equations arise from applying Newton's second law to fluid motion, together with the assumption that the stress

in the fluid is the sum of a diffusing viscous term (proportional to the gradient of velocity) and a pressure term, and hence, describing viscous flow. The instantaneous velocity field in a turbulent flow is described by the continuity and the momentum (Navier-Stokes) equations by expressing the conservation of mass and momentum (Newton's second law) for an infinitesimal control volume in space, which in conservative form in the absence of body forces may be written as:

$$\frac{\partial \rho}{\partial t} + \frac{\partial}{\partial x_i}(\rho U_i) = 0, \tag{5.1}$$

and,

$$\frac{\partial}{\partial t}(\rho U_i) + \frac{\partial}{\partial x_j}(\rho U_i U_j) = -\frac{\partial P}{\partial x_i} + \frac{\partial}{\partial x_j}\left[\mu\left(\frac{\partial U_i}{\partial x_j} + \frac{\partial U_j}{\partial x_i} - \frac{2}{3}\delta_{ij}\frac{\partial U_k}{\partial x_k}\right)\right], \tag{5.2}$$

where P denotes pressure, ρ and μ are the density and dynamic viscosity of the fluid respectively. The term in square brackets is in fact the viscous stress, τ_{ij}, for a Newtonian fluid. Together with the pressure it represents the total stress, i.e. the force per unit area acting on the surface of an elementary fluid control volume. This equation with appropriate boundary condition contains all the turbulent phenomena (at least for classical systems). The problem is that Navier-Stokes equation is highly non-linear and analytical solutions are extremely scarce. On the other hand, the multi-scale nature of turbulence (both in time and space), makes numerical analysis extremely expensive, considering that short and long time and space scales must be resolved simultaneously. Because of the range of scales to be resolved, from the fine-scale dissipative motions to the complete flow field, it is only feasible, currently, to carry out a direct numerical simulation (DNS) of turbulent flow for relatively simple shear flows for overall Reynolds numbers typically of order 10^4 with a supercomputer. As expected, the computational cost of these simulations is huge. Some form of modelling is essential to compensate for being unable to resolve directly all the turbulence scales as well as the mean flow.

Two broad strategies for modelling are commonly employed:

- *Large-eddy simulation* (LES) where one resolves as large a proportion of the turbulent fluctuations as one judges necessary (or can afford) and applies a *sub-grid-scale* (SGS) model to account for the effects of those motions of a finer scale than the adopted mesh.

- *Reynolds averaging of the Navier-Stokes* (RANS) equations in which the effects of all the turbulent fluctuations are subsumed within the termed *turbulence model.*

A comparative illustration of the numerical resolution of turbulent flow in a pipe or

channel required by these different numerical approaches - DNS, LES, RANS - is shown in Figure 5.1.

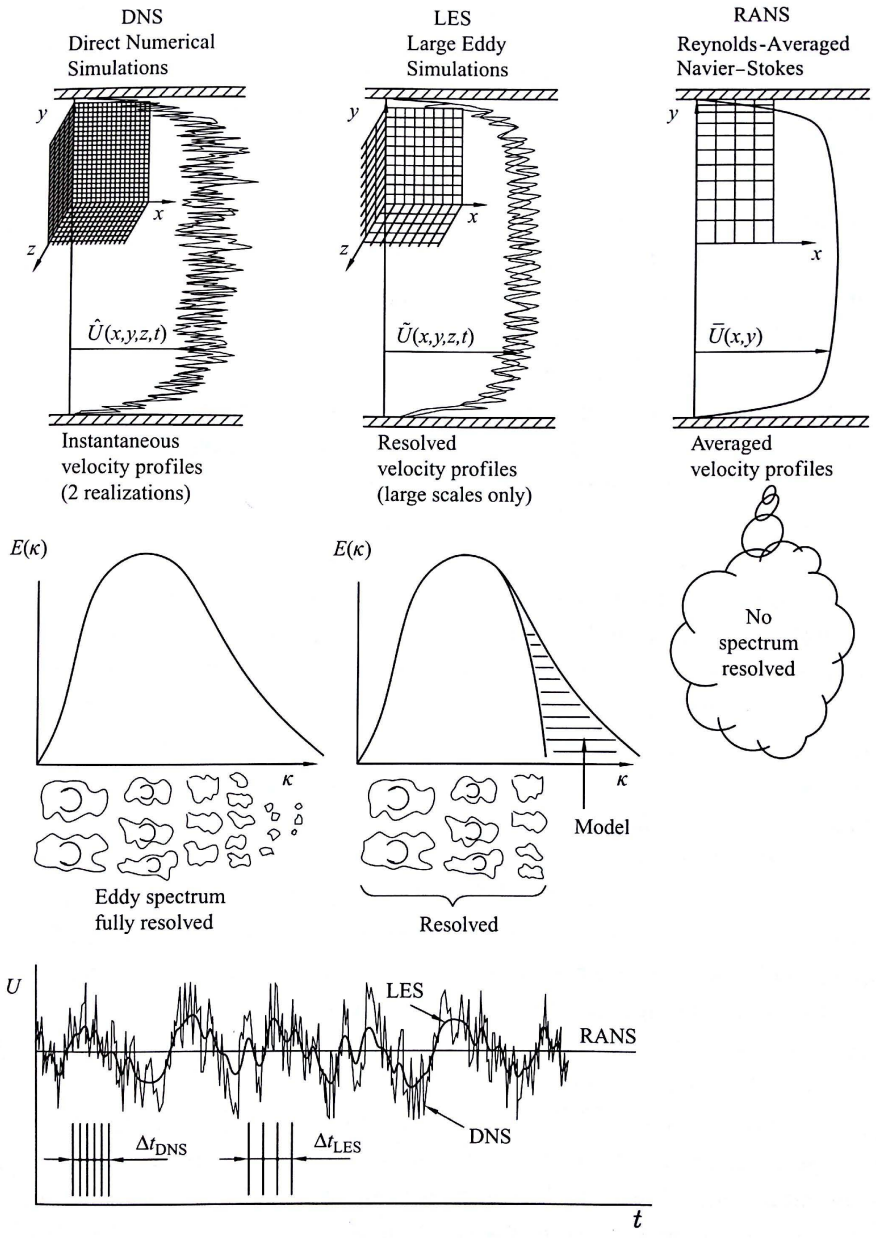

Figure 5.1: Illustrative comparison of DNS, LES and RANS simulations of a fully developed, steady turbulent flow in a pipe or a plane channel (image taken from Hanjalic and Launder [17])

A random-like oscillating signal with sharp peaks provides a snapshot of the true instantaneous velocity, in a vertical cross plane. A properly resolved DNS (with the computational cells smaller than the smallest important eddy size) provides the complete range of wavelengths of velocity fluctuations. The instantaneous velocity profile obtained

by LES also shows a range of wavelengths, but because the computational mesh is coarser, the signal is somewhat smoother. High frequencies, in those with a wavelength smaller than the computational cells, are absent because they have been filtered out. Finally the RANS simulation exhibits a smooth profile that can be obtained with a much coarser two-dimensional grid.

The second row of figures illustrates the resolved energy spectrum $E(\kappa)$ determined using each of methods. Naturally, DNS should provide the complete spectrum while LES excludes only the high wave number portion (beyond $\kappa = 2\pi/\Delta$, where Δ is the characteristic mesh size). In contrast, RANS provide no information about the turbulence spectrum.

The bottom figure illustrates a time record of fluid velocity at a point is space in a steady flow. Again, the strongly oscillating peaky signal (such as would be recorded by a hot-wire anemometer) is representative of a typical DNS velocity fluctuations. The smoother oscillating signal is a typical LES result, whereas the RANS record would simply give a constant value. Resolving the DNS signal requires very small time steps, whereas LES tolerates a somewhat larger time step corresponding with the coarser computational mesh.

5.1.1 Reynolds Averaged Navier-Stokes Equations (RANS)

In Reynolds averaging, the solution variables in the instantaneous (exact) Navier-Stokes equations are decomposed into the mean (ensemble-averaged or time-averaged) and fluctuating components. For the velocity components:

$$U_i = \overline{u}_i + u'_i, \tag{5.3}$$

where $\overline{u}_i$ and u'_i are the mean and fluctuating velocity components ($i = 1, 2, 3$). For the turbulent flow of a Newtonian fluid, by introducing the decomposition in Equation (5.3) into the Navier-Stokes equations 5.1 and 5.2, the resulting the continuity equation and the Reynolds-averaged Navier-Stokes (RANS) as follows:

$$\frac{\partial \rho}{\partial t} + \frac{\partial}{\partial x_i}\left(\rho \overline{u}_i\right) = 0, \tag{5.4}$$

and,

$$\frac{\partial \rho \overline{u}_i}{\partial t} + \frac{\partial (\rho \overline{u_i u_j})}{\partial x_j} = -\frac{\partial \overline{p}}{\partial x_i} + \frac{\partial}{\partial x_j}\left[\mu\left(\frac{\partial \overline{u}_i}{\partial x_j} + \frac{\partial \overline{u}_j}{\partial x_i} - \frac{2}{3}\delta_{ij}\frac{\partial \overline{u}_l}{\partial x_l}\right)\right] + \frac{\partial}{\partial x_j}\left(-\rho \overline{u'_i u'_j}\right), \tag{5.5}$$

where ρ is the fluid density, $\overline{p}$ is the time averaged pressure and μ is the dynamic

viscosity of the fluid. The averaging process leads to the term $-\rho\overline{u_i' u_j'}$, the so-called Reynolds stress, involving products of averaged fluctuating velocity components whose relationship to the mean flow components is unknown. This is known as the closure problem. In order to close the system it is necessary to describe Reynolds stresses in terms of the known solution (mean flow). To obtain this relation, two types of turbulence or closure models exist:

- *Eddy Viscosity models* (EVM): In an eddy-viscosity model the Reynolds stresses are assumed to be proportional to the mean velocity gradients, with the constant of proportionality being the turbulent viscosity, μ_t. Then, the problem reduces to find the turbulent viscosity μ_t. This assumption is known as the *Boussinesq eddy viscosity* hypothesis and provides the following expression for the Reynolds stresses [87]:

$$\left(-\rho\overline{u_i' u_j'}\right) = \frac{2}{3}\rho k\delta_{ij} + \mu\left(\frac{\partial \overline{u}_i}{\partial x_j} + \frac{\partial \overline{u}_j}{\partial x_i}\right) + \frac{2}{3}\mu_t \frac{\partial \overline{u}_j}{\partial x_j}\delta_{ij}. \tag{5.6}$$

  Depending of the number of equation involved, EVM models are classified as:

  - Algebraic or Zero equation models: Mixing length model, Cebeci-Smith, Baldwin-Lomax...
  - One equation models: k model, Wolfstein, Baldwin-Barth, Spalart-Almaras...
  - Two equation models: Standard k-ϵ, Realizable k-ϵ, RNG k-ϵ, Standtard k-ω, SST k-ω...
  - Transition models: k - kl - ω transition model, Transition SST model...

- *Reynolds Transport Models (RSM)*: Solves directly the Reynolds stresses, also known as the seven equations model.

The great majority of computations at present, particularly those for industrial applications for complex-shaped configurations are computed by two equation eddy viscosity models, usually by way of supplementary transport equations that amount to representative length and time scales for the energy-containing turbulent motions.

Two equation eddy viscosity models (EVM)

Different eddy-viscosity models have been developed since the pioneering work of Launder and Spalding [114]. A description of the employed models is provided accounting for their transport equations based on the information available in Ansys theory guide [115].

The k - ϵ turbulence model

In eddy viscosity based $k-\epsilon$ turbulence models the velocity and length scales which characterize the turbulent field are obtained from two parameters: The turbulence kinetic energy, k and dissipation ϵ. The velocity scale is taken to be $\sqrt{k}$ and the length scale is taken to be $\sqrt{k^3}/\epsilon$. Therefore, the turbulent viscosity μ_t is computed by combining k and ϵ as:

$$\mu_t = \rho C_\mu \frac{k^2}{\epsilon}, \tag{5.7}$$

where k is the turbulence kinetic energy expressed as:

$$k = \frac{1}{2}\overline{u'}_i\overline{u'}_i. \tag{5.8}$$

The standard $k-\epsilon$ turbulence model initially developed by Launder and Spalding [116] is a semi-empirical model based on model transport equations for the turbulence kinetic energy k and its dissipation rate ϵ. The model transport equations for k is derived from the exact equation, while the model transport equation for ϵ is obtained using the physical reasoning and bears little resemblance to its mathematically exact counter-part. In the derivation of the $k-\epsilon$ turbulence model, it is assumed that the flow is highly turbulent, and the effects of the molecular viscosity are negligible. The turbulence kinetic energy k and its dissipation rate ϵ are obtained from the following transport equations given by Launder and Spalding [116]:

$$\frac{\partial}{\partial t}(\rho k) + \frac{\partial}{\partial x_i}(\rho \overline{u}_i k) = \frac{\partial}{\partial x_j}\left[\left(\mu + \frac{\mu_t}{\sigma_k}\right)\frac{\partial k}{\partial x_j}\right] + G_k - \rho\epsilon, \tag{5.9}$$

and,

$$\frac{\partial}{\partial t}(\rho \epsilon) + \frac{\partial}{\partial x_i}(\rho \overline{u}_i \epsilon) = \frac{\partial}{\partial x_j}\left[\left(\mu + \frac{\mu_t}{\sigma_\epsilon}\right)\frac{\partial \epsilon}{\partial x_j}\right] + C_{1\epsilon}\frac{\epsilon}{k}G_k - C_{2\epsilon}\rho\frac{\epsilon^2}{k}. \tag{5.10}$$

In these equations, G_k represents the generation of turbulence kinetic energy due to the mean velocity gradients, calculated as follows:

$$G_k = -\rho\overline{u'}_i\overline{u'}_j\frac{\partial \overline{u}_j}{\partial x_i}. \tag{5.11}$$

The coefficients $C_{1\epsilon}, C_{2\epsilon}, C_\mu, \sigma_k, \sigma_\epsilon$ are the constants. The corresponding default values for these coefficients are given as follows [114]:

$$C_{1\epsilon} = 1.44, C_{2\epsilon} = 1.92, C_\mu = 0.09, \sigma_k = 1.0, \sigma_\epsilon = 1.3. \tag{5.12}$$

These default values have been determined from experiments for fundamental tur-

bulent flows including frequently encountered shear flows like boundary layers, mixing layers and jets as well as for decaying isotropic grid turbulence (Chapter 4.1.2).

The RNG $k-\epsilon$ turbulence model

Yakhot and Orszag [117] have proposed another variant of the $k-\epsilon$ turbulence model where the performance characteristics are improved relative to the standard model. The RNG $k-\epsilon$ turbulence model is based on Renormalised Group theory. This model is similar in form to the standard $k-\epsilon$ turbulence model; however the RNG $k-\epsilon$ turbulence model differs from the standard model by the inclusion of an additional sink term in the turbulence dissipation equation to account for non-equilibrium strain rates and employs different values for the various model coefficients. The form of the k equation remains same. The turbulence dissipation equation of the RNG $k-\epsilon$ turbulence model includes the following sink term:

$$\frac{C_\mu \rho \eta^3 (1-\eta/\eta_0)}{1+\beta\eta^3}\frac{\epsilon^2}{k}, \tag{5.13}$$

where $\eta_0 = 4.38$ and $\beta = 0.012$. The above sink term also employs the parameter η, which is the ratio of characteristic time scales of turbulence and mean flow field as follows:

$$\eta = \frac{Sk}{\epsilon}, \tag{5.14}$$

where

$$S = \sqrt{2S_{ij}S_{ij}} = \sqrt{\frac{G_k}{\mu_t}}. \tag{5.15}$$

The models constants, except β (derived from experiment), have values derived analytically by the RNG theory. Recommended values for these model coefficients are given as follows:

$$C_{1\epsilon} = 1.44, C_{2\epsilon} = 1.68. \tag{5.16}$$

The Realizable $k-\epsilon$ turbulence model

The Realizable $k-\epsilon$ model [118] differs from the standard $k-\epsilon$ model in two important ways:

1. The realizable $k-\epsilon$ model contains an alternative formulation for the turbulent viscosity.
2. A modified transport equation for the dissipation rate ϵ, has been derived from an exact equation for the transport of the mean-square vorticity fluctuation.

The term realizable means that the model satisfies certain mathematical constraints on the Reynolds stresses, consistent with the physics of turbulent flows. The difference between the realizable and other $k-\epsilon$ models is that C_μ is no longer constant. It is

a function of the mean strain and rotation rates, the angular velocity of the system rotation, and the turbulence fields (k and ϵ). It is computed from

$$C_\mu = \frac{1}{A_0 + A_s \frac{kU^*}{\epsilon}}, \tag{5.17}$$

where $A_0 = 4.04$ and $A_s = \sqrt{6}\cos\phi$.
More specific details on this expressions can be found in Ansys theory guide [115]. The model constants $C_{1\epsilon}, C_{2\epsilon}, \sigma_k$ and σ_ϵ have been established to ensure that the model performs well for certain canonical flows. The model constants are

$$C_{1\epsilon} = 1.44, C_2 = 1.9, \sigma_k = 1.0, \sigma_\epsilon = 1.2. \tag{5.18}$$

Low-Re Chien $k-\epsilon$ turbulence model

There are hundreds of different low-Re $k-\epsilon$ models in the literature. A very common model in turbomachinery applications is the one developed by Chien [119]. Low-Re $k-\epsilon$ models were developed to improve the prediction of the behavior for k and ϵ near to the solid walls. The equations are integrated to the wall without assuming an universal law for the velocity profile and an equilibrium conditions for k and ϵ. In low-Re $k-\epsilon$ models, the turbulent viscosity μ_t the transport equations of standard $k-\epsilon$ model are modified using algebraic functions to damp certains terms:

$$\mu_t = \rho f_\mu C_\mu \frac{k^2}{\epsilon}, \tag{5.19}$$

$$\frac{\partial}{\partial t}(\rho k) + \frac{\partial}{\partial x_i}(\rho \overline{u}_i k) = \frac{\partial}{\partial x_j}\left[\left(\mu + \frac{\mu_t}{\sigma_k}\right)\frac{\partial k}{\partial x_j}\right] + G_k - \rho\epsilon - \rho D, \tag{5.20}$$

and,

$$\frac{\partial}{\partial t}(\rho \epsilon) + \frac{\partial}{\partial x_i}(\rho \overline{u}_i \epsilon) = \frac{\partial}{\partial x_j}\left[\left(\mu + \frac{\mu_t}{\sigma_\epsilon}\right)\frac{\partial \epsilon}{\partial x_j}\right] + C_{1\epsilon} f_1 \frac{\epsilon}{k} G_k - C_{2\epsilon} f_2 \rho \frac{\epsilon^2}{k} + \rho E. \tag{5.21}$$

where

$$f_1 = 1; f_2 = 1 - 0.22 e^{-\frac{{Re_t}^2}{6}}; f_\mu = 1 - e^{-0.0115 y^+}, \tag{5.22}$$

and,

$$D = 2\frac{\mu k}{\rho y^2}; E = 2\frac{\mu \epsilon}{\rho y^2} e^{-0.5 y^+}. \tag{5.23}$$

The damping functions f_1, f_2, f_μ and the extra source terms D and E are only active close to solid walls and makes it possible to solve $k-\epsilon$ down to the viscous sublayer.

The coefficients $C_{1\epsilon}, C_{2\epsilon}, C_\mu, \sigma_k, \sigma_\epsilon$ take the following values:

$$C_{1\epsilon} = 1.35, C_{2\epsilon} = 1.8, C_\mu = 0.09, \sigma_k = 1.0, \sigma_\epsilon = 1.3. \tag{5.24}$$

The standard $k-\omega$ turbulence model

The two-equation model by Wilcox [120] is an empirical model based on transport equations for the turbulence kinetic energy k and the specific dissipation rate ω, which is related to ϵ and k as follows:

$$\epsilon = \beta^* \omega k. \tag{5.25}$$

The turbulent viscosity μ_t is related to k and ω by:

$$\mu_t = \alpha^* \frac{\rho k}{\omega}. \tag{5.26}$$

The coefficient α^* damps the turbulent viscosity causing a low-Reynolds number correction. And the distribution of k and ω is calculated from the model transport equations

$$\frac{\partial}{\partial t}(\rho k) + \frac{\partial}{\partial x_i}(\rho \overline{u}_i k) = \frac{\partial}{\partial x_j}\left[\left(\mu + \frac{\mu_t}{\sigma_k}\right)\frac{\partial k}{\partial x_j}\right] + G_k - \beta^* \rho \omega k, \tag{5.27}$$

and,

$$\frac{\partial}{\partial t}(\rho \omega) + \frac{\partial}{\partial x_i}(\rho \overline{u}_i \omega) = \frac{\partial}{\partial x_j}\left[\left(\mu + \frac{\mu_t}{\sigma_\omega}\right)\frac{\partial \omega}{\partial x_j}\right] + \alpha \frac{\omega}{k} G_k - \beta \rho \omega^2. \tag{5.28}$$

In these equations, G_k is modeled identically as for the $k-\epsilon$ models. The rest of model constants are those specified by Wilcox [121] in the original version of the $k-\omega$ model.

The Shear Stress Transport (SST) $k-\omega$ turbulence model

The SST $k-\omega$ turbulence model previously developed by Menter [122] to effectively blend the robust and accurate formulation of the $k-\omega$ model in the near-wall region with the free-stream independence of the $k-\epsilon$ model in the far field. To achieve this, $k-\epsilon$ model is converted into a $k-\omega$ formulation with the inclusion of following refinements into the standard $k-\omega$ model:

1. The standard $k-\omega$ model and the transformed $k-\epsilon$ model are both multiplied by a blending function and both models are added together. The blending function is designed to be one in the near-wall region, which activates the standard $k-\omega$ model, and zero away from the surface, which activates the transformed $k-\epsilon$ model.

2. The SST model incorporates a damped cross-diffusion derivative term in the ω equation.

3. The definition of the turbulent viscosity is modified to account for the transport of

the turbulent shear stress.

4. The modelling constants are different.

These features make the SST $k-\omega$ model more accurate and reliable for adverse pressure gradient flows, airfoils and transonic shock waves, among others.

Modelling in the immediate wall vicinity

The turbulence models considered in earlier chapter were based on the assumption that the turbulent Reynolds numbers were high enough everywhere to permit the neglect of viscous effects. Thus, they are not applicable to flows with a low Reynolds number or to the viscosity-affected regions adjacent to solid walls. In other words, while at high Reynolds number viscous effects on the energy-containing turbulent motions are indeed negligible throughout most of the flow, the condition of no-slip at solid interfaces always ensure that, in the immediate vicinity of a wall, viscous contributions will be influential, perhaps dominant. This viscosity-affected zone is named as the boundary layer. The boundary layer allows the fluid to transition from the free stream velocity U_0 to a velocity of zero at the wall. Its thickness δ is defined as the distance away from the surface where the velocity reaches 99 % of the free-stream velocity. Although the thickness of the boundary layer is usually two or more orders of magnitude less than the overall with of flow, its effects extend over the whole flow field since, typically, half of the velocity change from the wall to the free stream occurs in this region. Figure 5.2 shows the schema of the boundary layer and the different regions that comprised it.

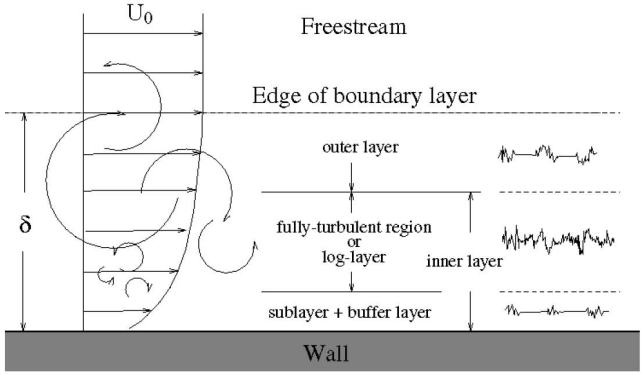

Figure 5.2: Different regions at turbulent boundary layer

In fully developed turbulence conditions, the boundary layer is divided in three sub-regions; the viscous sublayer, the log-law region and the outer layer. The two first layers establish the inner layer. In the following subsections further analysis in these regions is provided.

Subdivisions of near-wall regions

To differentiate each of regions the adimensional parameter y^+ is utilized, that is defined as:

$$y^+ = \frac{\rho u_\tau y}{\mu}, \tag{5.29}$$

where u_τ is the so-called friction velocity that is determined as:

$$u_\tau = \sqrt{\frac{\tau_w}{\rho}}. \tag{5.30}$$

Close to the wall the flow is influenced by viscous effects and does not depend on free stream parameters. The mean flow velocity U only depends on the distance y from the wall, fluid density ρ, the viscosity μ, and the wall shear stress τ_w.

$$U = f(y, \rho, \mu, \tau_w). \tag{5.31}$$

The friction velocity u_τ can be used to adimensonalize the velocity. Dimensional analysis shows that:

$$u^+ = \frac{U}{u_\tau = f\left(\frac{\rho u_\tau y}{\mu}\right)} = f(y^+). \tag{5.32}$$

The Equation (5.32) is recognized as the law of the wall and contains the definitions of the two important dimensionless groups u^+ and y^+. The law of the wall can vary depending on the subdivision of the near wall region that is considered. A schema of the different regions and the law of the wall involved in each region is provided in Figure 5.3.

Viscous sublayer

This layer is extremely smooth, being limited by the condition $y^+<5$. In this sublayer, viscous effects predominate over the inertial effects, so it underlies a laminar behavior. Thereby the wall shear stress is constant and corresponds to the value at the wall.

$$\tau(y) = \mu \frac{\partial u}{\partial y} \cong \tau_w. \tag{5.33}$$

Integrating and using the equations 6.3, 5.30 and 5.32 it is obtained that:

$$u^+ = y^+. \tag{5.34}$$

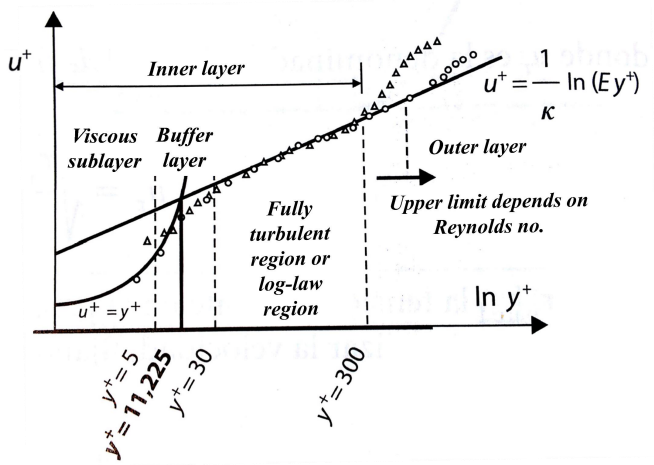

Figure 5.3: Boundary layer regions (adapted from Oro [23])

Log-law layer or fully turbulent region

This layer is developed in the interval between $30 < y^+ < 300$. At lower limit there is a transition between viscous and log-law layer, called buffer layer, which delimits the laminar and fully turbulent flow. It is usual to set an intermediate value of y^+=11.225 in order to establish a limit between two zones. Moreover, this limit coincides with the intersection between the linear law $u^+ = y^+$ and the log-law that adjusts to this zone:

$$u^+ = \frac{1}{K} \ln(Ey^+), \tag{5.35}$$

where $K = 0.41$ and E=9.793 are the *Von Karman* constants. In this layer the Reynolds stresses predominate over the viscous stress.

Outer layer

This layer is developed from y^+>300 or 500, that normally corresponds to zone between the 20 % and the final of the boundary layer. In this region the inertial effects of the central zone of the flow dominate over the viscous effects in the near wall region.

Near-wall treatment

The complex flow structures in the near wall region imply a serious challenge for any type of turbulence model. The turbulence length scales in the solid wall boundaries are so small that the number of cells rises significantly. Thus, the strategy of modelling the whole boundary layer seems to be the best option. Using the experimental formulation that governs the structure of the boundary layer, different mathematical models are developed to produce the boundary conditions for the near wall cells of the turbulent flow. This way, the conditions for all the transport equations to be resolved are introduced.

Generally, two approaches are differentiated (Figure 5.4):

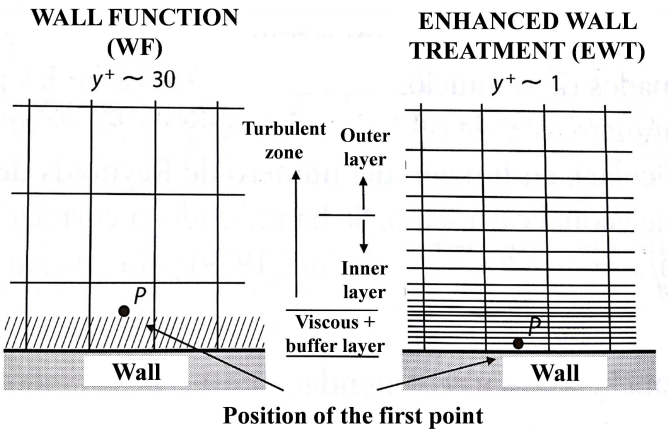

Figure 5.4: Near-wall treatments as a function of the mesh density (adapted from Oro [23])

Wall Functions (WF):

They are based in log-law (Equation (5.35)) of the fully turbulent region and it is valid in the range $30<y^+<300$. In this case the mesh must be relatively coarse, as its application is correct for $y^+>11.225$. When the mesh is such that $y^+<11.225$ at the wall-adjacent cells, it applies the laminar stress-strain relationship (Equation (5.34)).

Enhanced Wall treatment (EWT):

Also known as two layer model, it is defined as a near wall model which resolves the entire distribution of the velocity in the inner layer until the viscous sub-layer. The all domain is devised in two regions and combines the resolution of the viscosity-affected laminar region and the fully-turbulent region. The demarcation of the two regions is determined by a wall-distance-based, turbulent Reynolds number Re_y defined as:

$$Re_y = \frac{\rho y \sqrt{k}}{\mu}. \tag{5.36}$$

For applying this option it is essential to have a very fine mesh, in the order of $y^+ \approx 1$, which requires at least 10 to 15 cells in the viscous sublayer.

5.1.2 Large-Eddy Simulation (LES)

The LES method is half way between the direct solution (DNS) and the RANS methods. By not resolving the smallest scales the spatial resolution of the mesh and the time resolution of the calculation are not that high as for the DNS. The scales that are below the mesh size are modeled by SGS (Sub-Grid Scale). To carry out the computation of the turbulent flow, continuity Equation (5.1) and and Navier-Stokes Equation (5.2) are filtered as described below:

$$\frac{\partial \rho}{\partial t} + \frac{\partial \rho \hat{u}_i}{\partial x_i} = 0, \tag{5.37}$$

and,

$$\frac{\partial}{\partial t}(\rho \hat{u}_i) + \frac{\partial}{\partial x_j}(\rho \hat{u}_i \hat{u}_j) = -\frac{\partial \hat{p}}{\partial x_i} + \frac{\partial}{\partial x_j}\left[\mu\left(\frac{\partial \hat{u}_i}{\partial x_j} + \frac{\partial \hat{u}_j}{\partial x_i} - \tau_{ij}\right)\right] \tag{5.38}$$

where ρ is the fluid density, μ is the dynamic viscosity of the fluid, $\hat{u}_i$ is the filtered value of the velocity, $\hat{p}$ is the filtered value of the pressure, and τ_{ij} is the sub-grid scale stress, defined as:

$$\tau_{ij} = \widehat{u_i u_j} - \hat{u}_i \hat{u}_j \tag{5.39}$$

To close the filtered equations the sub-grid scale stress is modeled using a viscous analogy based on the Boussinesq hypothesis (Equation 5.6) [87], which consists on expressing the sub-grid scale stress τ_{ij} in terms of μ_t, the sub-grid scale viscosity. This procedure is the same that is employed in Eddy Viscosity models for the closure problem in RANS simulations (Section 5.1.1).

Sub-grid scale (SGS) models

The modelling of the sub-grid scale stress $\tau_i j$ is relatively simple, because it accounts for the effect of small scales over the transport equations and these scales are, in principle, isotropic. Most of SGS models are based on the hypothesis that the fluctuations are isotropic and determined by the gradients of the filtered fluctuations through the artificial sub-grid scale viscosity μ_t. These gradients are named *mean strain rate tensor* and they are defined as:

$$\hat{S}_{ij} = \frac{1}{2}\left(\frac{\partial \hat{u}_i}{\partial \hat{x}_j} + \frac{\partial \hat{u}_j}{\partial \hat{x}_i}\right) \tag{5.40}$$

Next, the most employed sub-grid scale (SGS) models are presented:

The Smagorinsky-Lilly model

This algebraic simple (zero equations) model does not require the resolution of any additional transport equation. It was first proposed by Smagorinsky [123] and Lilly [124] and it resolves the SGS stresses τ_{ij} from the filtered variables calculated by Equation (5.40) using the following formulation:

$$\tau_{ij} = -2\mu_t \hat{S}_{ij} + \frac{2}{3} k_{SGS} \delta_{ij}, \tag{5.41}$$

where k_{SGS} is the sub-grid scale kinetic energy, and μ_t is the sub-grid scale viscosity term calculated by the Smagorinsky model given as:

$$\mu_t = \rho l^2 \left(2\hat{S}_{ij}\hat{S}_{ij}\right)^{1/2}, \tag{5.42}$$

with l is the characteristic sub-grid length scale, which is related to the width of the filter Δ used as

$$l = C_s \Delta. \tag{5.43}$$

C_s is the Smagorinsky constant calculated from the inertial subrange of the energy spectrum given by the Kolmogorov's $-5/3$ law (Section 4.1.1.3) and it is chosen in a range from 0.10 to 0.30. The second term Δ is the filter width, an indication of the characteristic length scale separates large and small-scale eddies from each other and can considered to be an average cell size. It is calculated as

$$\Delta = (\Delta x \Delta y \Delta z)^{1/3}. \tag{5.44}$$

Therefore, the sub-grid length is calculated directly from the local grid size and the grid size distribution is thus very important for the present subgrid scale (SGS) model. The Smagorinsky-Lilly model is based on the local equilibrium at the sub-grid scale (turbulent kinetic energy transport is not allowed). What is more, there is not a universal C_s value, it depends on the flow type, and can present problems reproducing transitional flows and wall effects. To address these limitations several SGS models are available in literature.

The Wall-Adapting Local Eddy-Viscosity (WALE) model

This model is a modification of Smagorinsky-Lilly model that takes into account the flow structures near the wall. It improves the artificial viscosity in the walls, but still do not resolve the non-equilibrium problems neither the transport of turbulence in sub-grid

scales.

The Dynamic Smagorinsky-Lilly model

Also known as Dynamic Sub-Grid Scale (DSGS), it was proposed by Germano [125], it is a modification of Smagorinsky-Lilly model that provides a dynamic calculus of the C_s constant, overcoming the problems of reproducing transitional flows and wall effects. The constant is calculated locally in time through a two phase filter in predictor-corrector mode.

The problem of near-wall treatment: Hybrid Techniques

In the near wall region, the requirements of LES for solving the 80 % of the turbulent kinetic energy are very restrictive due to the boundary layer flow structure. The complexity sources from the necessity of having an extremely high mesh density ($x^+ \approx 50-150$, $y^+ < 1$, $z^+ \approx 15-40$), being x the flow direction, y the distance from the wall and z the width) able to describe the dynamics of eddies down to the inner layer. These requirements rises the computational cost of LES to the order of DNS, and it can only be resolved for low or moderate Reynolds numbers through supercomputers. These types of simulations are called WRLES or LES-NWR (Wall-Resolved or Near-Wall Resolved). In practice, it is advisable, in terms of computational cost and precision, to introduce a wall model in the LES simulation. Several possibilities exist:

Wall-modeled LES (WMLES)

In this case a wall model is implemented based on the wall treatment that is done in RANS simulations (Wall Functions in Section 5.1.1), where the boundary layer is modeled by an established log-law (Equation 5.35). In this case, values of y^+>11.225 are adopted with the consequent computational save.

Detached Eddy Simulation (DES)

The next step is to solve the totality of the boundary layer (inner and outer region) through a RANS model (usually Spalart-Allmaras) coupling it with LES filtered equations. The change between two zones is precised by the grid dimension. Thereby, the conventional RANS turbulence model in the RANS zone turns into a SGS model in LES zone through a simple mathematic conversion:

$$\widetilde{d} = \min[d, C_{DES} \cdot \Delta], \tag{5.45}$$

where d is the distance to the wall and $C_{DES} \cdot \Delta$ establishes the reference value in Equation (5.44) for applying SGS model. This way, near the wall (d«Δ) one obtains that $d = \widetilde{d}$ (RANS), and far from the wall ($C_{DES} \cdot \Delta$<d), one obtains that $\widetilde{d} = C_{DES} \cdot \Delta$ (LES).

These techniques are known as Hybrid, and join the advantages of RANS to solve the smooth boundary layers and of LES to solve flow separated regions, highly vortical and turbulent. The main problem of these techniques is to define a good initial mesh that achieves to differentiate RANS and LES zone where it is interesting (in the border of the boundary layer).

5.2 Experimental study

In this study a small opened wind tunnel, initially built at the Department of Physics of the Ecole Normale Supérieure in Paris for undergraduate laboratory Courses (now moved to *Laboratoire des Écoulements Géophysiques et Industriels*, LEGI, in Grenoble) is used for the experimental measurements. The results in this study serve to validate the numerical simulations performed.

The wind tunnel employed is fully described in Mordant [100], it is about 4 m long with a cross section of 25×25 cm^2. It is composed of several sections made of 1 cm thick plywood. Four 37 W fans (EBMPAPST model DV6224) blow the air into the tunnel. Upstream the test section an 8 cm thick honeycomb is used to damp the vortices generated by the fans. After this section, the flow is relatively homogeneous with natural fluctuations below 2 % of the mean velocity, which can reach 7.5 m/s at the full speed of the fans. The grid is located at the entrance of the test section, just downstream of the honeycomb. Air then flows through the grid system followed by a 2 m test section with a free exit.

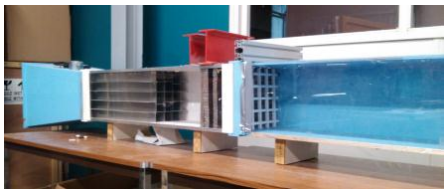

Figure 5.5: Low-speed wind tunnel

The passive grid has a mesh spacing of $M = 0.05$ m and given the length of the test section, which is 2 m, a maximum of 40 mesh numbers ($x/M = 40$) are reached in the streamwise direction for the measurement of the decay of turbulence. In this experiment a flow turbulence with Reynolds number of order 100 (based on Taylor microscale) is obtained downstream a passive grid.

Measurements are performed using a single wire probe model 55P11 coupled to a CTA 90C10 module from Dantec Measurement Technology company. A commercial autocalibrated velocity transducer model 8455 from TSI company is positioned next to

the hot wire to give a reference measurement of the average longitudinal flow velocity used for the calibration of the hot wire. It should be noted here that in open flows with a large mean velocity U compared to fluctuations u' (as it is the case in grid turbulence) the time series of velocity recorded by the hot wire in a fixed point can be related to the streamwise spatial fluctuations of the velocity field (in the moving frame at the velocity U) using a frozen field Taylor hypothesis, with the space-time correspondance $x = Ut$. Such a Taylor hypothesis is used to calculate spatial correlation functions of the velocity field, from which the integral scale of turbulence is extracted.

Different variables are obtained, such as velocity profiles, velocity fluctuations, decay of the turbulence kinetic energy and the growth of the length scales. These results are then compared with the typical values obtained in literature for assessing its reliability, showing that it is consistent with other studies with an exponent decay in the range n=1.15-1.45 (depending on the choice of the virtual origin). The evolution of the streamwise component of the velocity along the central line of the tunnel is obtained in order to compare with the numerical data (see Figure 5.6).

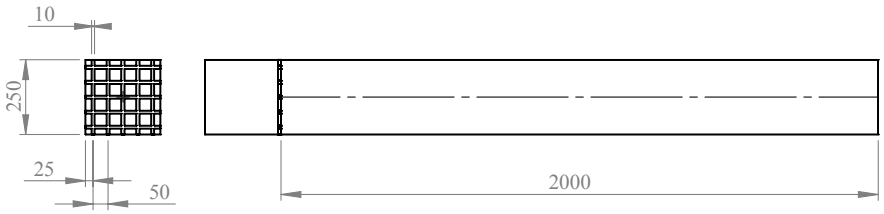

Figure 5.6: Central line for extracting experimental data (units in mm)

More detailed information on the experimental measurements is available in Torrano *et al.* [126]. The experiments in this study can be resumed by simply noting that the experiment produces a canonical and well behaved decaying turbulence, with standard power law decaying profiles. The energy dissipation rate, and all the relevant turbulent scales are estimated based on measurements of the decay of turbulence kinetic energy. On the other hand, the energy injection scale is determined from the velocity correlations, which was found to be related to the turbulent dissipation according to the usual scaling $\epsilon = Du_{rms}^3/L$. The dimensionless constant D tends toward a constant plateau of the order of 0.7-0.8 in the well developed region, consistent with the numerical data from various DNS simulations of homogeneous and isotropic turbulence collected by [127] and giving an estimate of D between 0.5 and 1 for the range of Reynolds number investigated.

5.3 RANS modelling

In spite of the popularity of passive grids as turbulence generators, their design relies essentially on empirical laws. It is proposed here to test the ability of simple numerical simulations to capture the large scale properties (rms velocity, turbulence decay, pressure drop, etc) of the turbulence downstream a passive grid.

The accuracy of several RANS-based turbulence models is tested. With this purpose, a simulation plan is performed to study first the mesh dependency, and second, the influence of the different two equations eddy viscosity models and variables involved in their transport equations.

5.3.1 Computational domain and boundary conditions

The flow domain of the test section with the grid inside are initially reproduced with a CAD program. After importing the geometry to the fluid flow solver environment, several computational meshes are created in order to discretize the governing flow equations in the computational domain. Different meshing strategies are performed for analyzing the sensitivity of the model. Cut-cell assembly method is employed in all meshes for a faster convergence and stability for flow simulations. This mesh method generates a high percentage of hexahedral cells in a Cartesian layout in the far field, to deliver accurate fluid flow results. They generated meshes also checked and revised for its skewness and aspect ratio criteria. Details of each mesh are given in Table 5.1.

Table 5.1: Simulation plan for the mesh sensitivity analysis

Case	Turbulence model	Wall treatment	Number of cells	Parametric test
1	Standard $k-\epsilon$	Standard WF	2500000	Mesh Sensitivity
2		Enhanced WT	3350000	
3		Standard WF	8985600	

Mesh 1 and 2 consist of 4 mm size elements in the whole computational domain with the only difference in the vicinity of the grid and exterior walls. The surface cells can be inflated to generate hexahedral and prismatic layers (inflation layers) to capture near-wall physics effects. Mesh 2 employs finer mesh of 0.1 mm which is comprised of 5 inflation layers that provide a suitable wall y plus value for utilizing the Enhanced Wall Treatment. This near-wall modelling method resolves the viscosity-affected near-wall region all the way to the viscous sublayer, if the near-wall mesh is fine enough to capture the laminar sublayer (typically $y^+ \approx 1$). This procedure leads to higher number of mesh cells than Mesh 1. Regarding the Mesh 3, a smaller mesh density in the whole domain

is employed with elements of 2.5 mm.

Having completed the mesh domains, required inflow and outflow boundary conditions are imposed. At the inlet boundary, a uniform velocity of 5 m/s is imposed while free outflow boundary conditions are used at the outlet as a fully developed velocity profile is expected. For setting the turbulent parameters at the inlet, it is known from experiments that the turbulence intensity at the wind tunnel entry is 2 %. It is also known that the integral length scale in grid-generated turbulence can be assumed to be equal to the mesh spacing $M = 0.05$ m, so the values of k and ϵ are defined based on these parameters. No slip condition is imposed at the wall surfaces in the test section and grid walls.

5.3.2 Solver method and turbulence modelling

A finite volume method is used for solving the incompressible Navier-Stokes equations with steady state assumptions. The SIMPLE (Semi-Implicit Method for Pressure Linked Equations) pressure velocity-coupling scheme based on the high degree of approximate relation between pressure and velocity is used for the present numerical solver. For a choice of best suitable turbulence modelling approach, a parametric study of an analysis of turbulence modelling effects is performed. The different simulations performed are summarized in Table 5.2. All the models are set up with the default constants values defined in Section 5.1.1.

Table 5.2: Simulation plan for the turbulence modelling effect

Case	Turbulence model	Mesh	Parametric test
4	RNG $k-\epsilon$		
5	Standard $k-\omega$		
6	SST $k-\omega$	Mesh 3	modelling effect
7	Low-Re Chen RNG $k-\epsilon$		
8	Realizable $k-\epsilon$		

The standard values of these constants represent a compromise to give the best performance for a range of canonical flows, such as decaying homogeneous isotropic turbulence (which is the subject of study here), homogeneous shear flow and the logarithmic layer. Specifically, $C_{2\epsilon}$ value is built to be consistent with the power-law decay observed in grid turbulence [20];

$$C_{2\epsilon} = \frac{n+1}{n}, \tag{5.46}$$

where n is the decay exponent.

Another condition sources from the homogeneous shear turbulence, which establishes the ratio between turbulence kinetic energy production P and dissipation ϵ as;

$$\frac{P}{\epsilon} = \frac{C_{2\epsilon} - 1}{C_{1\epsilon} - 1}. \tag{5.47}$$

The difference $(C_{2\epsilon} - C_{1\epsilon})$ determines the balance of production and removal terms in the closure equations (Equation (5.10)) and hence the length scale. To ensure that the model equations reproduce well the constant-stress logarithmic velocity law in the near wall region, the constants should satisfy the following condition:

$$\sigma_\epsilon = \frac{\kappa^2}{C_\mu^{1/2}(C_{2\epsilon} - C_{1\epsilon})}. \tag{5.48}$$

In this condition σ_ϵ is the effective Prandtl number for transport of the turbulent dissipation rate, which defines the ratio of the momentum diffusivity to the diffusivity of turbulence dissipation via turbulent transport. κ is the Von Karman constant that describes the logarithmic velocity profile of a turbulent fluid flow near a boundary with a no-slip condition. This constant is obtained through the boundary layer experiment and is considered to correspond to a universal value of $\kappa \approx 0.41$.

Any of the cited turbulence models is subjected to modifications due to the fact the model constants do not represent an adequate reconstruction of the ratio between the production and dissipation of the turbulence kinetic energy [128]. Then, the accuracy of the model calculations can be improved by adjusting these parameters to obtain agreement with experimental data, as suggested by Kantha [129]. In this study several modifications are proposed in accordance to the previously obtained experimental data of decaying turbulence. The computations are performed through the standard $k-\epsilon$ turbulence model due its simplicity for modifying the default constants. Table 5.3 shows the different values employed. First, Cases 9-12 are modified according to Equation (5.46) and the $C_{2\epsilon}$ value is then set to 1.75, which corresponds to the decay exponent measured of $n = 1.33$. The difference $(C_{2\epsilon} - C_{1\epsilon})$ is also investigated with reference to Equation (5.47) as the ratio P/ϵ decreases towards unity. Finally, the σ_ϵ value is tuned in order to maintain a realistic value of $\kappa \approx 0.41$.

5.3.3 Numerical results and discussion

The numerical results obtained from all cases (Cases 1-12) are presented in both qualitative and quantitative manner in comparison with the experimental data obtained under

Table 5.3: Simulation plan for modelling effect of constants modification

Case	Turbulence model	$C_{1\epsilon}$	$C_{2\epsilon}$	σ_ϵ	Parametric test
9	Standard $k-\epsilon$	1.44	1.75	2.0	Constants modification
10		1.55	1.75	3.1	
11		1.60	1.75	4.1	
12		1.65	1.75	6.0	

the same flow conditions. Figures 5.7-5.9 represent the predicted decay of turbulence kinetic energy as a function of the model length for different mesh densities, turbulence models and model constants. It is generally seen from these figures that the simulations are roughly consistent with the experimental data. Both numerical results and the experimental data reproduce similar tendency of loss of kinetic energy except more pronounced kinetic energy values obtained from the numerical simulations.

The comparative study of results obtained from different mesh densities are initially represented in Figure 5.7 to demonstrate the effect of mesh resolution on the results together with the treatment of near wall layer with different wall functions.

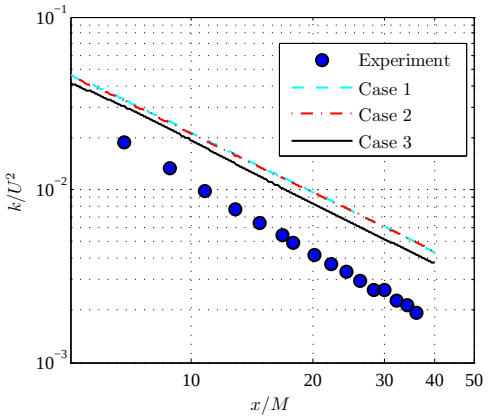

Figure 5.7: Turbulence kinetic energy decay for mesh sensitivity analysis

Taking into account the results obtained from Case 1 and Case 2, it is seen that there is no significant difference in using the Enhanced Wall Treatment and the required inflation layers, so the mesh of Case 3 is used for the subsequent simulations, due to its better correspondence with the experimental data.

Figure 5.8 then represents graphically the decay of turbulence kinetic energy for different turbulence models defined in Table 5.2.

For almost all cases, although the experimental power law decay is reasonably well recovered, the overall energy level is overestimated in the simulations. Cases 3, 6 and

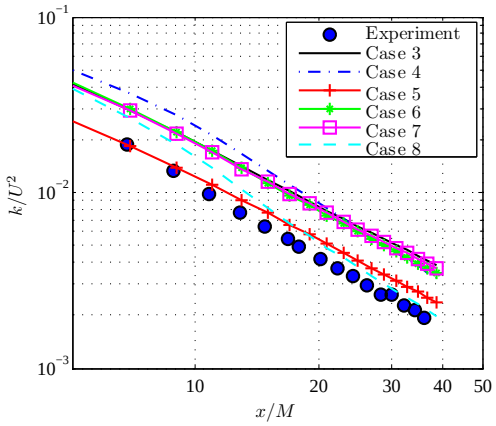

Figure 5.8: Turbulence kinetic energy decay for turbulence modelling effect

7, which correspond to Standard $k-\epsilon$, SST $k-\omega$ and Low Re RNG $k-\epsilon$ turbulence models, respectively, show a very similar tendency, and Case 4, which is the RNG $k-\epsilon$ model still gets a higher over-prediction of k in the near field region.

However, the results of Case 5 and Case 8 are found to be in better agreement with the experimental data. Specifically, Case 8 reproduces better far-field solution as Realizable $k-\epsilon$ includes a modified transport equation for the dissipation rate ϵ that has been derived from an exact equation for the transport of the mean-square vorticity fluctuations. It is noteworthy here that the k equation (Equation (5.9)) is the same as that in the standard $k-\epsilon$ and the RNG $k-\epsilon$ model, except for the model constants. However, the form of the ϵ equation is quite different from those in the standard and RNG-based $k-\epsilon$ models. One of the noteworthy features is that the production term in ϵ equation (the second term on the right-hand side of Equation (5.10)) does not involve the production of k, i.e., it does not contain the same G_k term as the other $k-\epsilon$ models. It is believed that the present form better represents the spectral energy transfer. On the other hand, Case 5 reproduces similar values in a near-field region (production zone) compared to experimental results. The $k-\omega$ model provides a better mechanism for predicting turbulence anisotropic effects at $x/M<20$, where the flow is affected by swirling effects.

The application of two-equation models in their initial form to grid generated turbulence leads to an overestimation ok k, and thus, requires improvement. The main explanation for this behavior may be in the P/ϵ ratio given by the model constants that are used by default in this models and cause an excessive production rate of k in the near wall region. For example, the P/ϵ ratio obtained in standard $k-\epsilon$ model (Case 3) for the default constants values of $C_{1\epsilon}$=1.44 and $C_{2\epsilon}$=1.92 is $P/\epsilon = 2.1$, which is a considerably higher value than the observed in experiments and DNS. Moreover, the $C_{2\epsilon}$=1.92 lies somewhat outside of the experimentally observed range. In order to evaluate the

influence of modifying the default parameters, Figure 5.9 shows the resulting evolution of k for the modifications proposed in Table 5.3.

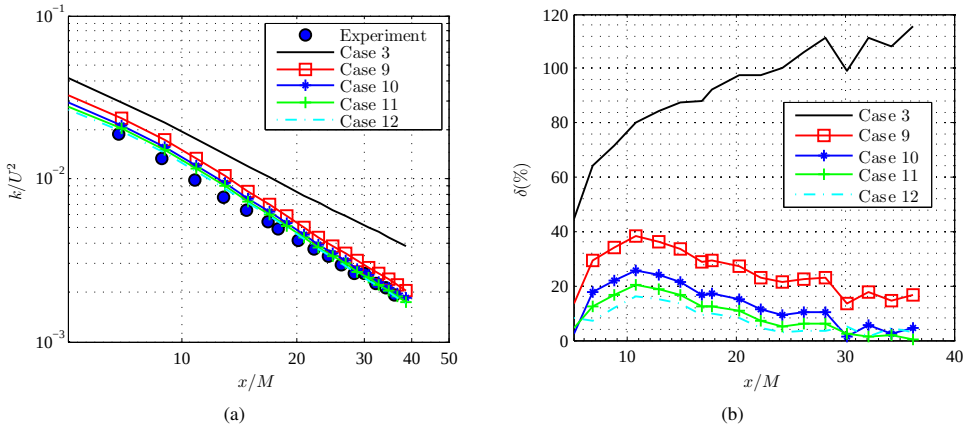

Figure 5.9: The downstream evolution of turbulence flow parameters; (a) Turbulence kinetic energy decay for modelling effect of the constants modification. (b) Relative error

The slopes in the profile of the turbulence kinetic energy for Cases 9-12 are parallel, corresponding to the $C_{2\epsilon}$ value employed. A good agreement with experimental data is achieved in the decaying zone ($x/M < 20$), once the inhomogeneities have vanished. The relative error in this zone $\delta = |k_{simulation} - k_{experiment}|/k_{experiment}$ is below 10 % for cases 10-12. This result might be expected beforehand due to the fact that in this zone there is no production of kinetic energy and the models' solutions have been built to be consistent with a power-law decay (Equation (5.46)). On the other hand, the over-predictions (relative error up to 40 %) of k is still a problem as in Case 9, because the difference ($C_{2\epsilon}$ - $C_{1\epsilon}$) predicts a high value of P/ϵ=1.7. In the subsequent Cases 10-12 it is observed how increasing the $C_{1\epsilon}$ value leads to better predictions, as the difference ($C_{2\epsilon}$ - $C_{1\epsilon}$) decreases and therefore so does the resulting P/ϵ ratio. It is also noteworthy that the effect of increasing $C_{1\epsilon}$ has slightly less influence on the decay profiles of turbulence kinetic energy as Case 11 and Case 12 both behaves in a very similar way. The limit for modifying the $C_{1\epsilon}$ is up to values of almost equal to $C_{2\epsilon}$ that will reproduce P/ϵ ratios closed to unity, which is the equilibrium state.

Rising the $C_{1\epsilon}$ value not only affects the turbulence kinetic energy decay, but also has a significant effect on the pressure coefficient C_p, as it is demonstrated in Figure 5.10.

The pressure coefficient C_p can be defined as the dimensionless normalized static pressure drop as:

$$C_p = \frac{\Delta p(x)}{\frac{1}{2}\rho U^2}, \tag{5.49}$$

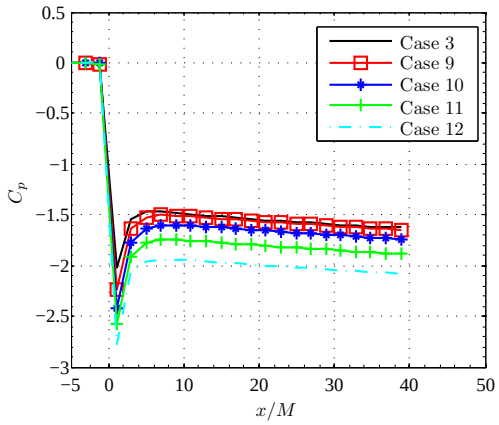

Figure 5.10: Pressure coefficient evolution for the modelling effect of the constants modification

with $\Delta p(x) = p(x) - p_0$ being the difference between the downstream static pressure at a position x and the pressure just upstream the grid.

It is observed how the C_p values are highly affected by the constant values. While gradually increasing the $C_{1\epsilon}$ in Cases 9-12, the static pressure drop through the grid increases. In the work done by Hurst [104] the experimental measurement of the pressure drop for a similar grid of 44 % of solidity and dimensions of T/M=6 (with T being equal to the test section size and M the mesh size of the grid) is provided and takes values around $C_p \approx 3.5$. On the other hand, in the reference handbook published by Corrsin [130], the evolution of C_p values for classic squared bars as a function of the solidity ranging from values of 35 % to 60 % is given for a grid of size T/M=20-40. In order to get a rough estimation of the C_p value, the data obtained by Hurst [104] is taken and extrapolated by employing the function supplied by Corrsin [130], what leads roughly to a pressure drop of $C_p \approx 2 - 2.5$ for the grid employed in this work, with a dimension of T/M=5 and a solidity of 36 %. Taking this value as a reference, it can be concluded that Case 12 reproduce better predictions according to the value obtained in Figure 5.9. Thus, the difference $(C_{2\epsilon} - C_{1\epsilon})$ plays a significant role not only in the decay of k, but also in predicting the pressure drag of the grid, and by modifying the constants in a proper manner it is possible to make a reliable prediction of the behavior of the turbulence generating grids. The RANS-based turbulence models, hence, become a useful tool for designing such grids.

In order to close the discussion of the numerical results, the qualitative comparison of the cases discussed is analyzed. Figure 5.11 shows the contour plot for turbulence kinetic energy obtained for the mid-plane along the streamwise direction. Different patterns are observed in the distribution of the kinetic energy contours. It is noticed that the higher magnitude of turbulence kinetic energy is obtained from Case 3, of the Standard $k - \epsilon$,

while lowest magnitude is obtained from both Case 4 and Case 8, where modifications of standard $k-\epsilon$ model are performed, the RNG $k-\epsilon$ and the Realizable $k-\epsilon$, respectively. Thus, the modifications made in the transport equations of $k-\epsilon$ models severely affect the turbulent flow properties. Regarding Case 5, where the $k-\omega$ turbulence model is employed, a high magnitude turbulence kinetic energy zone is observed in the frontal face. This zone is non-existent in Case 6 where the SST $k-\omega$ is employed. It is also noticeable that the contour plot of the low Re number turbulence model used in Case 7 is qualitatively very similar to that of Case 3. This is due to the fact that both models employ the same standard $k-\epsilon$ transport equations and the damping functions of the low Re number turbulence model are only applied to the near wall regions. Thus, the turbulence kinetic energy rise observed in the Case of the standard $k-\epsilon$ model just downstream of the grid is slightly lower than the one observed in Case 7, as a result of the developed boundary layer calculated by low Re number model. Similarities in the flow field between Case 5 and Case 8 are also noticeable, where the lower turbulence kinetic energy regions (blue zones) in the production range of the turbulence kinetic energy has almost the same lengths. Regarding Cases 9-12, it is observed how the values of k contours downstream of the grid are progressively reduced. In contrast, there is a growth in k contours in the zone located immediately before the grid. This effect becomes significant for Case 12, where the red colored zone is clearly visible, as occurred in Case 5.

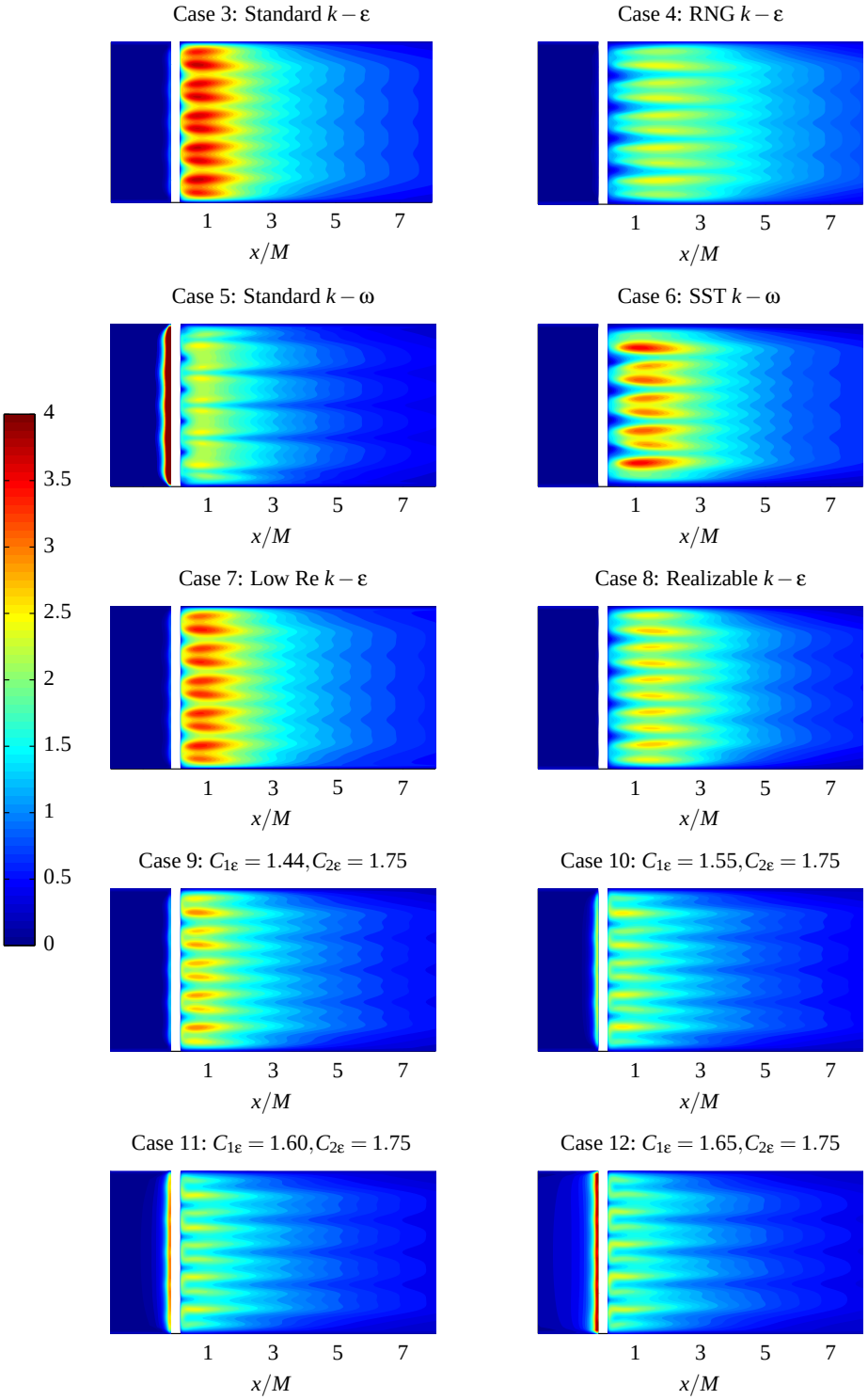

Figure 5.11: Turbulence kinetic energy (m^2/s^2) contour plots obtained for different turbulence models

5.4 Conclusions

In this chapter the accuracy of several RANS-based turbulence models to capture the large scale properties (rms velocity, turbulence intensity, turbulence decay and pressure drop) of the turbulence downstream a passive grid is tested.

Regarding the results obtained from mesh sensitivity analysis, it is seen that there is no significant difference in using the enhanced wall treatment for the current grid topology.

Among the different turbulence models applied, the results show that Standard $k-\omega$ model can successfully reproduce the production of turbulence kinetic energy in the near-field region, while Realizable $k-\epsilon$ model provides a better correlation in the far-field region.

The modification of the default constant values in two equation models can be considered to optimize the agreement with the experimental results, provided that the relations between the different parameters must be within a limited range in order to reproduce realistic behaviour of the turbulence model.

RANS-based turbulence model simulations are within an acceptable accuracy when compared to the experimental data (relative error below 10 % for the decaying zone), in spite of modelling all the energy spectrum. Therefore, it is demonstrated that RANS solutions can be used to study the influence of the grid design parameters on the decay of grid-generated turbulence.

Chapter 6

Airfoil simulations in turbulent inflow conditions

As noted in previous chapters, inflow turbulence affects the performance of devices operating in the atmospheric boundary layer. For instance, wind turbines placed in a wind farm can experience high intensities, specially when they are located in the wake of other wind turbines. In order to increase the efficiency of these devices, it is necessary to understand how the inflow turbulent characteristics affect drag and lift loads, flow separation and wake dissipation.

While inflow turbulence effect has frequently been investigated in wind tunnel experiments by the use of grids, it has not received much attention from the CFD community. The treatment of inlet conditions is a complex problem, but of extreme importance as, in many cases, the fluid behavior within the domain is determined in large part by the inlet behavior. Inflow conditions specified at the inlet boundary should ideally represent the contributions of energy-carrying eddies. Since the transport of momentum to the inner region of the boundary layer is caused by the eddies from the free flow entering and mixing the flow in the boundary layer, these eddies should be resolved to reproduce the desired mixing. Therefore, a turbulence resolving technique such as LES must be used to predict the effect of inflow turbulence.

In spite of its importance, there does not appear to be a consistent standard practice for dealing with inflow turbulence in LES. Several methods reported in the literature are classified as *precursor simulation* methods and *synthesized* methods. The main drawback of synthetic inlets is that turbulence kinetic energy is quickly dissipated and precursor simulation methods have a high computational cost, as they usually require running a separate simulation.

This chapter is then motivated by the need to produce a reliable and cost effective

solution to generate turbulent inflow conditions for its use in airfoil simulations at low Re numbers. Similar to wind tunnel experiments, a passive grid-generated turbulence technique is developed to produce inflow conditions in LES. The final aim is to use the proposed technique in an airfoil simulation to numerically investigate the effect of turbulent inflow conditions.

The current chapter is divided in different sections. The introduction summarizes the state of art of airfoil simulations at low Re numbers together with a description of the most common methods to generate turbulent inflow conditions within LES. Regarding the discussion of the results, two separate section are presented. First, Section 6.2 is focused on setting up an airfoil simulation at low Re numbers under smooth inflow conditions, which is by itself a challenging task. Secondly, Section 6.3 describes the proposed passive grid-generated turbulence technique to produce inflow conditions in LES.

6.1 Introduction

It is very complex to study airfoils at low Re numbers due to the three dimensional nature of laminar separation bubbles (LSB) and spanwise variations in lift and drag. Consequently, the bandwidth of the experimental results at low Re number is quite large and numerical models have serious shortcomings to accurately predict the flow patterns in the low Re number regime.

6.1.1 Modelling low Re number airfoils

For many years, modelling the transition from laminar to turbulent flow has been one of the most difficult challenges of CFD, although many industrial applications have Re numbers between 10^4 and 10^6. In this Re regime, significant portions of the boundary layer can be laminar and the location of the laminar to turbulent transition point is essential for accurate predictions of the performance of aerodynamic devices. The flow is completely determined by the turbulence in the boundary layers and the small spanwise structures must be resolved in order to achieve accurate results. A turbulence resolving technique is required to predict the unsteady and three dimensional nature of laminar separations bubbles, complicating the use of simple steady RANS simulations [131].

Therefore, LES appears as a potential tool in this type of applications. Several well-known researchers from the scientific community participated in the European project *Large Eddy Simulation (LES) of the flow around an airfoil*, also called LESFOIL [132]. The main objective of the LESFOIL project was to assess the suitability of LES for airfoil flow. Accurate LES of wall-bounded flow requires fine cells in the near-wall region

in all coordinate directions. In an attempt to release this constraint, a large part of the LESFOIL project was aimed at developing and validating different approximate near-wall treatments. The simulations performed were based on two-dimensional isolated profiles, which represent a first step toward the real configuration. But even for this simpler case, the accuracy of their different results was not satisfactory. Wall functions are unable to produce accurate solutions for such complex separated flows [133]. When flow separation occurs, the accurate prediction of the separation point has an impact on the result, and the boundary layer needs to be resolved with a finer mesh to account for the flow reversals and reattachment points over the airfoil surface.

As LES and DNS have a prohibitive high computational cost, DES is typically applied for simulating airfoil flows in the last decade [131, 134, 135]. DES is an hybrid LES/RANS approach in which the turbulence outside the boundary layer is resolved and the boundary layer is modeled with URANS solutions. The mesh resolution does not have to be fine enough to resolve the small turbulence structures in the boundary layer, as it is required in LES computations. Instead, the mesh needs to be fine enough to resolve the comparably large scales from the free-stream turbulence [76]. DES simulations have been applied together with transitional models inside the boundary layer to predict flow under massive separation with accuracy [136]. The one equation γ model that Menter [136] proposed in the Local-Correlation based Transition Modelling (LCTM) approach successfully introduced transition effects into the SST $k-\omega$ model, enabling the prediction of the transition point. However, DES simulations still require a considerable mesh resolution, specially if a transitional model is used. The mesh recommendations for the correct implementation of this model states that the y^+ value should be around one, more than 30 cells need to be across the boundary layer, the mesh growth rate should not exceed 1.1, and more than 150 cells along each blade side are required.

Transition models

Most eddy viscosity models (EVM) have been carried out for fully turbulent conditions, neglecting the effect of laminar to turbulent transition process on the flow field as well as on the overall performance. Transition can present different mechanisms (boundary layer bypass transition, separation induced transition, crossflow) that are difficult to model in a physics-based equation framework.

In order to provide unified concept that handle all the different mechanisms, Menter *et al.* [137, 138, 139] proposed the so-called LCTM concept. In this formulation a set of compatible transport equations allow to combine experimental correlations in a local fashion with the underlying turbulence model. Specifically, two additional transport equations have been formulated; one for turbulence intermittency and another one for the transition onset correlation. This formulation is termed as $\gamma - Re_\theta$ model. The Re_θ

equation is required to transport the information of the free-stream turbulence level and the non-dimensional pressure gradient into the boundary layer. The main drawback of this model is that the turbulence intensity $T_u = 100\sqrt{(2/3)k/U}$ enters into the experimental correlation. The free-stream velocity U is not Galilean invariant, and therefore the model is only applicable to simulations where the transitional walls are stationary relative to the coordinate system.

To overcome the limitations of this model, Menter proposed a new one-equation transition model [136]. The main change from the $\gamma - Re_\theta$ model is that the free-stream turbulence level and the pressure gradient parameter are entered into the correlations by computing algebraically local variables inside the boundary layer, and not outside. This removes the need of a second transport equation for Re_θ and maintains the Galilean invariance since it does not require the velocity U. Another advantage is that it simplifies the model drastically compared to the original $\gamma - Re_\theta$ model as the formulation is reduced to only one additional equation (γ equation) while it maintains the LCTM concept, including the ability to model essentially all transitional processes for which correlations can be formulated.

Intermittency-based one-equation transition model

Also called γ model, it has currently been combined with SST k-ω with the inclusion of a third the transport equation for the intermittency γ, as follows:

$$\frac{\partial}{\partial t}(\rho\gamma) + \frac{\partial}{\partial x_j}(\rho U_j \gamma) = \frac{\partial}{\partial x_j}\left[\left(\mu + \frac{\mu_t}{\sigma_\gamma}\right)\frac{\partial \gamma}{\partial x_j}\right] + P_\gamma - E_\gamma. \tag{6.1}$$

The transition source term is defined as:

$$P_\gamma = F_{length}\rho S\gamma(1-\gamma)F_{onset}, \tag{6.2}$$

where S is the strain rate magnitude. This term is designed to be equal to zero (due to the F_{onset} function) in the laminar boundary layer upstream of transition and is active once the local transition onset criteria is met. The magnitude of this source term is controlled by the transition length function, F_{length}, which is a constant parameter.

The destruction/relaminarization source is defined as follows:

$$E_\gamma = c_{a2}\rho\Omega\gamma F_{turb}(c_{e2}\gamma - 1), \tag{6.3}$$

where Ω is the magnitude of the absolute vorticity rate.

The formulation of the function F_{onset}, which is used to trigger the intermittency production (Equation (6.2)) contains the ratio of the local vorticity Reynolds number

Re_V to the critical Reynolds number $Re_{\theta c}$. The $Re_{\theta c}$ is not computed from a transport equation, instead, it is computed algebraically using k and other local variables. As a result, the transition onset is controlled by the following functions:

$$F_{onset1} = \frac{Re_V}{2.2Re_{\theta c}}, \; F_{onset2} = \min(F_{onset1}, 2.0) \tag{6.4}$$

$$F_{onset3} = \max\left(1 - \left(\frac{R_T}{3.5}\right)^3, 0\right), \; F_{onset} = \max(F_{onset2} - F_{onset3}, 0) \tag{6.5}$$

$$F_{turb} = e^{-\left(\frac{R_T}{2}\right)^4}, \; R_T = \frac{\rho k}{\mu\omega}, \; Re_V = \frac{\rho d_w^2 S}{\mu}, \; Re_{\theta c} = f(Tu_L, \lambda_{\theta L}) \tag{6.6}$$

The model constants are:

$$F_{length} = 100, \; c_{e2} = 50, \; c_{a2} = 0.06, \; \sigma_\gamma = 1.0. \tag{6.7}$$

In these equations, d_w is the wall distance and ω is the turbulence frequency (obtained from the ω-equation). The local formulations of Tu_L and $\lambda_{\theta L}$ are designed so that $Re_{\theta c}$ has meaningful values in a region between the middle and the edge of boundary layer, where triggering of the transition model starts. More details on the arguments Tu_L and $\lambda_{\theta L}$ entering the correlation $Re_{\theta c}$ can be found in [136].

Apart from traditional CFD, theoretical models significantly reduce the computational requirements. Vortex panel methods are techniques for solving incompressible potential flow over thick 2D and 3D geometries. In 2D, the airfoil surface is divided into piecewise straight line segments or panels and vortex sheets placed on each panel. These vortex sheets mimic the boundary layer around airfoils. One of the most used panel method is Xfoil, developed by Professor Drela at MIT [140]. This inviscid linear-vorticity panel method superimposes source distributions on the airfoil and wake permitting the modeling of viscous layer influence on the potential flow. A two-equation lagged dissipation integral method is used to represent the viscous sublayers. Both laminar and turbulent layers are treated, determining the transition point. The boundary layer and transition equations are solved simultaneously with the inviscid flow field by a global Newton method. The procedure is specially suitable for rapid analysis of low Re number airfoils with transitional separation bubbles. Xfoil can handle small to medium sized separation regions quite accurately, however, when separation gets larger the results are less realistic. Another shortcoming is the fact that only low turbulence levels can be introduced.

6.1.2 Turbulent inflow generation within LES

The treatment of inlet conditions for a fully turbulent region in LES is a complex problem, but of extreme importance as, in many cases, the fluid behavior within the domain is determined in large part by the inlet behavior. Since LES solves the energy-carrying eddies, the inflow conditions specified at the inlet boundary should ideally represent the contributions of these eddies. These conditions are crucial to optimize the performance of devices under free-stream turbulence or even higher turbulence intensities.

Numerous studies exist in literature where this effects have been analyzed. Tutar *et al.* analyzed the influence of inflow turbulent conditions on bluff bodies [141], a circular cylinder [142], a square cylinder [143] and also on other engineering applications like transonic turbines [144].

The selection of inflow values at the inlet boundaries for turbulence models in aerodynamic calculations is not an easy task. There does not appear to be a consistent standard practice and most CFD codes handle the issue differently. Spalart *et al.* [145] probed in their work that inlet values of viscosity ratio (μ_t/μ) have a strong influence on the free decay rates of turbulence quantities. Typically, the larger inlet viscosity ratio, the smaller turbulent decay rate. However, if too large viscosity ratio is specified (greater than 100), the skin friction can deviate significantly from the laminar value.

For this reason, it is desirable to keep a relatively low inlet viscosity ratio (between 1-10) [115]. The main inconvenient is that it is sometimes not feasible to maintain the viscosity ratio at that level while introducing high turbulence intensity values at the inlet boundary. A high turbulence intensity I at the inlet produces high turbulence kinetic energy values. As a consequence, the specific dissipation rate ω in the SST $k-\omega$ model (which is related to the turbulent viscosity as $\omega = \frac{\rho k}{\mu_t}$) is too high. This results in a dramatic or non-physical decay of k and ω turbulence quantities and the local turbulence intensity downstream the inlet can be much smaller than the inlet value. It is therefore difficult to generate high turbulence levels in numerical simulations. This is a serious shortcoming, as inflow turbulence has a significant impact on the aerodynamic performance on airfoils operating inside the atmospheric boundary layer (ABL).

To reproduce high turbulence levels in a numerical simulation, the eddies in the free flow must be resolved in order to transport their momentum to the inner region of the boundary layer. Therefore, a turbulence resolving technique must be used to predict these effects [76]. Gilling *et al.* [146] studied the effect of resolving inflow turbulence in DES simulations of airfoil flows. The results show that the flow is sensitive to the intensity of the resolved turbulence, specially when the flow is close to stall. However, the synthetic inflow boundary conditions employed only permitted to reach values up to

2 %, which are below the turbulence levels encountered inside the atmospheric boundary layer. Daniele *et al.* [147] achieved to increase the turbulence level up to 3.6 % by imposing inlet values of turbulence intensity such that at the leading edge of the airfoil, the turbulence intensity has decayed to the desired value.

There does not appear to be a consistent standard practice for dealing with the inflow turbulence in LES. According to Tabor and Baba-Ahmadi [148], the existing methods in the literature for generating turbulent inflow conditions can be classified in two basic categories: *Synthesized* methods, in which random fluctuations are artificially generated and combined with the mean flow at the inlet, and *precursor simulation* methods, in which some form of turbulence is precomputed before the main calculation and introduced into the flow domain at the inlet.

Synthesized turbulence methods

Synthesis methods consists in artificially generating random time series of velocity fluctuations combined with the mean flow. The main advantage of these methods is that they are easy to manipulate to specify the desired turbulent properties, such as turbulent length scales or energy levels. On the other hand, the fluctuations are invariably generated at different length and time scales without proper phase information, which is related to the structure and shape of the turbulent eddies. Keating and Le [149, 150] claimed that without this structural information inflow conditions cannot be expected to be accurate because the random fluctuations are not correlated and thus, the flow lacks realistic turbulent structure and the turbulence level in the separated shear layer decays rapidly.

A number of synthesized turbulence methods exists in literature. In this study, the vortex method [151] and the random flow generation [152] are considered.

Vortex method (VM)

The random 2D vortex method generates fluctuations that, unlike the random noise, contains some spatial correlations [151]. In this approach, a perturbation is added on a specified mean velocity profile via a fluctuating vorticity field (in the plane normal to the streamwise direction) which gives a spatial correlation. Based on the Lagrangian form of the 2D evolution equation of the vorticity, a particle discretization is used to solve this equation. These particles, or centers of the vortices are convected randomly and transport the information about vorticity field. If N is the number of vortex points and A is the area of the inlet section, the amount of vorticity carried by a given particle i is represented by the circulation Γ_i and an assumed spatial distribution η:

$$\Gamma_i(x,y) = 4\sqrt{\frac{\pi A k(x,y)}{3N[2\ln(3) - 3\ln(2)]}}, \tag{6.8}$$

and

$$\eta(\vec{x}) = \frac{1}{2\pi\sigma^2}\left(2e^{-|x|^2/2\sigma^2} - 1\right)2e^{-|x|^2/2\sigma^2}, \tag{6.9}$$

where k is the turbulence kinetic energy and the parameter σ controls the size of a vortex particle. The resulting discretization for the velocity is given by

$$\vec{u}\ (\vec{x}) = \frac{1}{2\pi}\sum_{i=1}^{N}\Gamma_i\frac{((\vec{x}_i - \vec{x})\times\ \vec{z})\left(1 - e^{-\left|\vec{x}-\vec{x}'\right|^2/2\sigma^2}\right)}{\left|\vec{x} - \vec{x}_i'\right|^2}, \tag{6.10}$$

where $\vec{z}$ is the unit vector in the streamwise direction. The size of the vortex σ is specified through a turbulent mixing length hypothesis, calculated from a known profile of mean kinetic energy and mean dissipation rate at the inlet according to the following:

$$\sigma = \frac{ck^{3/2}}{2\epsilon}, \tag{6.11}$$

where $c = 0.16$.

Random Flow Generation (RFG)

The present random flow generation technique is developed by Smirnov *et al.*[152]. The fluctuating component is derived from the turbulence intensity, and length-scales provided by the turbulence model or via empirical relations. In this procedure adopted here a homogeneous isotropic transient flow field is realized as a superposition of harmonic functions as previously suggested by [153]:

$$\vec{v}\ (x,t) = \sqrt{\frac{2}{N}}\sum_{n=1}^{N}\left[\vec{v}_1\ (\vec{k}_n)\cos(\vec{k}_n\vec{x}\ +\omega_n t) + \vec{v}_2\ (\vec{k}_n)\sin(\vec{k}_n\vec{x}\ +\omega_n t)\right]. \tag{6.12}$$

In this equation,

$$\vec{v}_1\ (\vec{k}_n) = \vec{\zeta}_n\ x(\vec{k}_n),\ \vec{v}_2\ (\vec{k}_n) = \vec{\varsigma}_n\ x(\vec{k}_n), \tag{6.13}$$

with

$$\vec{k}_n\vec{v}_1\ (\vec{k}_n) = \vec{k}_n\vec{v}_2\ (\vec{k}_n) = 0, \tag{6.14}$$

where the components of vectors ζ_n and ς_n and the frequency ω_n are chosen independently from a Gaussian distribution with a standard deviation of unity, $N(0,1)$. Each component is a Gaussian random number with a standard deviation of $1/2$. Here, N is the

number of terms in series. The generated flow-field is then homogeneous, isotropic and divergence-free [152]. Velocity fluctuations are calculated in accordance with a proper selection of length and time scales for the turbulence conditions and then returns the calculated values of fluctuating velocity components at each grid point of the inflow boundary at each time step.

Precursor simulation methods

These methods use separate calculations to generate a library of turbulent data that can be introduced at the inlet of the main computation. The main advantage is that the inflow conditions for the main computation are taken from a genuine simulation of turbulence, and thus should possess many of the required characteristics, including temporal and spatial fluctuations with correlation and a correct energy spectrum. This data can be generated in a number of ways by the use of periodic boxes of turbulence or cyclic channel flow calculations, internal mapping, and precomputed simulation and/or experimental database of well-known canonical flows, such as decaying homogeneous turbulence (Section 4.1.2).

For example, flow in a channel bounded by flat plates reproduce velocity profiles that have been measured very accurately, so this serves as a good test case. Since the flow in a long pipe becomes fully developed sufficiently far downstream from the inlet, a very long distance would be required to reach this condition. Computationally, this would be prohibitive due to the amount of cells and the consequent computational cost. However, this can be sorted out by the use of cyclic boundaries. If flow out of the outlet of the domain is reintroduced directly into the inlet through some sort of mathematical mapping, then the flow recirculates through the same domain endlessly, and will quickly arrive at a fully developed state. Cyclic domains are valuable tools, enabling the computation and study of fully-developed flow in a short domain space and have been extensively used in fundamental studies of LES and DNS, and in the study of wall bounded flows [154, 155]. However, they still require the generation and storage of a separate database.

Precursor databases are extensively used for LES. The main drawback is that if the library does not meet the specifications for the required flow, the data needs to be rescaled to the desired statistical properties (specified mean and variance of velocity). According to Wang and Bai [156], this rescaling does cause problems as the level of turbulence kinetic energy is seen to decrease downstream of the inlet, due to the unphysical turbulence at the inlet adapting to become true turbulent flow further downstream.

A modification of these precursor methods is to run the precursor calculation continuously in parallel with the main simulation. Such a technique was originally proposed by Lund *et al.* [157]. This method, which was developed for flat-plate boundary lay-

ers, consists of taking a plane of data from a location several boundary-layer thickness δ downstream of the inflow, and rescaling the inner and outer layers of velocity profiles separately, to account for the different similarity laws that are observed in these two regions. The main shortcoming is the fact the inlet must be placed in a region in which the flow is in an equilibrium, well-known condition (flat-plate boundary layer, for instance) and a fairly long domain must be used for the region of interest for the recycling.

One disadvantage of all these methods is the necessity to set up and run a separate calculation involving a separate mesh, either a priori or concurrently with the main computation. However, there is actually no reason why the precursor calculation cannot be integrated into the main domain. In this context, Blackmore *et al.* [158] applied the canonical case of grid-generated turbulence (Section 4.1.2) to develop a *gridInlet* technique by projecting solid patches on the inlet simulating different grid topologies. This allows the turbulence integral length scale to be controlled by changing the grid size, while the turbulence intensity is controlled by changing the inlet distance. They showed that this technique can be used to generate isotropic turbulence with intensities up to 20 % and the rate of growth of integral length scales compared well with wind tunnel studies. Therefore, this new technique of generating turbulence in LES could be useful for free-stream investigations under high intensity isotropic turbulence.

6.2 Airfoil simulations at low Re number

Prior to studying the effect of free-stream turbulence in simulations of airfoils, it is necessary to setup a computational model of the airfoil section to be analyzed under smooth inflow conditions. The subsonic flow around a NACA0021 airfoil is studied at Re number of 100000 for validation purposes against experimental data available in Chapter 3.

Since the large scales from free-stream turbulence need to be resolved [76], simple steady RANS simulations cannot produce accurate results. Therefore, a turbulence resolving technique is used. In order to get good results in airfoil flow simulations, the prediction of the transition is more important than the near-wall modelling [159]. The flow is completely determined by the turbulence in the boundary layers and the log law in the wall functions around the suction side of the airfoil is not accurate. For this reason, a DES hybrid approach is used to simulate the airfoil where turbulence outside the boundary layer is resolved and the boundary layer is modeled with an URANS solution. The intermittency-based one-equation transition model (γ model) is used to introduce transition effects into the SST $k-\omega$ model, enabling the prediction of the transition point.

In the subsequent sections the computational model together with the numerical methodology is defined and the results obtained are presented.

6.2.1 Computational domain and boundary conditions

The computational domain is reproduced corresponding to the geometry of the wind tunnel test section where the experiments are conducted. Due to the three dimensional and transient nature of laminar separation bubbles, a 3D simulation would be more realistic. However, the model is defined as two-dimensional as a first step to the real configuration and permits to decrease the computational cost of the simulation. The domain consists of a C-type mesh around the airfoil and the rest of the domain is splitted in different blocks to permit a mapped face meshing. This meshing methodology eases the transition of the cells growing from the boundary layer to the free-stream area of the model maintaining a good mesh quality.

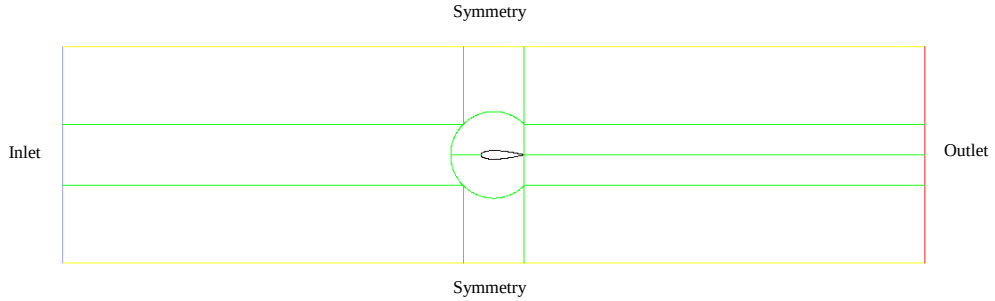

Figure 6.1: 2D computational domain. The angle of attack in the shown mesh is 0°

According to Gilling [76], the influence of the tunnel walls should be similar in both experiments and simulations so that the results can be directly compared, without the necessity of applying wall corrections. For this reason, the airfoil is modeled inside the wind tunnel leaving the same distances to the walls as in the experiments (airfoil centered in a 3 m long and 0.75 m width domain). Symmetry boundary conditions are used on the top and bottom boundaries to limit the flow without having to resolve the boundary layer of a no-slip wall. The airfoil is centered along the test section length and the inlet and outlet boundaries corresponds to the entrance and exit of the test section. Outflow boundary condition is used at the outlet boundary and the inlet velocity is set to 10 m/s. The turbulence parameters at the inlet, turbulence kinetic energy k_{inlet} and specific dissipation rate ω_{inlet}, are estimated by employing the Random Flow Generated (RFG) algorithm [152] so that the turbulence intensity at the leading edge of the airfoil has decayed to 0.3 %, which is the turbulence level inside the wind tunnel. The decay of turbulent kinetic energy can be calculated with the following analytical solution [115]:

$$k = k_{inlet}(1 + \omega_{inlet}\beta t)^{\frac{-\beta^*}{\beta}}, \tag{6.15}$$

where β=0.09 and β^*=0.0828 are the free-stream constants for the SST $k-\omega$ turbulence model and $t = \frac{x}{U}$ is the time scale with x being the streamwise distance downstream of the inlet and U is the free-stream velocity.

Up to five flow domains are created corresponding to the angle of attack (0°, 5°, 10°, 15° and 20°) to be computed. The same mesh criteria is followed for all the simulations performed. The number of cells ranges from 142000 to 145000 and 180 elements are employed along the sides of the airfoil. Each of the computational mesh is checked to have acceptable values of maximum skewness below 0.8 which is considered to be a good quality [115]. Large aspect ratio is not accepted where strong transverse gradient is expected in the boundary layer, so the aspect ratio is kept below 50. More than 30 cells are across the boundary layer and the mesh growth rate does not exceed 1.1. In Table 6.1 the correspondent mesh quality data is provided for each of the simulations.

Table 6.1: Mesh quality of the computational domains

AoA	0°	5°	10°	15°	20°
Skewness	<0.58	<0.65	<0.63	<0.66	<0.72
Aspect ratio	<43	<54	<49	<46	<45
Number of cells	142190	142190	145088	144809	145063

Figure 6.2 shows a detailed view of the mesh for cases $AoA = 0°$ and $AoA = 20°$.

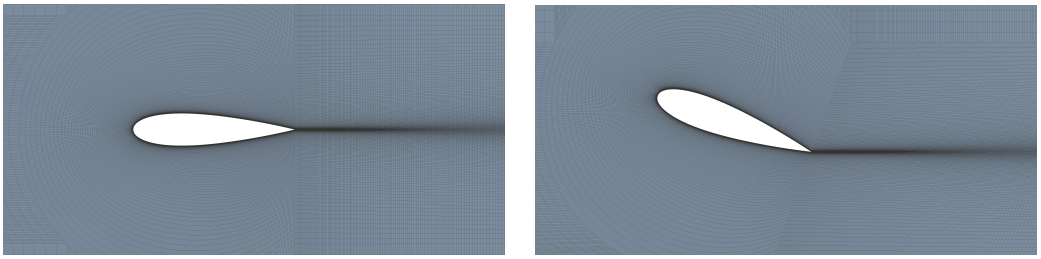

(a) (b)

Figure 6.2: Detailed view of the mesh of the two-dimensional mesh: (a) $AoA = 0°$ and (b) $AoA = 20°$

6.2.2 Numerical solver methodology

In this study DES simulations are carried out using a finite volume solver which employs a finite volume method (FVM) for solving the incompressible Navier-Stokes equations within transient assumptions. In the present FVM method, the solution domain is subdivided into a finite number of continuous control volume (CV), and the non-linear conservation equations are transformed into analogous algebraic equations for each CV, and these equations are solved by a segregated solution algorithm. Specifically, the Pressure Implicit with Splitting of Operator (PISO) pressure velocity coupling scheme is used for the present numerical fluid flow solver.

The resultant scalar system of equations for the dependent variable in each cell is solved with a bounded second order implicit time integration scheme. These transient computations for the DES method are then performed for long time-average solutions of flow past the domain, so that all statistics for the DES computations are averaged over a period of at least ten cycles (or mean flow residence time), being a cycle the mean time that a fluid particle takes to travel along the total length of flow domain ($t_{cycle} = x/U$, where x is the flow domain length and U is the free-stream velocity). When simulating airfoils, Gilling *et al.* [76] may also refer to non-dimensional time tU/c by normalizing the simulation time t with the airfoil chord length c. In the current model, ten cycles are equivalent to 200 time units, which is enough time for the flow to develop and become a stationary stochastic process [76].

The time step Δt=1e-05 s is assigned to obtain a maximum Courant number $Co = U\Delta t/\Delta x = 1$, which leads to a total of 300000 time steps. The solution convergence criterion is set to 1e-05 for all solution variables. Simulations are performed using the cluster computing facility available at MU in double precision with up to a total of 84 cores (2.30 GHz Intel Xeon E5-2695v3 and 64 GB RAM). Table 6.2 shows the computational cost of each simulation per mean flow residence time.

Table 6.2: Computational cost of the airfoil simulations at low Re number

AoA	0°	5°	10°	15°	20°
TWCT[1] per mean flow residence time (h)	16.5	17.2	23.1	28.8	26.4

[1] Total Wall-Clock Time

The resulting computational cost is quite high, due to the low time step employed and the large number of times steps that are required to reach a sufficiently long time solution. It is noteworthy here that the computational cost is lower at low AoA, corresponding to the attached flow condition here. As the AoA increases, the flow is more separated

and the computational cost increases as it takes more iterations to reach a converged solution on each time step. In any case, no more than 20 iterations are required to reach convergence within a time step.

6.2.3 Results and discussions

Prior to the discussion of the results it is recommended to check the obtained y^+ values as it is known that the γ model is very sensitive to it [136]. Figure 6.3 ensures that most of the cells are below one along the curved airfoil edge, except some cells near the leading edge in the case of $AoA = 20°$ where the flow is accelerated.

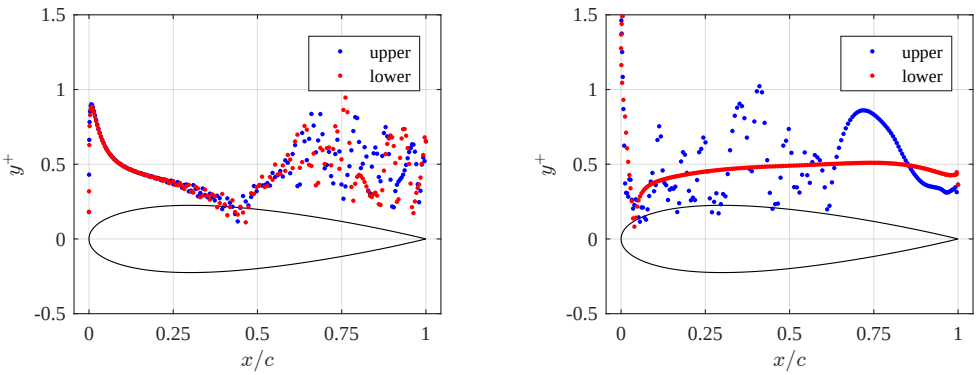

(a) (b)

Figure 6.3: y^+ values for the upper and lower sides of the airfoil at interval t=3 s: (a) $AoA = 0°$ and (b) $AoA = 20°$

Figure 6.4 shows the instantaneous u velocity contour plots for the limiting angle positions of $AoA = 0°$ and $AoA = 20°$. It can be seen how the LES formulation outside the boundary layer of the airfoil solves the flow structures that are larger than the mesh employed. This permits to numerically reproduce the vortex shedding in the wake of the airfoil. On the other hand, the transitional model inside the boundary layer is able to compute massively separated flows, such as in the case of $AoA = 20°$. The one equation γ model [136] successfully introduces transition effects into the SST $k-\omega$ model, enabling the prediction of the transition point and the formation of laminar separation bubbles.

Due to the transient nature of low Re airfoil flows, it is required to check the time averaging of the simulations performed. Figure 6.5 shows the temporal signals and the obtained mean values of the main aerodynamic coefficients, C_D and C_L, for the case of $AoA = 0°$. To do a proper time averaging, the first 30 time units (transitory part of the signal) are removed to include only the time interval where the flow becomes stationary. The adopted total simulation time of 200 time units ensures that the flow is stable with constant mean aerodynamic coefficients. The mean lift coefficient is zero as corresponds to a symmetric airfoil for $AoA = 0°$, even if the lift coefficient varies with amplitudes up

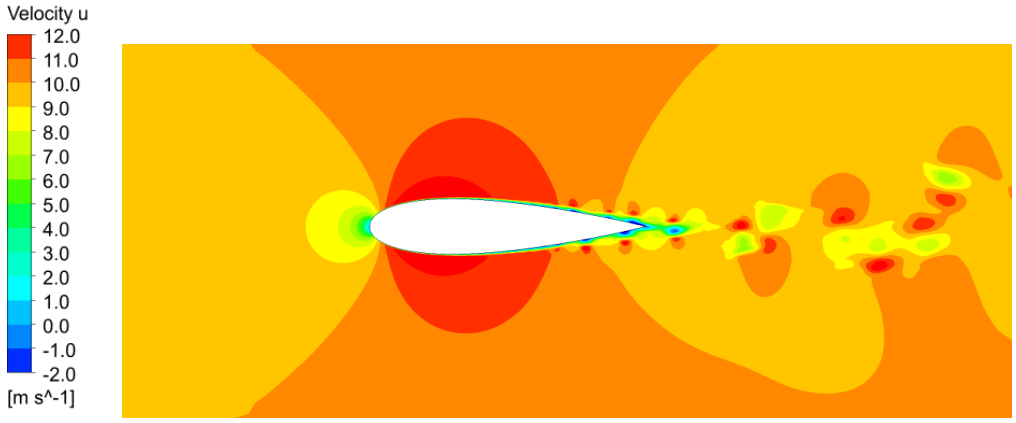

(a)

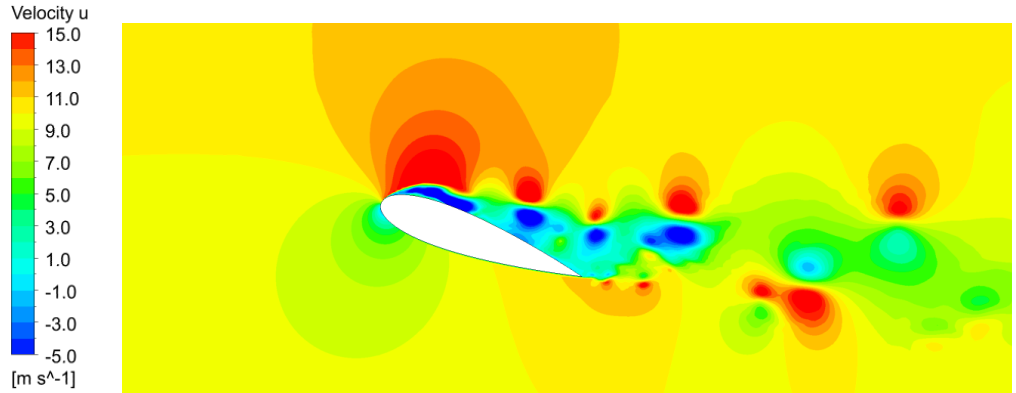

(b)

Figure 6.4: Instantaneous u velocity field at interval t=3 s: (a) $AoA = 0°$ and (b) $AoA = 20°$

to $\pm$ 0.15.

In Figure 6.6 the computed mean drag and lift coefficients are compared to the experimental data available in Chapter 3 and to Xfoil calculations. In general, good agreement is obtained at angles of attack between $AoA = 0° - 10°$. Although experimental drag polar is above the numerical computations in this range, it should be noted here that this discrepancy can be partly explained due to experimental model deficiencies (Section 3.2.2). The good agreement obtained between Xfoil and DES-γ model suggests that both methods reproduce reliable results when an attached flow condition occurs. As regards to the C_L polar, the laminar separation bubble has a marked effect in the experimental data since the slope discontinuities are more prominent.

The results at angles $AoA = 15°$ and $AoA = 20°$ are less consistent. The experimentally measured stall is much more abrupt, resulting in a significant loss of lift. The DES-γ model does not capture the stall condition correctly and overpredicts the post-stall lift coefficients. These results manifests the difficulty of producing accurate solutions for such complex separated flows. Even with the finer mesh employed across the boundary

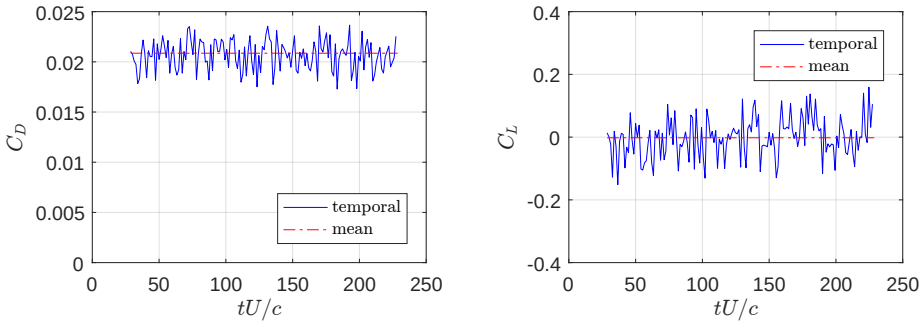

(a) (b)

Figure 6.5: Time series and mean values for $AoA = 0°$: (a) C_D coefficient and (b) C_L coefficient

layer over the airfoil, separation characteristics are not exactly captured by the numerical model. Regarding Xfoil results, a plateau is observed starting at the stall angle instead of the sudden drop reproduced experimentally. This evidences that when separation gets larger, the results provided by both methods become less realistic.

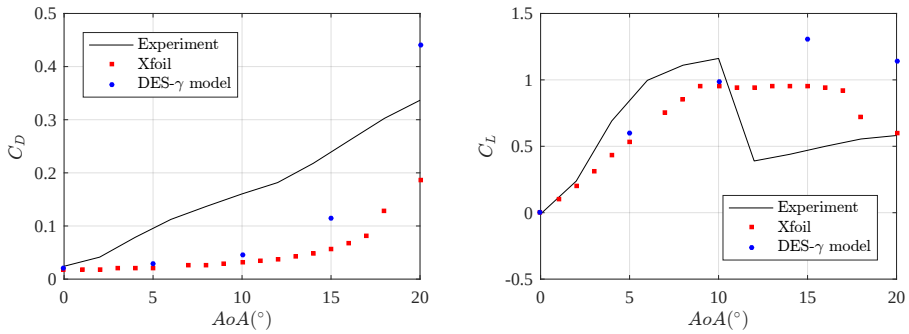

(a) (b)

Figure 6.6: Comparison between drag C_D and lift C_L coefficients between experiments, Xfoil and DES-γ model

To get more insight on the numerical results, Figure 6.7 provides the mean pressure coefficient $C_p = 2(p - p_\infty)/\rho U^2$ and the mean skin friction coefficient $C_f = 2\tau_\omega/\rho U^2$ along the airfoil surfaces. The mean C_p coefficient is plotted for both Xfoil and DES-γ model for comparison, while the mean C_f coefficient is only available for DES-γ model. The direction of the y-axis in the C_p plot is reversed to make the upper side of the airfoil coincident with the suction side.

As noted before, the agreement between numerical models is good for cases with small to medium sized separation regions ($AoA = 0° - 10°$). The suction peak near the leading edge and the stagnation point in the pressure side coincides with accuracy. Both methods successfully introduce transition effects enabling the prediction of the transition point and the formation of laminar separation bubbles. The plateau observed in the

pressure distribution plots indicates the presence of a laminar separation bubbles. The size of the laminar separation bubbles are also well predicted since the plateau initiates at similar x/c coordinates and ends with a sharp gradient, what means that the turbulent reattachment point also matches. This sharp end is at ≈ 0.65 for the case of $AoA = 0°$, and gradually decreases for higher angles of attack. For the case of $AoA = 5°$ the turbulent reattachment point is around 0.45 and for the case of $AoA = 10°$ is around 0.25. The size of the laminar separation bubble can be also extracted from the C_f plots. The point where C_f coefficient reaches zero value is the laminar separation point, which is the start of the laminar separation bubble. The C_f stays near zero value in the reverse flow region of the laminar separation bubble until a sudden peak is obtained at the turbulent reattachment point.

At higher angles both methods produce less realistic results. The size of the laminar separation bubble that Xfoil reproduces is shorter compared to the DES-γ model for the case of $AoA = 15°$. Indeed, the size of the laminar separation bubble reproduced with the DES-γ model is quite similar to the case $AoA = 10°$, with the difference that the peak in the C_p distribution is more pronounced. Due to this the lift coefficient at $AoA = 15°$ is higher and does not experience a sudden drop, making it inconsistent with the experiment as it does not correspond to a stalled state of the airfoil. At $AoA = 20°$ the flow is massively separated with various separation and reattachment points, pointing out the difficulty of reliably simulating this condition.

Although Xfoil computations require a considerable lower computational cost compared cost compared to DES-γ models, only low turbulence levels can be introduced. If high intensity turbulence levels need to be computed, a turbulence resolving technique such as LES must be used to predict the effect of inflow turbulence. The following chapter describes the proposed inflow turbulence generation method, which is based on the use of a passive grid to generated prescribed turbulent inflow conditions.

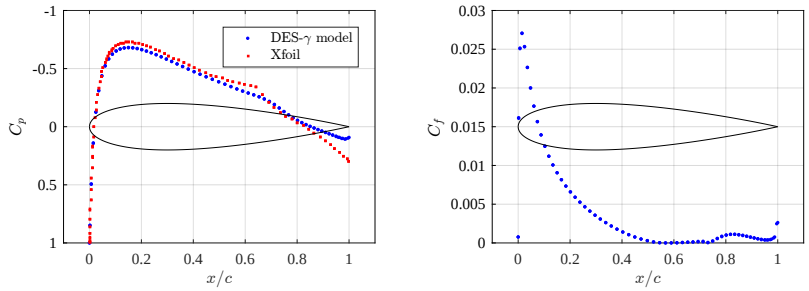

(a) $AoA = 0°$

(b) $AoA = 0°$

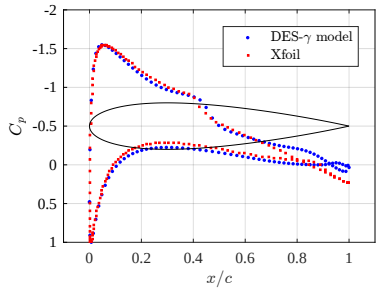

(c) $AoA = 5°$

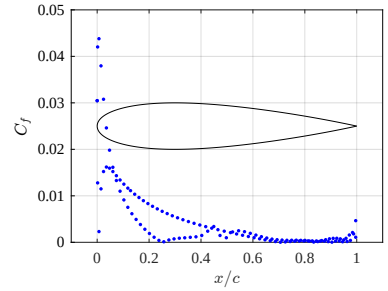

(d) $AoA = 5°$

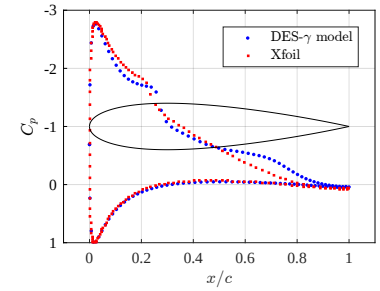

(e) $AoA = 10°$

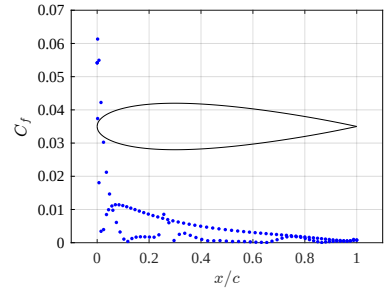

(f) $AoA = 10°$

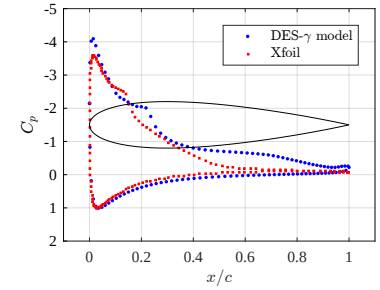

(g) $AoA = 15°$

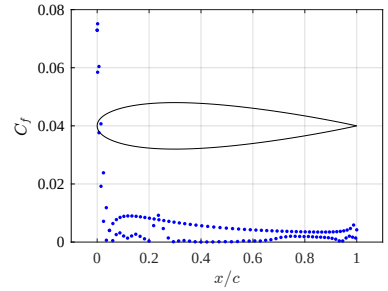

(h) $AoA = 15°$

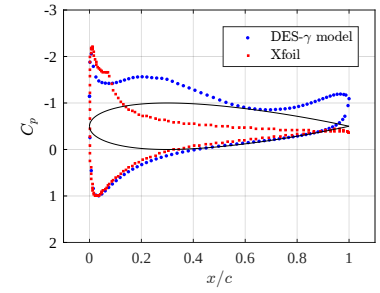

(i) $AoA = 20°$

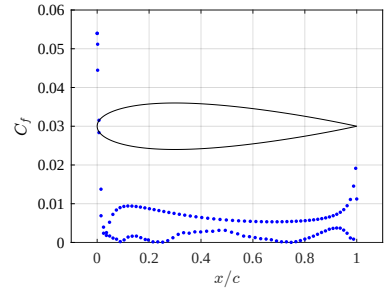

(j) $AoA = 20°$

Figure 6.7: Mean surface pressure C_p and skin friction C_f coefficients.

6.3 LES study of grid-generated turbulent inflow conditions

The aim of this study is to produce a reliable and cost effective solution for generating turbulent inflow conditions. Given that synthetic inlets dissipate quickly due to the lack of turbulence generation mechanism, a LES model of grid-generated turbulence is computed where the grid is introduced in the computational domain as a wall boundary condition. In order to decrease the computational cost a near wall modelling approach is employed in the solid boundary of the grid. First, the results are compared with existing synthetic methods, with the method proposed by Blackmore *et al.* [158] and with experimental data presented in Chapter 5. Then a mesh sensitivity analysis is provided to analyze the effect of mesh resolution and the wall modelling technique in the large scale properties downstream of the grid.

6.3.1 Computational domain and boundary conditions

Three different flow domains are created corresponding to the different methodologies employed for generating the decay of turbulence. The overall dimensions are set to coincide with the experimental wind tunnel described in Section 3.10, as shown in Figure 6.8. The main difference between the flow domains is due to the way of generating the turbulence inflow conditions at the inlet. The inlet velocity for all cases is set to $U = 5$ m/s which leads to a Reynolds number of $Re = \frac{UM}{\nu} = 16666$, adopting the mesh spacing of the grid M as characteristic length scale of the flow. Outflow boundary conditions are used at the outlet boundary and free-slip condition is applied to wind tunnel walls.

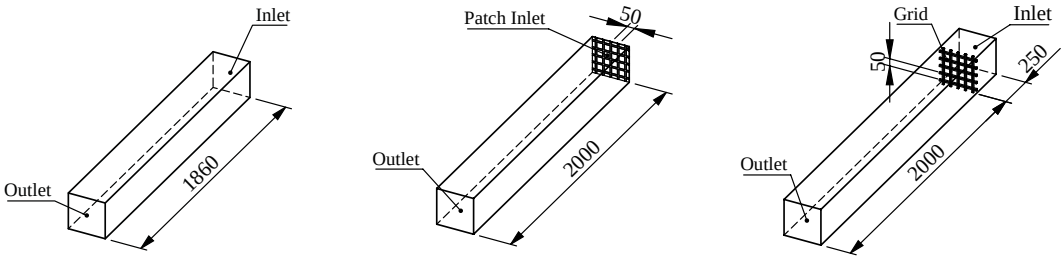

(a) Cases 1 and 2 (b) Case 3 (c) Cases 4-6

Figure 6.8: Computational domain and boundary conditions of cases 1-6 (units in mm)

The domain in cases 1 and 2 is used with synthetic inlets, so there is no solid boundary to generate the cascade of eddies. The level of turbulence at the inlet is introduced based on the experimental data available for the first measured point, which is located at 0.14 m downstream of the grid. This makes the total length of the domain decrease compared

to the rest of the domains. The inlet parameters are set as follows; turbulence kinetic energy $k = 1.6736$ m^2/s^2 and turbulence dissipation rate $\epsilon = 82.7823$ m^2/s^3. Given these turbulent inlet parameters, the size of vortices for the vortex method (case 1) is computed using the Equation (6.11).

Case 3 is the method proposed by Blackmore *et al.*[158]. A pattern of solid patches is incorporated on the inlet simulating an identical grid as used in the experiments. Turbulence is generated due to the shear between the inlet flow and solid areas. As there is no physical grid in the domain the total length of the domain is 2 m, which is equal to the test section length of the experimental wind tunnel. The inlet velocity in this case is calculated using the grid porosity $\theta = 0.64$ and free-stream velocity $U = 5$ m/s; $u_{inlet} = U/\theta = 7.8125$ m/s.

In cases 4-6 the grid is physically represented in the computational domain as a wall boundary with no-slip condition imposed on it. The grid hereby functions as a post-inflow boundary to regenerate the turbulence inside the flow domain to develop unsteady turbulent inflow conditions with more realistic physical properties. For this method, the flow domain is further extended (0.25 m) prior to the location of the grid to set the inlet velocity. For setting the turbulent parameters at the inlet, it is known from experiments that the turbulence intensity is 2 % when the wind tunnel is empty. Turbulent inflow conditions are defined based on this parameter by employing the RFG algorithm [152].

The mesh resolutions used are provided in Table 6.3. Cases 1-4 use the same mesh resolution for a direct comparison of the inflow turbulence generation methods. Regarding cases 4-6, different meshing strategies are performed for analyzing the mesh sensitivity of the model. Case 4 and 5 do not present a high mesh resolution in the near wall region of the grid (y^+ values are between 30 and 300) and thus, the logarithmic law of the wall is applied. However, case 6 employs finer mesh elements comprised by 10 inflation layers that provide a suitable mesh density in the vicinity of the wall (y^+ values in the order of 1) for solving the turbulent eddies until the viscous sublayer.

Table 6.3: Grid layouts of the performed meshes

Case	Inlet type	Cell density[1]	Wall y^+
1	Synthetic (VM)	10 × 10	-
2	Synthetic (RFG)	10 × 10	-
3	Patch inlet	10 × 10	-
4	Grid turbulence	10 × 10	30-300
5	Grid turbulence	20 × 20	30-300
6	Grid turbulence	20 × 20	≈ 1

Table 6.4: Ratios of $L/\Delta x$, $\lambda/\Delta x$ and $\eta/\Delta x$

		x/M=10	x/M=20	x/M=40
Case 4	$L/\Delta x$	3.51	4.23	5.31
	$\lambda/\Delta x$	0.63	0.85	1.15
	$\eta/\Delta x$	0.02	0.05	0.10
Cases 5, 6	$L/\Delta x$	7.02	8.47	10.62
	$\lambda/\Delta x$	1.25	1.70	2.30
	$\eta/\Delta x$	0.05	0.10	0.21

6.3.1.1 LES uncertainty quantification (UQ) analysis

The uncertainty quantification (UQ) can be analyzed with different criteria, such as convergence criteria, mesh resolution or Smagorinsky constant C_s choice. This uncertainty analysis is made in the context of the different meshing methodologies employed, as the convergence criteria and the C_s value are constant for all the simulations. The verification of LES calculations is difficult because of the fact that both the sub-grid scale (SGS) model and numerical discretization errors are function of the grid resolution.

According to Baggett *et al.* [160], the grid spacing used in LES simulations should be some minimal ratio of the integral length scale. In order to resolve all large turbulent scales in the flow, a proper LES simulation should resolve 80 % of all turbulence length scales. For homogeneous isotropic turbulence, it can be shown that 80 % of the energy is resolved when $\Delta \cong \lambda$ [20], where λ is the Taylor microscale. In this study, the turbulent length scales are estimated based on the experimental data available presented in Chapter 5. Turbulent length scales evolve according to power laws, and more specifically, the Taylor microscale λ varies from a value of 1.7 mm in the near field region to 5.8 mm in the far field region. These measurements were used to set an initial criteria for the mesh resolution in the LES simulations, as specified in Table 6.3. In addition to this, Table 6.4 shows the ratios obtained for the turbulent length scales $L/\Delta x$, $\lambda/\Delta x$ and $\eta/\Delta x$ for different positions (x/M=10, x/M=20 and x/M=40) along the streamwise direction. Cases 4 and 5 have the same results as the mesh resolution only varies in the near wall region. It can be observed that the ratio $\lambda/\Delta x$ is below unity for case 3 in the region $x/M < 20$, so the mesh resolution here cannot capture properly the small-scale motions and the SGS turbulence model is active in this zone. It is important to remind that the objective of the current study is to test the ability of LES simulations to capture the large scale properties of grid-generated turbulence with moderate number of mesh cells.

A number of different criteria have been investigated to determine the spatial and temporal resolution of the LES results. According to Vreman [161, 162], there are two

approaches for testing the performance of SGS models: (i) a priori tests where model predictions are compared to SGS stresses obtained from DNS or experiments; (ii) a posteriori testing whereby actual LES results are compared with results from DNS or experiments. At this stage, a priori evaluation of the resolution quality is performed. Celik [163] propose an LES index of quality based on grid resolution relative to the Kolmogorov length scale, η_k:

$$LES\ IQ_{\eta_k} = \frac{1}{1 + \alpha_n(\frac{h}{\eta_k})^m} \tag{6.16}$$

In this study η_k is obtained from the experiments $\eta = \sqrt[4]{\nu^3/\epsilon}$. The parameters α_n and m can be defined as functions of Re_λ and Δ/h according to the equation $\frac{h}{\eta_k} = \frac{{Re_\lambda}^{3/4}}{8(\Delta/h)}$. For a Reynolds number of $\mathrm{Re}_\lambda = 100$, it is obtained that $\frac{h}{\eta_k} = 4$, and the parameters are set to $\alpha_n = 0.05$ and $m = 1.161$. It is considered that an index of quality greater than 0.8 signifies a good LES while 0.95 and higher index values signify a DNS. The highest resolution in case 4 corresponds to an index value of 0.58, while for cases 5 and 6 it is about 0.76. Although LES is below the recommended index values, it is important to remind that the objective of the current study is to test the ability of LES simulations to capture the large scale properties of grid-generated turbulence with moderate number of mesh cells in order to decrease the computational cost.

6.3.2 Numerical solver methodology

In this study LES simulations are carried out using a finite volume solver which employs a finite volume method (FVM) for solving the incompressible Navier-Stokes equations within transient assumptions. In the present FVM method, the solution domain is subdivided into a finite number of continuous control volume (CV), and the non-linear conservation equations are transformed into analogous algebraic equations for each CV and these equations are solved by a segregated solution algorithm. Specifically the Semi-Implicit Method for Pressure Linked Equations (SIMPLE) pressure velocity coupling scheme is used for the present numerical fluid flow solver.

The resultant scalar system of equations for the dependent variable in each cell with a second order implicit time integration scheme. These transient computations for the LES method are then performed for long time-average solutions of flow past the grid, so that all statistics for the LES computations are averaged over a period of at least ten cycles, being a cycle the mean time that a fluid particle takes to travel along the total length of flow domain $t = x/U$ (where x is the flow domain length and U is the mean reference velocity at the inflow boundary). The size of one time step Δt is assigned to obtain a maximum Courant number $Co = U\Delta t/\Delta x = 1$, where Δx is the grid resolution

of the different mesh cases tested in Table 6.3. The solution convergence criterion is set to 0.001 for all solution variables.

Table 6.5 summarizes the simulation plan followed. First, cases 1 to 4 are computed for the same mesh resolution in order to analyze the inflow turbulence generation with respect to their capability for capturing turbulence structures. Then, a mesh sensitivity analysis for LES simulations (cases 4 to 6) is performed to assess the accuracy of the present LES solutions depending on the mesh resolution. Simulations are performed in double precision with up to a total of 8 processors (double core 2.40 GHz Intel Xeon E5620 and 32 GB RAM) using parallel computing technology.

Table 6.5: Simulation plan

Case	Number of cells	Iterations per time step	AWCT[1] per iteration (s)	TWCT[2] per mean flow residence time (h)
1	2864640	28	7.045	21.91
2	2864640	27	7.811	23.43
3	3148530	21	7.497	17.49
4	3568520	25	9.811	27.25
5	8985600	27	20.890	62.67
6	9853560	32	21.525	76.53

[1]Averaged Wall-Clock Time
[2]Total Wall-Clock Time

As it can be expected for cases 5 and 6, the computational cost increases significantly when the mesh resolution is higher. As stated by Blackmore *et al.* [158], projecting the grid pattern in the inlet boundary (case 3) leads to a lower computational time, as the cell count decreases compared to placing the grid downstream of the inlet (case 4). It is noteworthy that case 3 costs even less computational time than synthetic inlets (cases 1 and 2), where less computational cells are adopted due to the smaller domain size. Synthetic inlets require higher number of iterations per time step, which leads to a slower convergence of the solution.

6.3.3 Results and discussions

The numerical results obtained from all cases are presented in both qualitative and quantitative manner in comparison with the experimental data obtained under the same flow conditions [126]. Figure 6.9 shows the locations where data are extracted.

All cases share the same Cartesian coordinate system with a common origin, in which X is the streamwise direction starting just downstream of the grid, and Y and Z are

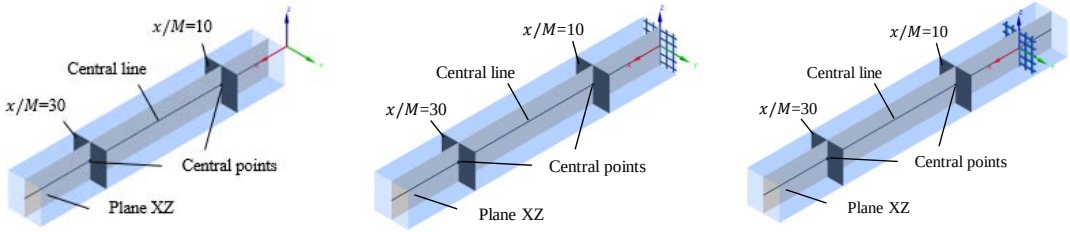

(a) Cases 1 and 2 (b) Case 3 (c) Cases 4-6

Figure 6.9: Locations for the data extraction

the other two orthogonal directions. As qualitative information, contour plots on the XZ plane as well as cross-stream planes situated in the near-field (x/M=10) and far-field (x/M= 30) are provided. Quantitatively, different variables (mean velocity profile, decay of the turbulence intensity and growth of the length scales) are represented along the central line of the wind tunnel. In addition, turbulence kinetic energy spectra is obtained at discrete points placed at the center of the cross-stream planes x/M=10 and x/M=30.

6.3.3.1 Comparison between turbulent inflow generation methods

Next, the results obtained with different turbulent inflow generation methods are discussed. Figure 6.10 shows the contour plot of u velocity obtained at $t = 5$ s. It can be said that the velocity fluctuations obtained for synthetic methods (case 1 and 2) are not too far from the mean so they cannot reproduce the highly turbulent intensities that exist in the near field region. They miss the phase information of the large scale eddies where the energy is contained, so they are quickly dissipated. An extra flow development section would be required to regenerate the large scale turbulent eddies just before the flow-structure interaction area. A very good time scale and finer mesh resolution may capture the summation of the developing turbulence after the inlet boundary condition, increasing the overall computational cost of the solution.

In order to analyze how the flow restores the homogeneity, the cross-stream cuts of the instantaneous velocity components at planes $x/M = 10$ and $x/M = 30$ for cases 1-4 are provided in Figures 6.11, 6.12 and 6.13. The contour plots of u, v and w are the velocity components in the X, Y and Z directions, respectively. Case 1 shows inhomogeneities on the left side due to the developing turbulence in x direction, and this effect is less significant in the far field. The artificial vortex points generated at the inlet are not able to reproduce a reliable turbulent inflow domain with the current mesh resolution employed. In case 3 the solid patch at the inlet generates a visible pattern that recreates the grid for

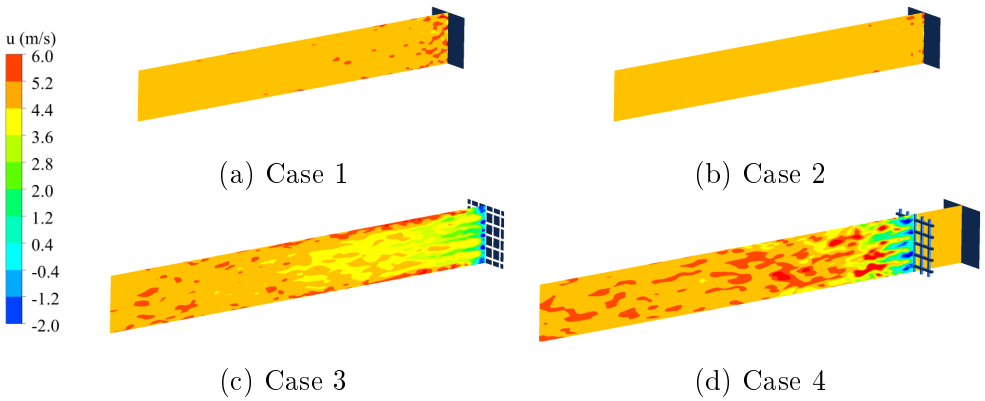

Figure 6.10: Instantaneous u velocity contour plot extracted for the XZ plane at t =5 s.

$x/M = 10$ cut. Cases 1-3 do not represent realistic turbulent structures for none of the velocity contour plots, as the flow is nearly homogeneous in both near-field and far-field. As noted previously, the velocity contour plots of grid-generated turbulence reproduce more realistic turbulent structures compared to synthetic inlets. Case 4 reproduces an inhomogenous field with velocities varying from 6 m/s to even 4 m/s. In both cases the flow is almost settled down for $x/M = 30$, where it is assumed that HIT conditions are satisfied [20]. Concerning the lateral velocity components, a major inhomogeneity exists for case 4, specially at near-field where values up to 1 m/s are reached. It is therefore believed that more natural turbulent inflow conditions are reproduced with the inclusion of the grid as a part of the domain instead of generating solid patches at the inlet.

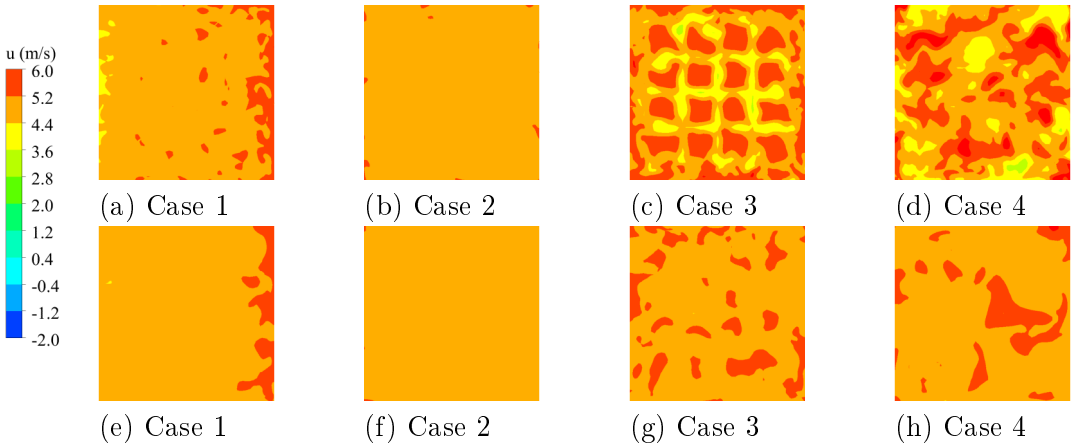

Figure 6.11: Instantaneous u velocity contour plots obtained at different cross-stream planes at $t = 5$ s ((a)-(d):$x/M = 10$,(e)-(h):$x/M = 30$.

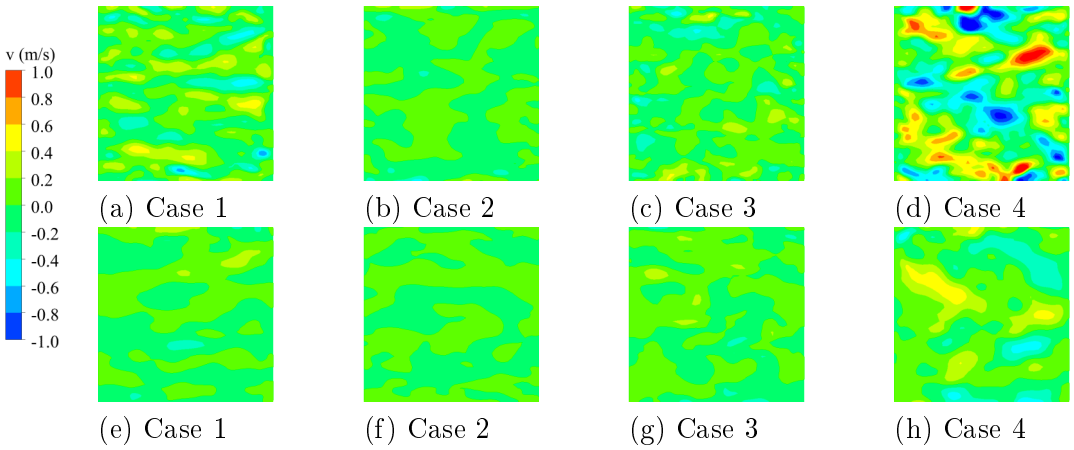

(a) Case 1 (b) Case 2 (c) Case 3 (d) Case 4

(e) Case 1 (f) Case 2 (g) Case 3 (h) Case 4

Figure 6.12: Instantaneous v velocity contour plots obtained at different cross-stream planes at $t = 5$ s ((a)-(d):$x/M = 10$,(e)-(h):$x/M = 30$.

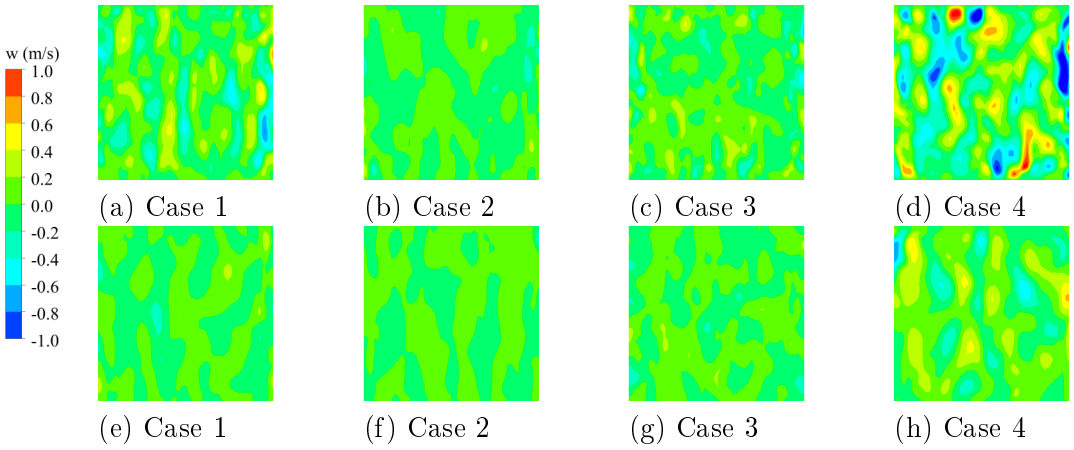

(a) Case 1 (b) Case 2 (c) Case 3 (d) Case 4

(e) Case 1 (f) Case 2 (g) Case 3 (h) Case 4

Figure 6.13: Instantaneous w velocity contour plots obtained at different cross-stream planes at $t = 5$ s ((a)-(d):$x/M = 10$,(e)-(h):$x/M = 30$.

Figure 6.14(a) shows the mean velocity profile along the streamwise direction. In Figure 6.14 (b) the decay of turbulence intensity is plotted as a function of the streamwise length x, which is normalized by the mesh size M. Turbulence intensity is obtained as the standard deviation of the fluctuations (normalized by the velocity in the free-stream U). The instantaneous velocity component u for each location of the central line is recorded at each time step. Then, the standard deviation of the velocity signal for each location is computed by the root-mean squared $u_{rms} = \sqrt{\overline{u'^2}}$, and turbulence intensity is calculated as $I = u_{rms}/U$. Only u velocity component is plotted for a comparison with the available experimental data.

The mean velocity profile in cases 1 and 2 cannot be distinguished. Since there is no obstacle in the domain acting as a turbulence generation mechanism, i.e. wall-generated turbulence, both cases present a constant value that coincides with the uniform

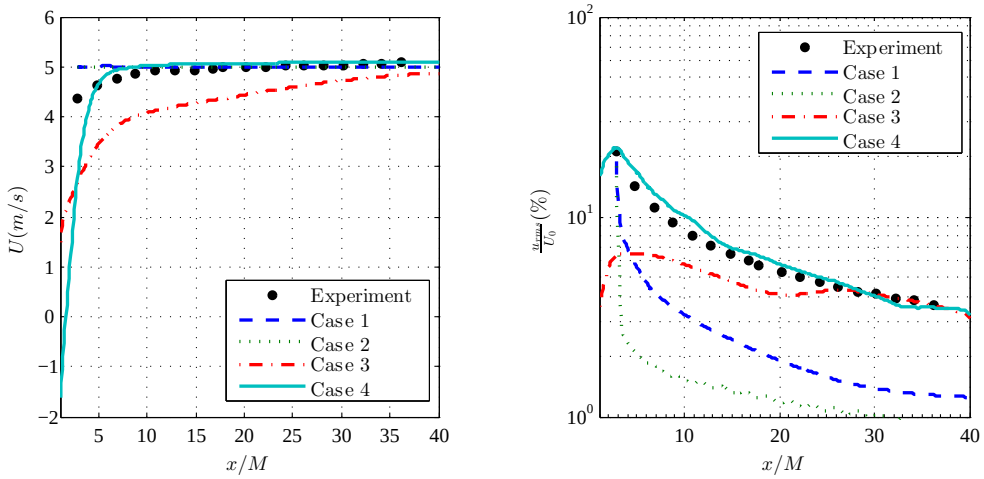

(a) (b)

Figure 6.14: Effect of turbulent inflow generation method on mean velocity profile and turbulence intensity along the central line of the wind tunnel with distance downstream of the grid. (a) Mean velocity profile (b) Turbulence Intensity

inlet velocity. In case 3 the solid patch which is used in the uniform inlet does have influence on the mean velocity profile, and reproduces a similar velocity profile compared with the experimental data but with lower values. In contrast, case 4 shows better correspondence with the experimental data. This better behavior can be attributed to the near wall treatment employed in the solid boundary of the grid. As case 4 does include a wall boundary condition, the production of turbulence is developed with more realistic physical properties. The solid patch employed in case 3 has no structural information, and thus, the flow does not represent the real eddies generated by the grid.

This behavior is also noticed in the turbulence intensity decay shown in Figure 6.14(b). Case 3 obtains a good agreement in far field region ($x/M > 30$) but the underestimation in the production of turbulence at the solid patch leads to a poor result in the near field region. On the other hand, case 4 produces more realistic turbulent structures at the grid walls that are sustained along the streamwise direction and fits the experimental data with acceptable accuracy, even for the high intensity rates given in the near field region. The behavior of synthetic inlets decays rapidly as it is anticipated, due to the lack of a turbulence mechanism to generate large integral scale eddies. A longer development section would be required in order to allow the generation of organized turbulent motion.

The turbulence energy dissipation rate ϵ can be defined as $\epsilon = -dk/dt$ in the reference frame moving at the mean velocity U, or equivalently $\epsilon = -Udk/dx$ in the reference frame

of the laboratory, using a Taylor hypothesis where the streamwise spatial coordinate x in the laboratory frame is simply related to the time variable t in the moving frame by $x = Ut$. If the isotropy condition is satisfied then $k = \frac{3}{2}u_{rms}^2$ and the turbulence kinetic energy dissipation rate can be rewritten as $\epsilon = \frac{3}{2}\frac{du_{rms}^2}{dx}U$. Once it is determined, most of the relevant turbulent length scales can be easily estimated, such as the integral scale $L = \frac{u_{rms}^3}{\epsilon}$, the Taylor micro-scale $\lambda = \sqrt{\frac{15\nu u_{rms}^2}{\epsilon}}$ and the dissipation scale $\eta = \sqrt[4]{\nu^3/\epsilon}$. Figure 6.15 shows the downstream evolution of the turbulence length scales.

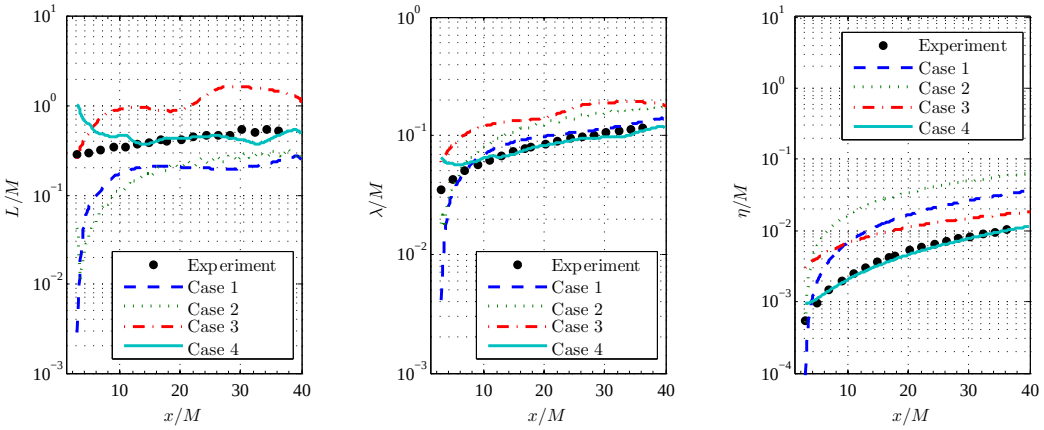

Figure 6.15: Effect of turbulent inflow generation method on turbulent length scales along the central line of the wind tunnel with distance downstream of the grid. (a) Evolution of integral length scale (b) Evolution of Taylor length scale (c) Evolution of dissipative length scale

It should be noted here that the integral length scale L in this comparative figure is obtained based on the decay of the energy dissipation rate ϵ, rather than being estimated from correlation function of the velocity. The reason for this is the difficulties encountered when obtaining the auto-correlation function of the velocity signals produced by LES simulations due to the simulation time employed, which is set to 5 seconds for more than 10 cycles. More cycles would be required for the integral length scale to converge as demonstrated by Blackmore *et al.* [158]. However, as mentioned in Section 3.10, in stationary conditions, the energy injection scale L and the energy dissipation rate ϵ are simply related by dimensional considerations: $\epsilon = Du_{rms}^3/L$, where D is a dimensionless constant of order 1 [127]. Regarding the results plotted in Figure 6.15, it is observed that case 3 overestimates the values for all length scales. Cases 1 and 2 show peak near the inlet and underestimate the integral length scale, while higher values are obtained for Taylor and dissipative length scales. Case 2 shows a better agreement for Taylor microscale when compared to the experimental data. In contrast, case 4 reproduces with higher accuracy

the evolution turbulent scales, except for the near-field region (x/M <10), where the isotropy condition is not satisfied [20].

In order to complete the validation of the proposed method, Figure 6.16 shows the energy spectra for cases 1-4. The energy is obtained via the power spectral density (PSD) estimate of the u velocity signal at near field region ($x/M = 10$) and far field region ($x/M = 30$). In general, the energy spectra of the simulations capture the $-5/3$ slope of the Kolmogorov law in the inertial subrange until the filter cut-off frequency, which is around 100 Hz. At higher frequencies the energy spectra deviates from the $-5/3$ slope and turbulent fluctuations are no longer resolved. It can be seen that the energy contained in the low frequencies is higher for case 4 at $x/M = 10$ compared to the rest of the cases. Cases 2 and 3 reproduce closer energy levels and case 2 underestimates the energy content. A very similar energy spectra is observed in cases 3 and 4 at $x/M = 30$.

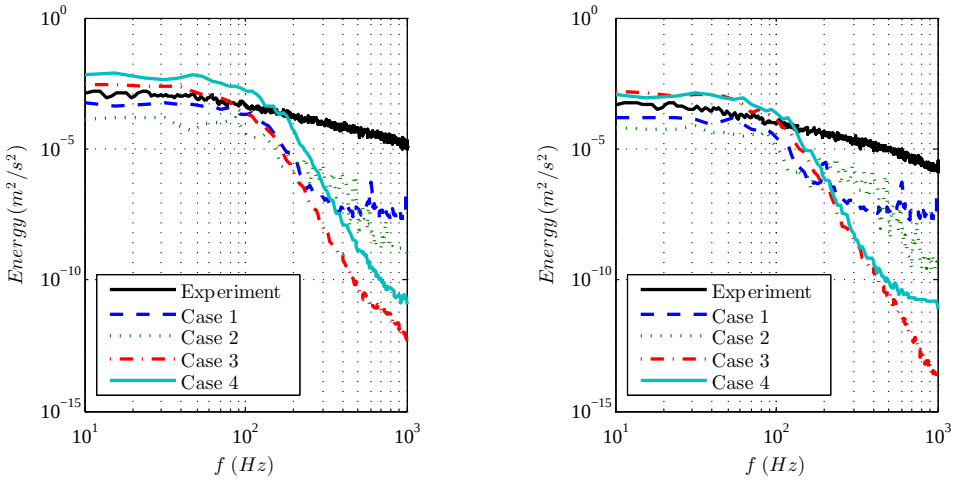

Figure 6.16: Energy spectrum of the turbulent inflow generation methods. (a) $x/M = 10$ (b) $x/M = 30$

6.3.3.2 LES mesh resolution sensitivity analysis

Due to the constant C_s value, boundary/initial conditions and solution methods utilized for all LES solutions, the uncertainty analysis is addressed only to mesh dependent parametric studies, more specifically, to sensitivity to the mesh resolution.

As a preliminary qualitative analysis, Figure 6.17 shows the vorticity iso-surfaces obtained for cases 4 to 6. It is observed that size of the eddies are in the range of the mesh element size employed. Thus, case 5 and 6 can more successfully capture smaller structures than case 4.

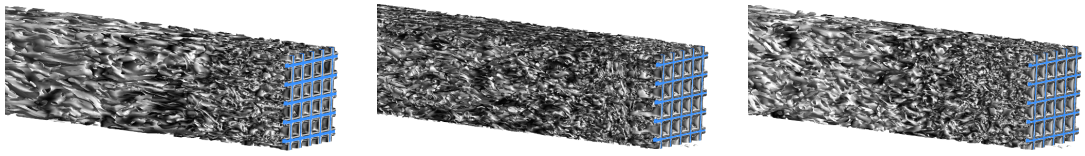

(a) Case 4 (b) Case 5 (c) Case 6

Figure 6.17: Iso-surfaces of vorticity contours for a constant value of 60 s^{-2} obtained by Q-criterion.

Figure 6.18(a) represents the predicted decay of turbulence intensity as a function of the model length for different mesh densities. It is generally seen from these figures that the simulation results are generally consistent with the experimental data.

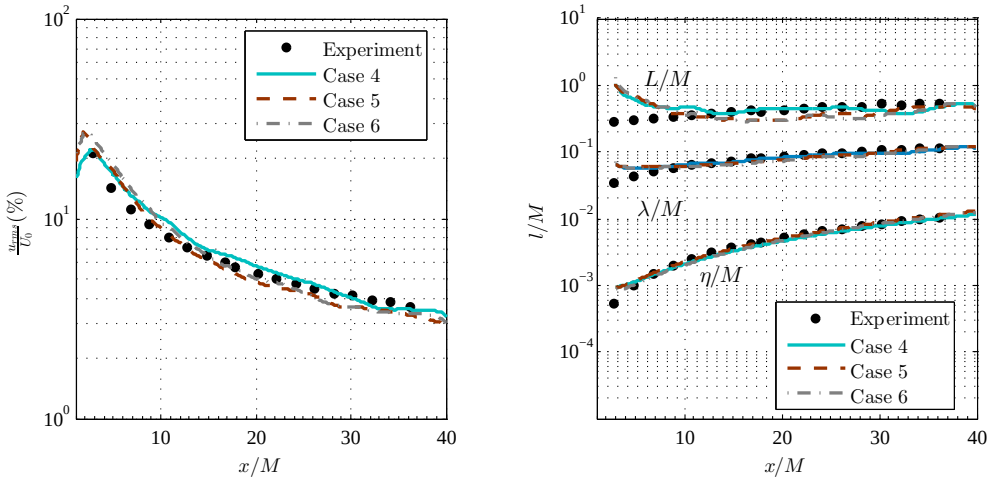

(a) (b)

Figure 6.18: Effect of mesh resolution on turbulence intensity and length scales along the central line of the wind tunnel with distance downstream of the grid. (a) Turbulence intensity (b) Variations of L, λ and η

Both numerical simulations and the experimental data reproduce similar tendency of loss of turbulence intensity except for more pronounced values obtained in the near field region where $x/M = 2$ in cases 4 and case 5. It is seen that case 3 reproduces similar results to the experiments, in spite of having a greater mesh size in this zone. Moreover, employing a wall resolved LES technique in case 5 with higher computational effort does not guarantee better predictions than other cases, where the logarithmic law-of-the-wall with appropriate wall y^+ values reproduces closer results compared to the experimental data. In Figure 6.18(b), the turbulence length scales (L, λ and η) increase and show a good agreement with experimental data once turbulence is generated, except for the

region where $x/M < 10$, as it is expected due to the anisotropy due to the lack of isotropy. All simulations show that L is still decreasing until $x/M = 20$, while the experimental profile grows with a power law evolution.

Another way to assess the effects of mesh resolution on the simulation is through the turbulence kinetic energy spectra. Figure 6.19 shows the one-dimensional turbulence kinetic energy spectra E in terms of the frequency f.

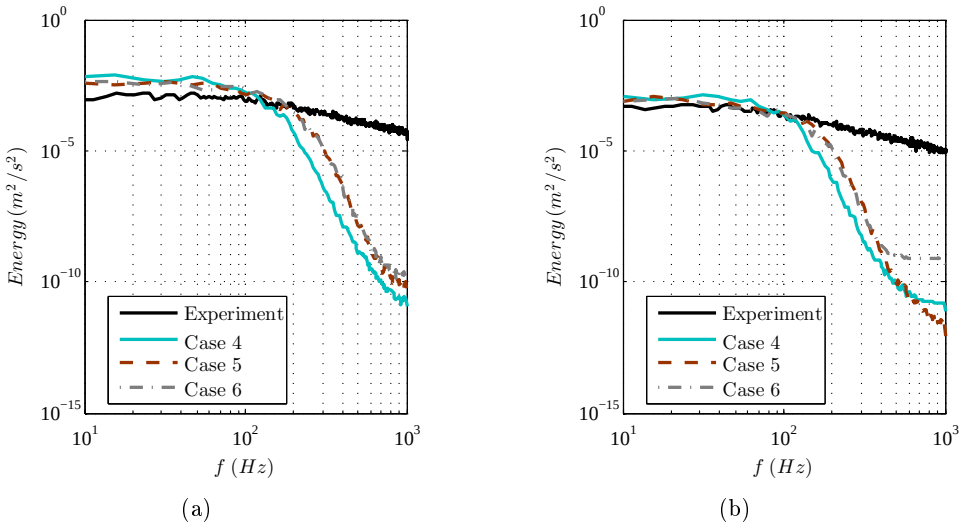

Figure 6.19: Effect of mesh resolution in energy spectra. (a) $x/M = 10$ (b) $x/M = 30$

The calculated spectra present similar features for the low wavenumbers. It can be appreciated also a good agreement with the $-5/3$ slope prior to the deviation that starts after the filter cut-off frequency. In contrast, poorer resolution is achieved at high frequencies, as might be expected due to the use of SGS turbulence model. Cases 4 and 5 have a wider spectra, which means that a higher portion of the length scales is captured as corresponds to the lower filter size employed in these cases. However, small scale fluctuations of the incoming flow do not affect in a significant manner the drag or lift loads, flow separation or wake dissipation for bluff bodies with fixed separation points [143]. The overall energy contained in the turbulent fluctuations certainly recreates the free-stream or even higher inflow turbulence levels and affects the performance of devices working under these conditions. Therefore, the results presented in this study reproduce a reliable compromise between computational cost and accuracy.

6.4 Conclusions

The aim of the current chapter is to use the proposed grid-generated turbulence technique to produce turbulent inflow conditions for its use in airfoil simulations at low Re numbers.

In order to reach this objective, a numerical model is tested in Section 6.2 to simulate the airfoil performance at different angles under smooth inflow conditions. The results are in good agreement when compared to experiments and Xfoil calculations for angles with low to medium separation regions. For higher angles of attack the agreement is less consistent, illustrating acknowledged difficulties associated with simulating massively separated flows. The simulations are based on 2D assumptions to reduce the computational cost. Due to the three dimensional nature of laminar separation bubbles, a 3D simulation with periodic boundary conditions on the spanwise boundaries could be considered. By resolving the small spanwise structures more accurate results may be achieved.

Regarding the proposed inflow generation method, the results obtained in Section 6.3 present a reliable compromise between computational cost and accuracy. This precomputation method can be employed for generating medium-high turbulent inflow conditions at low Re numbers by introducing the grid as a part of the computational domain, while different levels of turbulence intensity can be achieved by controlling the distance between the grid and the device to be analyzed.

Since LES resolves the large scales from the free flow, it reproduces the desired mixing and with the flow in the boundary layer, where the transition model is active. The interactions of the resolved mean flow fluctuations may alter the correlations employed in the intermittency-based one-equation transition model (γ model) to predict the transition point. This represents a promising approach to numerically study the effect of turbulent inflow conditions on airfoil performance, which is one of the main limitations of the numerical methods for modelling turbulence.

Chapter 7

Conclusions and future lines

As an overall conclusion, it can be said that the principal and auxiliary objectives of the project have been satisfactorily achieved. The constructed low-speed wind tunnel (LSWT) test facility at MU meets the aerodynamic flow quality requirements for the experimental testing of airfoils at low Re numbers. The airfoil performance data measurements have been compared with similar studies found in literature to asses their reliability. In spite of the differences caused by the defects detected in the airfoil due to the manufacturing process, the results are consistent with previous investigations. Therefore, it is believed that the current experimental methodology is validated.

In addition, the passive grid employed has permitted to successfully reproduce different free-stream turbulence levels at the inlet of the test section. It can be concluded that inflow turbulence has a significant impact on the lift curve and should be considered to obtain higher energy conversion efficiency of wind turbines operating inside the ABL or behind the wake of other wind turbines.

The ability of RANS simulations to capture the large scale properties (rms velocity, turbulence intensity, turbulence decay and pressure drop) of the turbulence downstream a passive grid is within an acceptable accuracy (relative error below 10 % for the decaying zone), in spite of modelling all the energy spectrum. RANS solutions can be used as a design tool for grids, without recurring to empirical laws. This way, parametric studies can be performed using RANS solutions in order to obtain the effect of design parameters (for instance solidity, size, mesh size and number of rods) on the turbulent flow field.

Regarding LES solutions, it is demonstrated that a relatively coarse mesh with the use of a near-wall modelling technique in the context of grid-generated turbulence achieve an acceptable accuracy when compared to experimental data. Due to the lower computational requirements compared to other precursor simulation methods, they also offer a cost effective solution to generate turbulent inflow conditions for their use in different

aerodynamic applications at low Re numbers. For instance, this method can be combined with detached eddy simulations (DES) for simulating airfoil flows under high intensity turbulence levels. This simulations represent a promising approach to numerically study the effect of turbulent inflow conditions on airfoil performance, which is one the main limitations of the numerical methods for modelling turbulence.

7.1 Future lines

The instrumentation installed on the LSWT has permitted to obtain valuable data of the flow properties through the test section. In the next future, hot-wire anemometry can be included to analyze a wider energy spectrum of the turbulent fluctuations. A velocity sensor will be installed permanently in the test section to make a more robust control of the wind speed in the test section. The signal coming from that velocity sensor will be used to feed the set point for the variable frequency controller of the fan in a closed-loop control scheme. Similarly, the same control system will be applied to the 3D traverse system and the rotary table. The signal coming from external linear and angular sensors will be used to position the probe with virtually no error.

Concerning the study of airfoils at low Re numbers, the study can be completed with surface pressure measurements and/or surface flow visualizations to shed light on the formation of laminar separation bubbles. In order to increase the admissible Re number that can be measured with the force balance arrangement, a new dynamometer KISTLER 9119A will be installed which has a measuring range up to 4 KN maintaining a high resolution.

The experimental tests of airfoils in turbulent inflow conditions could be also repeated with the use of active grids. These kind of grids are of particular interest because they are able to produce high Re wind tunnel turbulence that can be used to approximate conditions similar to those experienced in the atmosphere. Regarding the numerical approach, new simulations of grid-generated turbulence can be investigated. Different topologies such as fractal grids or even active grids could be studied to generate turbulence.

Finally, the present work could be completed with a DES-γ simulation of the NACA0021 in turbulent inflow. The grid could be introduced as a part of the numerical model, as proposed in Chapter 6. This inflow generation method in conjunction with the airfoil situated at the required distance could be investigated in order to compare with the performed experimental study.

Bibliography

[1] S1MA - Continuous-flow wind tunnel, Atmospheric, Mach 0.05 to Mach 1, feb.

[2] Jewel B. Barlow, William H. Rae, and Alan Pope. *Low-Speed Wind Tunnel Testing.* Wiley-Interscience, 1999.

[3] G. Falkovich. *Fluid Mechanics, a short course for physicists.* Cambridge University Press, 2011.

[4] GBRL Capabilities.

[5] T. Morel. Comprenhensive Design of Axisymetric Wind tunnel Contactions. *Journal of Fluids Engineering*, 97:225–233, 1975.

[6] K D Jensen. Flow measurements. *Journal of the Brazilian Society of Mechanical Sciences and Engineering*, 26(4):400–416, 2004.

[7] TFI - Cobra Probe.

[8] Serhiy Yarusevych, Pierre E. Sullivan, and John G. Kawall. On vortex shedding from an airfoil in low-Reynolds-number flows. *Journal of Fluid Mechanics*, 632:245, 2009.

[9] Joseph Katz and Allen. Plotkin. *Low-speed aerodynamics : from wing theory to panel methods.* McGraw-Hill, 1991.

[10] Leon Li. *Experimental Testing of Low Reynolds Number Airfoils for Unmanned Aerial Vehicles.* PhD thesis, University of Toronto, 2013.

[11] Michael S. Selig. Low Reynolds Number Airfoil Design Lecture Notes - Various Approaches to Airfoil Design. (November):24–28, 2003.

[12] G. K. Ananda, P. P. Sukumar, and M. S. Selig. Measured aerodynamic characteristics of wings at low Reynolds numbers. *Aerospace Science and Technology*, 42:392–406, 2015.

[13] Cameron Tropea, Alexander L. Yarin, and John F. Foss. *Springer Handbook of Experimental Fluid Mechanics*, volume 1. 2007.

[14] P B S Lissaman. Low-Reynolds-Number Airfoils. *Annual Review of Fluid Mechanics*, 15(1):223–239, jan 1983.

[15] Alain Pelletier and Thomas J. Mueller. Effect of Endplates on Two-Dimensional Airfoil Testing at Low Reynolds Number. *Journal of Aircraft*, 38(6):1056–1059, 2001.

[16] Paul Manneville. *Instabilities, chaos and turbulence*. Imperial College Press, volume 1 edition, 2010.

[17] Kemal Hanjalić and Brian Launder. *Modelling Turbulence in Engineering and the Environment: Second-Moment Routes to Closure*. Cambridge University Press, 2011.

[18] SG Saddoughi and SV Veeravalli. Local isotropy in turbulent boundary layers at high Reynolds number. *Journal of Fluid Mechanics*, 268:333–372, 1994.

[19] Roland B. Stull. *An Introduction to Boundary Layer Meteorology*. Springer, 1988.

[20] Stephen B. Pope. *Turbulent Flows*. Cambridge University Press, 2000.

[21] Uriel Frisch and AndreÄ Nikolaevich Kolmogorov. *Turbulence: The Legacy of A. N. Kolmogorov*, volume 0. Cambridge University Press, volume 1 edition, 1995.

[22] By Genevifive Comte-bellott and Stanley Corrsin. The use of a contraction to improve the isotropy of grid-generated turbulence. *Journal of Fluid Mechanics*, 25:657–682, 1966.

[23] Jesus Manuel Fernandez Oro. *Técnicas numéricas en ingeniería de fluidos*. Editorial Reverte, 2012.

[24] F.L. Wattenford. Factors Influencing the Energy Ratio of Return Flow Wind Tunnels. In *Fifth International Congress for Applied Mechanics*, page 52, Cambridge, 1938.

[25] W.T. Eckert, K.W. Mort, and J. Jope. Aerodynamic design guidelines and computer program for estimation of subsonic wind tunnel performance. *NASA Technical Note TN D-8243*, 1976.

[26] L Prandtl. Attaining a steady air stream in wind tunnels. *NACA TM 726*, 1933.

[27] James Scheiman and J D Brooks. Comparison of Experimental and Theoretical Turbulence Reduction from Screens, Honeycomb, and Honeycomb-Screen Combinations. *Journal of Aircraft*, 18(8):638–643, aug 1981.

[28] RD Mehta and P Bradshaw. Design rules for small low speed wind tunnels. *Aeronautical Journal*, 1979.

[29] P. Bradshaw. The effect of wind-tunnel screens on nominally two-dimensional boundary layers. *Journal of Fluid Mechanics*, 22(04):679–687, aug 1965.

[30] P.G. Morgan. The Stability of Flow Through Porous Screens. *Journal of the Royal Aeronautical Society*, 64:359, 1960.

[31] I.E. IdelÂ´Chik. *Handbook of hydraulic Resistance*. The Israel Program for Scientific Translations, AEC-TR-6630, Tel Aviv, 1966.

[32] Johan Groth. *On the Modelling of Homogeneous Turbulence*. Deparment of Mechanichs, KTH, SE-100 44, Stockholm, 1991.

[33] Eli Reshotko, William Saric, and Hassan Nagib. Flow quality issues for large wind tunnels. In *35th Aerospace Sciences Meeting and Exhibit*, Aerospace Sciences Meetings. American Institute of Aeronautics and Astronautics, jan 1997.

[34] Johan Groth and Arne V. Johansson. Turbulence reduction by screens. *Journal of Fluid Mechanics*, 197:139–155, apr 1988.

[35] G E Chmielewski. Boundary-Layer Considerations in the Design of Aerodynamic Contractions. *Journal of Aircraft*, 11(8):435–438, aug 1974.

[36] M. N. Mikhail. Optimum Design of Wind Tunnel Contractions. *AIAA Journal*, 17(5):471–477, may 1979.

[37] B. S. Stratford. The prediction of separation of the turbulent boundary layer. *Journal of Fluid Mechanics*, 5(01):1–16, mar 1959.

[38] RD Mehta and JH Bell. Boundary-layer predictions for small low-speed contractions. *AIAA Journal*, 27(3):372–374, 1989.

[39] Thomas Morel. Design of Two-Dimensional Wind Tunnel Contractions. *Journal of Fluids Engineering*, 99(2):371–377, jun 1977.

[40] Daniel Brassard. *Transformation of a Polynomial for a Contraction Wall Profile*. Lakehead University, Ontario, Canada, 2003.

[41] RD Mehta and JH Bell. *Contraction Design for small low-speed wind tunnels.* Number April. Deparment of Aeronautics and Astronautics, CA 94305, Stanford University, 1988.

[42] J E Sargison, G J Walker, and R Rossi. Design and calibration of a wind tunnel with a two dimensional contraction. In *15th Australasian Fluid Mechanics Conference*, number December, page 4, 2004.

[43] Craig A Zehrung. *Comparative analysis of a low-speed wind tunnel designed for renewable energy applications.* PhD thesis, 2011.

[44] I Torrano, M Martinez-Agirre, and M Tutar. Numerical characterization of pressure drop through a low speed wind tunnel: Some design aspects. In *Renewable and Sustainable Energy Conference (IRSEC)*, pages 240–245, Ouarzazate, Morocco, 2013.

[45] María Rodríguez Lastra, Jesús Manuel Fernández Oro, Mónica Galdo Vega, Eduardo Blanco Marigorta, and Carlos Santolaria Morros. Novel design and experimental validation of a contraction nozzle for aerodynamic measurements in a subsonic wind tunnel. *Journal of Wind Engineering and Industrial Aerodynamics*, 118:35–43, 2013.

[46] Leifur Leifsson and Slawomir Koziel. Simulation-driven design of low-speed wind tunnel contraction. *Journal of Computational Science*, 7:1–12, 2015.

[47] Ernest Brater, Horace King, James Lindell, and C. Wei. *Handbook of Hydraulics.* McGraw-Hill Publishing Co., 7 edition, 1996.

[48] I.H. Shames. *Mechanics of Fluids.* McGraw-Hill Publishing Co., New York, 3 edition, 1992.

[49] I. C. Shepherd. A Four Hole Pressure Probe for Fluid Flow Measurements in Three Dimensions. *Journal of Fluids Engineering*, 103(4):590, dec 1981.

[50] F. Kevin Owen and Andrew K. Owen. Measurement and assessment of wind tunnel flow quality. *Progress in Aerospace Sciences*, 44(5):315–348, 2008.

[51] National Wind Tunnel Complex, Facilities Study Office, Criteria and Requirements Document for Concept D-Option 5. Final Report. Technical report, 1993.

[52] Michael S. Selig, Robert W. Deters, and Gregory A. Williamson. Wind Tunnel Testing Airfoils at Low Reynolds Numbers. In *49 th AIAA Aerospace Sciences Meeting*, number 875, pages 1–32, Orlando, FL.

[53] Christophe Sicot, Sandrine Aubrun, Stephane Loyer, and Philippe Devinant. Unsteady characteristics of the static stall of an airfoil subjected to freestream turbulence level up to 16%. *Experiments in Fluids*, 41(4):641–648, 2006.

[54] Ph Devinant, T. Laverne, and J. Hureau. Experimental study of wind-turbine airfoil aerodynamics in high turbulence. *Journal of Wind Engineering and Industrial Aerodynamics*, 90(6):689–707, 2002.

[55] Benjamin Olle Johnson and Louis Cattafesta. *A Multi-Holed Pressure Probe Accuracy Analysis*. PhD thesis, University of Florida, 2012.

[56] Ivan Torrano, Manex Martinez-Agirre, and Alain Martin. Control and Aerodynamic Data Acquisition System for the Wind Tunnel at Mondragon University, 2016.

[57] Björn Lindgren and Arne V Johansson. Design and Evaluation of a Low-Speed Wind-Tunnel with Expanding Corners. Technical Report October, Royal Institute of Technology, Stockholm, 2002.

[58] Hermann Schlichting and K. Gersten. *Boundary-layer theory*. Springer, 8 edition edition, 2000.

[59] M. Gaster. The Structure and Behaviour of Laminar Separation Bubbles. *Aeronautical Research Council Reports and Memoranda*, (3595):1–31, 1967.

[60] B. H Carmichael. Low Reynolds number airfoil survey. Technical report, NASA Contractor Report 165803, 1981.

[61] Michaels Selig, James J Guglielmo, Andy P Broeren, and Philippe Giguere. *Summary of Low-Speed Airfoil Data*, volume 1. 1995.

[62] Zifeng Yang, Hirofumi Igarashi, Mathew Martin, and Hui Hu. An experimental investigation on aerodynamic hysteresis of a low-Reynolds number airfoil. In *AIAA Paper 2008-0315, 46th Aerospace Sciences Meeting and Exhibit*, pages 1–11, 2008.

[63] By I R A H Abbott. *Theory Of Wing Sections*.

[64] UIUC Airfoil Data Site.

[65] K L Hansen and R M Kelso. Laminar Separation Effect on the Lift Curve Slope of an Airfoil. In *19th Australasian Fluid Mechanics Conference*, pages 5–8, Melbourne, Australia.

[66] S. Ristic. Flow Visualisation Techniques in Wind Tunnels Part I - Non optical Methods. *Scientific Technical Review*, LVII(1):39–50, 2007.

[67] Gk Ananda, Pp Sukumar, and Ms Selig. Low-to-Moderate Aspect Ratio Wings Tested at Low Reynolds number. In *30th AIAA Applied aerodynamics Conference*, number 3026, pages 1–19, New Orleans, Louisiana.

[68] W.a. Timmer. Two-dimensional low-Reynolds number wind tunnel results for airfoil NACA 0018. *Wind Engineering*, 32(6):525–537, 2009.

[69] F Kevin Owen, T Kevin Mcdevitt, D G Morgan, Moffett Field, and Andrew K Owen. Wind Tunnel Model Angle of Attack Measurements using an Optical Model Attitude System. In *38th Aerospace Sciences Meeting & Exhibit*, number 0414, Reno , NV, 2000.

[70] Miguel a González, José Miguel Ezquerro, Victoria Lapuerta, Ana Laverón, and Jacobo Rodríguez. Components of a Wind Tunnel Balance: Design and Calibration. *Wind Tunnels and Experimental Fluid Dynamics Research*, pages 1–20, 2011.

[71] Thomas J Mueller and Stephen M Batil. Experimental Studies of Separation on a Two-Dimensional Airfoil at Low Reynolds Numbers. *AIAA Journal*, 20(4):457–463, apr 1982.

[72] Nilanjan Saha. *Gap Size Effect on Low Reynolds Number Wind Tunnel Experiments.* PhD thesis, 1999.

[73] *McGraw-Hill Dictionary of Scientific \& Technical Terms.* 6e edition, 2003.

[74] J.L. Tangler. Effects of Airfoil Thickness and Maximum Lift on Roughness Sensitivity. In *Third ASME-JSME Joint Fluid Engineering Conference*, page 4, San Francisco.

[75] Lance W. Traub. Effect of Rapid-Prototyped Airfoil Finish on Loading at Low Reynolds Numbers. *Journal of Aircraft*, 50(1):307–311, 2013.

[76] Lasse Gilling. *Airfoils in Turbulent Inflow.* PhD thesis, Aalborg Universitet, 2009.

[77] Jon a. Hoffmann. Effects of freestream turbulence on the performance characteristics of an airfoil. *AIAA Journal*, 29(9):1353–1354, 1991.

[78] John McArthur. *Aerodynamics of wings at low Reynolds numbers.* PhD thesis, University of Southern California, 2007.

[79] Michael S. H. Boutilier and Serhiy Yarusevych. Effects of End Plates and Blockage on Low-Reynolds-Number Flows Over Airfoils. *AIAA Journal*, 50(7):1547–1559, 2012.

[80] Aditya Vaidyanathan, David Kingman, and Theresa Kurth. When Do Endplates Work? In *52nd Aerospace Sciences Meeting*, pages 1–11, 2014.

[81] I I I J. Marchman, C Gunther, and I V J. Gundlach. Semi-span testing at low Reynolds number. In *36th AIAA Aerospace Sciences Meeting and Exhibit*, Aerospace Sciences Meetings, Reno , NV, jan 1998. American Institute of Aeronautics and Astronautics.

[82] Jeff M Diebold, Brian S Woodard, Marianne C Monastero, and Michael B Bragg. Experimental Study of Splitter Plates for Use with Semispan Wing Models. In *53rd AIAA Aerospace Sciences Meeting*, number 5-9 January, pages 1–14, Kissimmee, Florida, 2015.

[83] W.J. Graham. The Pressure-Drag due to Blunt Leading Edges on Two-Dimensional Aerofoils , at Transonic and Low-Supersonic Speeds. *Aeronautical and Research Rouncil Reports and Memoranda*, (3465), 1967.

[84] Marcel Lesieur. *Turbulence in Fluids*. Springer, vol 84. edition, 2008.

[85] Lewis Fry Richardson. *Weather Prediction by Numerical Process*. Cambridge University Press, 1922.

[86] AndreÄ Nikolaevich Kolmogorov. The local structure of turbulence in incompressible viscous fluid for very large Reynolds numbers. *Doklady Akademiia Nauk SSSR*, 30:299–303, 1941.

[87] J. O. Hinze. *Turbulence*. McGraw-Hill Publishing Co., New York, 1975.

[88] G Taylor. Statistical Theory of Turbulence. In *Proceedings of the Royal Society*, page 151, London, 1935.

[89] KR Sreenivasan. On the universality of the Kolmogorov constant. *Physics of Fluids*, (3), 1995.

[90] LD Landau. On the problem of turbulence. *Doklady Akademiia Nauk SSSR*, 44:339–342, 1944.

[91] Obukhov. Some specific features of atmospheric turbulence. *Journal of Fluid Mechanics*, 13:77–81, 1962.

[92] Ictr A Arneodo, R Benzi, J Berg, L Biferale, E Bodenschatz, A Busse, E Calzavarini, B Castaing, M Cencini, L Chevillard, R T Fisher, R Grauer, H Homann, D Lamb, A S Lanotte, E Leveque, B Luethi, J Mann, N Mordant, W C Mueller, S Ott, N T Ouellette, J F Pinton, S B Pope, S G Roux, F Toschi,

H Xu, and P K Yeung. Universal intermittent properties of particle trajectories in highly turbulent flows. *Physical Review Letters*, 100:254504, 2008.

[93] G Parisi. Fully developed turbulence and intermittency. In M Ghil, R Benzi, and G Parisi, editors, *Turbulence and Predictability in Geophysical Fluid Dynamics and Climate Dynamics*, pages 84–88, Amsterdam, 1985.

[94] G K Batchelor. *The theory of homogeneous turbulence*, volume 20. 1953.

[95] P. G. Saffman. The large-scale structure of homogeneous turbulence. *Journal of Fluid Mechanics*, 27(03):581, mar 2006.

[96] P.-Å. Krogstad and P. A. Davidson. Is grid turbulence Saffman turbulence? *Journal of Fluid Mechanics*, 642:373– 394, dec 2009.

[97] Antoine Llor. Langevin equation of big structure dynamics in turbulence: Landau invariant in the decay of homogeneous isotropic turbulence. *European Journal of Mechanics - B/Fluids*, 30(5):480–504, sep 2011.

[98] Z. Warhaft and J. L. Lumley. An experimental study of the decay of temperature fluctuations in grid-generated turbulence. *Journal of Fluid Mechanics*, 88(04):659–684, apr 1978.

[99] T. Ishida, P. A. Davidson, and Y. Kaneda. On the decay of isotropic turbulence. *Journal of Fluid Mechanics*, 564:455– 475, sep 2006.

[100] Nicolas Mordant. Experimental high Reynolds number turbulence with an active grid. *American Journal of Physics*, 76(12):1092, 2008.

[101] Hyung Suk Kang, Stuart Chester, and Charles Meneveau. Decaying turbulence in an active-grid-generated flow and comparisons with large-eddy simulation. *Journal of Fluid Mechanics*, 480:129–160, apr 2003.

[102] B. Mazzi and John Christos Vassilicos. Fractal-generated turbulence. *Journal of Fluid Mechanics*, 502(1):65–87, 2004.

[103] R E Seoud and J C Vassilicos. Dissipation and decay of fractal-generated turbulence. *Physics of Fluids*, 19(10):105–108, 2007.

[104] D. Hurst and J. C. Vassilicos. Scalings and decay of fractal-generated turbulence. *Physics of Fluids*, 19(3):035103, mar 2007.

[105] P.-Å. Krogstad and P. A. Davidson. Freely decaying, homogeneous turbulence generated by multi-scale grids. *Journal of Fluid Mechanics*, 680:417–434, 2011.

[106] I. Antoniou, D. Asimakopoulos, A. Fragoulis, A. Kotronaros, D.P. Lalas, and I. Panourgias. Turbulence measurements on top of a steep hill. *Journal of Wind Engineering and Industrial Aerodynamics*, 39(1-3):343–355, jan 1992.

[107] M. Noda and R.G.J. Flay. A simulation model for wind turbine blade fatigue loads. *Journal of Wind Engineering and Industrial Aerodynamics*, 83(1-3):527–540, nov 1999.

[108] K E Swalwell, J Sheridan, and W H Melbourne. The Effect of Turbulence Intensity on Stall of the NACA 0021 Aerofoil. In *14th Australasian Fluid Machanics Conference*, number December, pages 941–944, 2001.

[109] Patrick F Mish. *Mean Loading and Turbulence Scale Effects on the Surface Pressure Fluctuations Occurring on a NACA 0015 Airfoil Immersed in Grid Generated Turbulence*. PhD thesis, Virginia Polytechnic Institute and State University, 2001.

[110] Chia-ren Chu and Pei-hung Chiang. Turbulence effects on the wake fl ow and power production of a horizontal-axis wind turbine. *Journal of Wind Engineering and Industrial Aerodynamics*, 124:82–89, 2014.

[111] S.a Torres-Nieves, V.a Maldonado, L.a Castillo, C.b Meneveau, and H.S.c Kang. The role of large scales of turbulence in wind turbine blades at various angles of attack. In *6th AIAA Theoretical Fluid Mechanics Conference*, number June, pages 1–11, Honolulu, 2011.

[112] ESWIRP - Home, http://www.eswirp.eu/.

[113] Mickael Bourgoin, Christophe Baudet, Nicolas Mordant, Tristan VAndenberghe, Sholpan Sumbekova, Nickolas Stelzenmuller, Alberto Aliseda, Gibert Mathieu, Philippe Roche, Romain Volk, Thomas Barois, Miguel Lopez-Caballero, Laurent Chevillard, J F Pinton, Lionel Fiabane, Joel Delville, Carine Fourment, Arezki Bouha, Luminita Danaila, Eberhard Bodenschatz, Gregory Newley, Michael Sinhuber, Antonio Segalini, Ramis Orlu, Ivan Torrano, Jennifer Mantik, Daniel Guariglia, Vaclac Uruba, Vladislav Skala, Jarek Puczylowski, and Joachim Peinke. Investigation of the small scale statistics of turbulence in the Modane S1MA windtunnel. *CEAS Aeronautical Journal*, 2016.

[114] Brian Launder and Dudley Brian Spalding. *Lectures in Mathematical Models of Turbulence*. Academic Press Inc, 1972.

[115] Ansys Inc. ANSYS FLUENT Theory Guide, 2011.

[116] B.E. Launder and D.B. Spalding. The numerical computation of turbulent flows. *Computer Methods in Applied Mechanics and Engineering*, 3(2):269–289, 1974.

[117] Victor Yakhot and Steven A. Orszag. Renormalization group analysis of turbulence. I. Basic theory. *Journal of Scientific Computing*, 1(1):3–51, 1986.

[118] Tsan-Hsing Shih, William W. Liou, Aamir Shabbir, Zhigang Yang, and Jiang Zhu. A new k-\epsilon eddy viscosity model for high reynolds number turbulent flows. *Computers & Fluids*, 24(3):227–238, 1995.

[119] Kuei-Yuan Chien. Predictions of Channel and Boundary-Layer Flows with a Low-Reynolds-Number Turbulence Model. *AIAA Journal*, 20(1):33–38, may 1982.

[120] David C. Wilcox. *Turbulence Modeling for CFD*. DCW Industries, Inc., La Cañada, California, 1998.

[121] DAVID C. WILCOX. Reassessment of the scale-determining equation for advanced turbulence models. *AIAA Journal*, 26(11):1299–1310, nov 1988.

[122] F. R. Menter. Two-equation eddy-viscosity turbulence models for engineering applications. *AIAA Journal*, 32(8):1598–1605, aug 1994.

[123] J. Smagorinsky. General circulation experiments with the primitive equations. *Monthly Weather Review*, 91(3):99–164, mar 1963.

[124] D.K. Lilly. The representation of small-scale turbulence in numerical simulation experiments. In *Proc. of the IBM Scientific Computing Symposium on Environmental Sciences*, 1967.

[125] M Germano, Ugo Piomelli, P Moin, and WH Cabot. A dynamic subgrid scale eddy viscosity model. *Physics of Fluids*, 3(7):1760–1765, 1991.

[126] Ivan Torrano, Mustafa Tutar, Manex Martinez-Agirre, Anthony Rouquier, Nicolas Mordant, and Mickael Bourgoin. Comparison of experimental and RANS-based numerical studies of the decay of grid-generated turbulence. *Journal of Fluids Engineering*, 137(6):061203, feb 2015.

[127] KR Sreenivasan. An update on the energy dissipation rate in isotropic turbulence. *Physics of Fluids*, 10(2):528–529, sep 1998.

[128] Andrey Sogachev and Oleg Panferov. Modification of Two-Equation Models to Account for Plant Drag. *Boundary-Layer Meteorology*, 121(2):229–266, jun 2006.

[129] L. Kantha, J.-W. Bao, and S. Carniel. A note on Tennekes hypothesis and its impact on second moment closure models. *Ocean Modelling*, 9(1):23–29, jan 2005.

[130] Stanley Corrsin. *Turbulence: Experimental methods*. Springer, New York, handbook d edition, 1963.

[131] Stefan Schmidt and Frank Thiele. Detached eddy simulation of flow around A-airfoil. *Flow, Turbulence and Combustion*, 71(1-4):261–278, 2004.

[132] Lars Davidson, Davor Cokljat, Jochen Fröhlich, Michael A. Leschziner, Chris Mellen, and Wolfgang Rodi. *LESFOIL: Large Eddy Simulation of Flow Around a High Lift*. 2003.

[133] I. Mary and P. Sagaut. Large eddy simulation of flow around an airfoil near stall. *AIAA Journal*, 40(6):1139–1145, 2002.

[134] Hong-Sik Im and Ge-Cheng Zha. Delayed Detached Eddy Simulation of a Stall Flow Over NACA0012 Airfoil Using High Order Schemes. In *Proceedings of the 49th AIAA Aerospace Sciences Meeting including the New Horizons Forum and Aerospace Exhibition*, number January, pages 1–16, 2011.

[135] Philipp Gansel, Sebastian Illi, Thorsten Lutz, and Ewald Krämer. Numerical Simulation of Low-Speed Stall and Analysis of Turbulent Wake Spectra. In *Conference on Modelling Fluid Flow (CMFF 2012)*, number 199, pages 199–206, 2012.

[136] Florian R. Menter, Pavel E. Smirnov, Tao Liu, and Ravikanth Avancha. A One-Equation Local Correlation-Based Transition Model. *Flow, Turbulence and Combustion*, 95(4):583–619, 2015.

[137] F. R. Menter, R. B. Langtry, S. R. Likki, Y. B. Suzen, P. G. Huang, and S. Volker. A Correlation-Based Transition Model Using Local Variables - Part I: Model Formulation. *Journal of Turbomachinery*, 128(3):413, 2006.

[138] F. R. Menter, R. Langtry, S. Völker, and P. G. Huang. Transition Modelling for General Purpose CFD Codes. *Journal of Flow Turbulence and Combustion*, 77:277–303, 2006.

[139] R. B. Langtry and F. R. Menter. Correlation-based transition modeling for unstructured parallelized computational fluid dynamics codes. *AIAA Journal*, 47(12):2894–2906, 2009.

[140] Mark Drela. XFOIL: An analysis and design system for low Reynolds number airfoils. In *Low Reynolds number aerodynamics*, pages 1–12. Springer Berlin Heidelberg, 1989.

[141] M Tutar, I. Celik, and I. Yavuz. Modelling of effect of inflow turbulence on large eddy simulation of bluff body flows. *Mathematical and Computational Applications*, 11(3):225–234, 2006.

[142] M Tutar, I Celik, and I Yavuz. Modeling of Effect of Inflow Turbulence Data on Large Eddy Simulation of Circular Cylinder Flows. *Journal of Fluids Engineering*, 129(6):780–790, 2007.

[143] M Tutar and I Celik. Large eddy simulation of a square cylinder flow: Modelling of inflow turbulence. *Wind and Structures*, 10(6):511–532, dec 2007.

[144] M. Tutar and Ü. Sönmez. Computational modelling of inflow turbulence effects on transitional flow in a highly transonic linear turbine. *International Journal of Numerical Methods for Heat & Fluid Flow*, 22(8):1096–1119, 2012.

[145] Philippe R. Spalart and Christopher L. Rumsey. Effective Inflow Conditions for Turbulence Models in Aerodynamic Calculations. *AIAA Journal*, 45(10):2544–2553, 2007.

[146] Lasse Gilling, Niels N. Sorensen, and Lars Davidson. Detached Eddy Simulations of an Airfoil in Turbulent Inflow. In *47th AIAA Aerospace Sciences Meeting Including The New Horizons Forum and Aerospace Expositionth AIAA Aerospace Sciences Meeting Including The New Horizons Forum and Aerospace Exposition*, number 270, pages 1–13, Orlando, FL.

[147] Elia Daniele, Iván Herráez, Bernhard Stoevesandt, and Joachim Peinke. Wind Energy - Impact of Turbulence. chapter DES Study, pages 9–15. Springer Berlin Heidelberg, Berlin, Heidelberg, 2014.

[148] G.R. Tabor and M.H. Baba-Ahmadi. Inlet conditions for large eddy simulation: A review. *Computers & Fluids*, 39(4):553–567, apr 2010.

[149] Anthony Keating, Ugo Piomelli, Elias Balaras, and Hans-Jakob Kaltenbach. A priori and a posteriori tests of inflow conditions for large-eddy simulation. *Physics of Fluids*, 16(12):4696, 2004.

[150] H. Le, P. Moin, and J. Kim. Direct numerical simulation of turbulent flow over a backward-facing step. Journal of Fluid Mechanics. *Journal of Fluid Mechanics*, (330):349–374, 1997.

[151] Emmanuel Sergent. *Vers une méthodologie de couplage entre la Simulation des Grandes Echelles et les modèles statistiques.* PhD thesis, 2002.

[152] A. Smirnov, S. Shi, and I. Celik. Random Flow Generation Technique for Large Eddy Simulations and Particle-Dynamics Modeling. *Journal of Fluids Engineering*, 123(2):359–371, 2001.

[153] Robert H. Kraichnan. Diffusion by a Random Velocity Field. *Physics of Fluids*, 13(1):22, 1970.

[154] C. Fureby, A. D. Gosman, G. Tabor, H. G. Weller, N. Sandham, and M. Wolfshtein. Large Eddy Simulation of Turbulent Channel Flows. *Turbulent shear flows*, 11, 1997.

[155] John Kim, Parviz Moin, and Robert Moser. Turbulence statistics in fully developed channel flow at low Reynolds number. *Journal of Fluid Mechanics*, 177(-1):133, 1987.

[156] P Wang and XS Bai. Large eddy simulations of turbulent swirling flows in a dump combustor: a sensitivity study. *International journal for numerical methods in ...*, (November 2003):99–120, 2005.

[157] Thomas S. Lund, Xiaohua Wu, and Kyle D. Squires. Generation of Turbulent Inflow Data for Spatially-Developing Boundary Layer Simulations. *Journal of Computational Physics*, 140(2):233–258, 1998.

[158] T. Blackmore, W. M. J. Batten, and A. S. Bahaj. Inlet grid-generated turbulence for large eddy simulation. *International Journal of Computational Fluid Dynamics*, 27(6-7):307–315, 2013.

[159] Simon Dahlström. *Large eddy simulation of the flow around a high-lift airfoil*. PhD thesis, Chalmers University of Technology, 2003.

[160] J.S. Baggett, J. Jiménez, and A. G. Kravchenko. Resolution requirements in large-eddy simulations of shear flows. *Center for Turbulence Research*, (Annual Research Briefs):51–66, 1997.

[161] B Vreman, B J Geurts, and H Kuerten. Comparison of numerical schemes in large-eddy simulation of the temporal mixing layer. *International Journal for Numerical Methods in Fluids*, 22(December 1994):297–311, 1996.

[162] Bert Vreman, Bernard Geurts, and Hans Kuerten. Large-eddy simulation of the turbulent mixing layer. *Journal of Fluid Mechanics*, 339:357–390, 1997.

[163] I. B. Celik, Z. N. Cehreli, and I. Yavuz. Index of Resolution Quality for Large Eddy Simulations. *Journal of Fluids Engineering*, 127(September 2005):949, 2005.